JOURNAL OF THE

AERONAUTICAL SCIENCES

VOLUME 25 MAY, 1958 NUMBER 5

ST. LOUIS PUBLIC LIBRARY MAY 12 1958

CONTENTS

The Bending Stability of Thin-Walled Unstiffened Circular Cylinders Including the Effects of Internal Pressure ..... HERBERT S. SUER, LEONARD A. HARRIS, WILLIAM T. SKENE, AND ROLAND J. BENJAMIN 281

The Effect of an Internal Compressible Fluid Column on the Breathing Vibrations of a Thin Pressurized Cylindrical Shell ..... J. G. BERRY AND E. REISSNER 288

A Power-Spectrum Equation for Stationary Random Gusts, Including a Sample Problem ..... K. D. SAUNDERS 295

Oscillating Shock Boundary-Layer Interaction ..... LEON TRILLING 301

Transformation of the Compressible Turbulent Boundary Layer ..... ARTUR MAGER 305

Supersonic Flutter of a Cylindrical Shell—II ..... JOHN W. MILES 312

On Unsteady Interaction Between a Weak Thermal Layer and a Strong Plane Oblique Shock ..... C. T. CHANG 317

Experimental Investigation of the Aerodynamics of a Wing in a Slipstream ..... MARC E. BRENCKMANN 324

Readers' Forum 329

Published by
INSTITUTE OF THE AERONAUTICAL SCIENCES, INC.

JOURNAL OF THE AERONAUTICAL SCIENCES

Editor: W. R. SEARS
Director, Graduate School of Aeronautical Engineering, Cornell University

Associate Editor: ROBERT R. DEXTER *Managing Editor:* RITA J. TURINO
Editorial Assistant: CAROLINE TAYLOR

Editorial Committee

Aerodynamics and Fluid Mechanics

Holt Ashley
H. Julian Allen
Dean R. Chapman
Francis H. Clauser
Hugh L. Dryden
John C. Evvard
Antonio Ferri
Alexander Flax
Wallace D. Hayes
R. T. Jones
Carl Kaplan
H. W. Liepmann
C. C. Lin
H. F. Ludloff
Harold Luskin
Clark B. Millikan
Henry T. Nagamatsu
H. J. E. Reid
George S. Schairer
G. B. Schubauer
John Stack
Theodore Theodorsen
Arthur N. Tifford
Th. von Kármán

Flight Testing

R. R. Gilruth
Melvin N. Gough
W. L. Howland
W. F. Milliken, Jr.

Rotating Wing Aircraft

F. B. Gustafson
K. H. Hohenemser
Bartram Kelley
R. B. Maloy
Ralph McClarren
R. H. Miller
R. H. Prewitt
Igor I. Sikorsky

Structures

John E. Duberg
R. R. Heldenfels
N. J. Hoff
Samuel Levy
J. F. McBrearty
W. Ramberg
E. E. Sechler
F. R. Shanley
C. R. Strang
S. Timoshenko

Meteorology

C. F. Brooks
D. M. Little
F. W. Reichelderfer
K. C. Spengler

Vibration and Flutter

Lee Arnold
M. A. Biot
R. L. Bisplinghoff
Harold A. Cheilek
I. E. Garrick
Martin Goland

Aircraft Design

W. E. Beall
E. H. Heinemann
Hall L. Hibbard
Richard Hutton
C. L. Johnson
A. A. Kartveli
F. K. Teichmann

Electronics

K. C. Black
M. V. Kiebert, Jr.
David S. Little
Paul Rosenberg
Giles J. Strickroth

Physiologic Problems

H. G. Armstrong
Louis H. Bauer
Robert J. Benford
W. Randolph Lovelace, II
Ross A. MacFarland

Flight Propulsion

William Bollay
George W. Brady
R. P. Kroon
Frank E. Marble
Abe Silverstein
E. S. Taylor

Instruments

Alan G. Binnie
Charles H. Colvin
Frank R. Cook
C. S. Draper
S. G. Eskin
C. F. Savage
R. C. Sylvander

SUBSCRIPTION RATES

JOURNAL OF THE AERONAUTICAL SCIENCES, Published Monthly. United States and Possessions: 1 Year, $15.00; Single Copies, $1.50. Foreign Countries Including Canada (American Currency Rates): 1 Year, $16.00; Single Copies, $1.50.

AERONAUTICAL ENGINEERING REVIEW, Published Monthly. United States and Possessions: 1 Year, $5.00; Single Copies, $0.50. Foreign Countries Including Canada (American Currency Rates): 1 Year, $6.00; Single Copies, $0.50.

Notices of change of address should be sent to the Institute at least 30 days prior to actual change of address.

Manuscripts for publication, proofs, and all correspondence should be addressed to the Editorial Office of the JOURNAL.

Publication Office, 20th and Northampton Sts., Easton, Pa. Correspondence regarding subscriptions may be addressed to the Editorial Office of the JOURNAL OF THE AERONAUTICAL SCIENCES, 2 East 64th Street, New York 21, N.Y.

© Copyright, 1958, by the Institute of the Aeronautical Sciences, Inc.

Second-Class Mail Privileges Authorized at Easton, Penna. Acceptance for mailing at a special rate of Postage provided for in the Act of August 24, 1912. Authorized April 29, 1937.

JOURNAL OF THE AERONAUTICAL SCIENCES

VOLUME 25 MAY, 1958 NUMBER 5

The Bending Stability of Thin-Walled Unstiffened Circular Cylinders Including the Effects of Internal Pressure†

HERBERT S. SUER,* LEONARD A. HARRIS,* WILLIAM T. SKENE,** AND ROLAND J. BENJAMIN***

North American Aviation, Inc.

SUMMARY

In a recent paper, the authors presented a statistical, semiempirical design procedure for the determination of the buckling strength of unpressurized and pressurized cylinders under axial compression. This procedure has been extended in the present paper to the bending of unpressurized and pressurized cylindrical shells and allows the calculation of the critical bending stress with a knowledge of the cylinder geometry and the internal pressure only.

Because no published data could be found, an extensive series of bending tests of pressurized cylinders has been performed. These new data for pressurized cylinders are treated semiempirically together with all of the other known test data for unpressurized cylinders. Best-fit curves are presented using applicable theoretical parameters. Design curves for determining the critical buckling stress for unpressurized and pressurized cylinders in bending are then developed as 90 per cent probability curves from the test data.

SYMBOLS

C_b = bending buckling stress coefficient in the equation $\sigma_{cr} = C_b E(t/r)$ for unpressurized cylinders

C_{bp} = bending buckling stress coefficient in the equation $\sigma_{crp} = C_{bp} E(t/r)$ for pressurized cylinders

ΔC_{bp} = increase in the buckling stress coefficient, C_b, caused by internal pressure ($\Delta C_{bp} = C_{bp} - C_b$)

E = modulus of elasticity

I = moment of inertia of cylinder

L = length of cylinder

M_{cr} = unpressurized critical buckling moment

M_{crp} = pressurized critical buckling moment

p = internal pressure

r = radius of cylinder

t = wall thickness of cylinder

σ_{cr} = unpressurized critical buckling stress ($\sigma_{cr} = M_{cr} r/I$)

σ_{crp} = pressurized critical buckling stress ($\sigma_{crp} = M_{crp} r/I$)

$\Delta\sigma_{cr}$ = increase in the critical buckling stress caused by internal pressure ($\Delta\sigma_{cr} = \sigma_{crp} - \sigma_{cr}$)

Received December 9, 1957.

† The authors gratefully acknowledge the assistance of the personnel of the Structural Test Laboratory of the Missile Development Division who conducted the test program.

* Senior Structures Engineer, Missile Development Division.

** Group Leader, Structures Data and Methods, Missile Development Division.

*** Formerly, Senior Structures Engineer, Missile Development Division. Now, Senior Aeronautical Engineer, Cook Research Laboratories, Cook Technological Center, Morton Grove, Illinois.

INTRODUCTION

Statement of Problem

DURING the last few years the increased use of pure monocoque construction in aircraft and missile structures has forced a closer inspection of the stability analysis of unstiffened circular cylinders. It is well known that in many cases unsatisfactory agreement exists between the values of the critical buckling stress determined experimentally and those predicted by the classical theory. Experimental values of the critical stress are almost always lower than those calculated theoretically. For some loading conditions, large-deflection theories which include an initial imperfection parameter have been developed[1–5] to explain the discrepancy between test and linear theory. However, use of these more refined theoretical treatments is not satisfactory from a design standpoint because an estimate must first be made of the probable initial imperfection. To circumvent this design difficulty for the case of axial compression, the authors[6] have recently presented statistical, semiempirical design curves for the determination of the critical compressive stress of

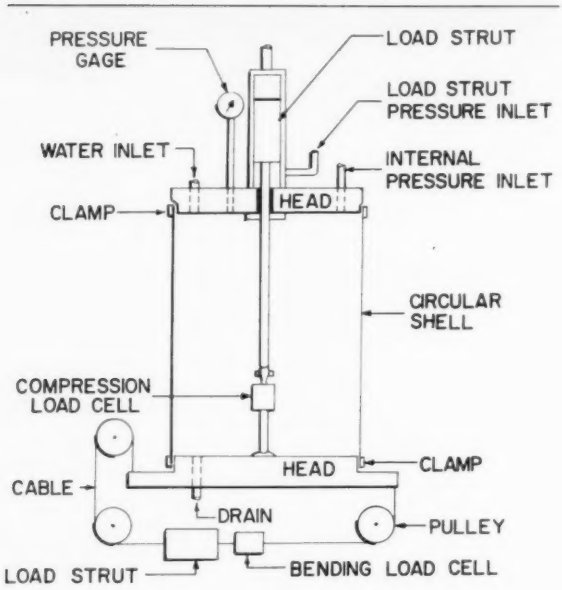

FIG. 1. Schematic drawing of test jig.

unpressurized and pressurized circular cylinders.

In general, the behavior of an unstiffened cylinder under bending is similar to that of a cylinder under compression—that is, the buckling mode shapes are similar, snap buckling may occur, and the buckling stress is sensitive to initial imperfections. In addition, unpressurized cylinders under bending and under compression share the distinction of exhibiting equally poor agreement between small-deflection theory and test. More precise theoretical treatments which include the effects of large deflections and initial irregularities have not been applied to cylinders in bending, as far as is known, although it is probable that better correlation could be achieved between test and theory by their use. For pressurized cylinders in bending, no theoretical analyses have been published.

Because of the difficulty of achieving a theoretical treatment of the problem, and because it was desired to compare the critical stresses under compression and bending, it is proposed in the present paper to treat the behavior of cylinders under bending semiempirically, in a manner similar to that previously used for cylinders under compression. Use of the statistical method of the analysis of cylinder stability data may be considered to amount to an empirical evaluation of the effects of initial irregularities. The basic assumption in this evaluation is that the initial imperfections of the test cylinders were representative of those likely to be encountered in actual aircraft structures. Where sufficient data are available, such a procedure should provide reliable, statistically defined design curves.

Scope of Investigation

Because test data in bending were not available for short cylinders, the present paper has been restricted to long cylinders unaffected by end fixity conditions. As a consequence, the theoretical parameters from the classical form of the buckling equation for long cylinders, $\sigma_{cr} = C_b E(t/r)$, have been used to develop a design curve for unpressurized cylinders. To evaluate the test data, the experimental values of the bending buckling coefficient, C_b, have been plotted as a function of the r/t ratio. A best-fit curve was placed through the test data and a 90 per cent probability curve was statistically defined. A thorough literature search indicated that considerable test data were available for unpressurized cylinders under bending and the results of these tests, with all but a few exceptions, were used in the study. However, as will be seen below, the data were scanty for values of r/t greater than 1,500.

In the present treatment of pressurized cylinders in bending, the parameters from the theoretical development by Lo, Crate, and Schwartz[7] for pressurized cylinders under compression have been used. The use of these parameters would appear justified because of the similarity between the behavior of circular cylinders under bending and under compression.

For pressurized cylinders under bending, apparently no previous tests had been performed. A total of 58 tests were performed in the Structural Test Laboratory and these tests provide the only data known to be available for the bending stability of pressurized cylinders.

TABLE 1

Results of North American Aviation Tests
18-8 Half-Hard Stainless Steel, $E = 27 \times 10^6$ psi, $r = 8.75$ in., $L = 21.5$ in.

Spec. No.*	r/t	p, psi	σ_{cr}, psi	Spec. No.*	r/t	p, psi	σ_{cr}, psi†
Unpressurized							
210	1,006	0	9,176	72(2)	2,734	0	1,218
211			9,797	77			1,624
212			7,742	77(2)			1,624
213	1,006		7,838	78			1,624
72	2,734	0	1,299	78(2)	2,734	0	1,461
Pressurized—Axially Pretensioned							
5	1,006	1.5	11,290	89(2)	2,734	4.4	10,530
282		1.8	10,987	86		8.4	16,990
285		18.4	21,243	1		8.5	23,550
286	1,006	18.4	18,967	11		14.0	31,000
283	2,734	2.2	8,481	9		18.0	30,600
284		2.2	9,019	10		18.0	31,600
85		4.4	9,742	13		18.4	38,750
87	2,734	4.4	10,070	3	2,734	18.4	36,650
Pressurized—Axial Pretensioning Balanced by Compressive Load							
275	1,006	1.0	9,707	84	2,734	4.4	5,521
276		1.0	11,649	75		8.4	6,170
277		1.8	12,127	75(2)			5,781
278		1.8	10,842	76			6,008
280		3.5	11,350	76(2)			6,008
281		3.5	12,425	77(3)			7,112
287		8.4	13,808	77(4)			6,982
288		8.4	14,415	78(3)			6,657
208		16.4	14,820	78(4)		8.4	6,495
209	1,006	16.4	15,200	116		12.4	7,307
272	2,734	1.1	4,841	117		12.4	7,534
274		1.1	3,475	79		16.4	8,119
270		2.2	4,965	79(2)			7,469
273		2.2	4,344	80			7,794
274(2)		3.5	4,758	80(2)		16.4	8,119
83	2,734	4.4	5,683	81	2,734	24.4	8,119

* Numbers in parentheses refer to the number of the succeeding test for those specimens tested more than once. Each succeeding test was made at an internal pressure equal to or greater than any previous test of the same cylinder.

† $\sigma_{cr} = Mr/I$.

For design purposes, it appeared advantageous to present the data for pressurized cylinders in two parts: that part of the critical stress which could be attained if the cylinder were unpressurized and that part by which the unpressurized critical stress is increased by internal pressure. As a consequence, the pressurized data have been analyzed and a design curve developed using the parameter $(\Delta\sigma_{cr}/E)(r/t)$ as a function of the pressure parameter $(p/E)(r/t)^2$, where $\Delta\sigma_{cr}$ is the increase in the critical bending stress associated with the internal pressure, p. This presentation has the advantage of giving the designer a direct indication of the effect that internal pressure has in increasing the allowable critical stress.

Experimental Investigations

North American Aviation Investigation

Prior to the present investigation, there appears to have been no comprehensive testing of pressurized cylinders in bending. Therefore, an extensive series of bending tests of model circular cylinders were performed at the Structural Test Laboratory of the Missile Development Division to obtain test data within the parameter range likely to be encountered in missile or aircraft structures.

A total of 58 tests was performed, 10 of unpressurized cylinders and 48 of pressurized cylinders. Two series of tests were conducted of pressurized cylinders in bending. In one series, the longitudinal component of the internal pressure was balanced by an axial compressive load before the bending moment was applied, while, in the second series, the longitudinal component of the internal pressure was not balanced.

The test cylinders were fabricated from 0.0032-in. and 0.0087-in. thick, half-hard, 18-8 stainless steel foil. The above sheet thicknesses were the averages of a number of micrometer measurements. The cylinders were prepared with a length of 21.5 in. and a radius of 8.75 in., and had r/t ratios of approximately 1,000 and 2,730. The internal pressure was varied from 0 to 24 psi. Most of the cylinders were fabricated by wrapping the sheet and adhesive-bonding a single $\frac{3}{8}$-in. wide longitudinal seam with Epon VI adhesive. Some of the later cylinders were fabricated by seam-welding, which proved to be a faster and simpler technique. No appreciable difference could be noted between the buckling stresses from the adhesive-bonded and from the seam-welded cylinders. The test cylinders were oriented with the vertical seam at the neutral axis.

A schematic drawing of the test jig with a cylinder in position for testing is shown in Fig. 1. The test cylinders snugly fitted the lower and upper heads of the test jig and were clamped to the heads by metal straps. The straps prevented slippage and leakage between the heads and the cylinder. Internal pressure was pneumatically supplied, but for reasons of safety most of the cylinders were partially filled with water for those tests in which the internal pressure exceeded 2 psi. A manometer was used to measure the internal pressure. In computing the pressure parameter from the test results, an internal pressure equivalent to a head of water of approximately half the specimen length was added to the applied pneumatic pressure reading for those specimens which were filled with water. Bending and axial compressive loads were applied by hydraulic struts and measured by SR-4 load cells.

The geometrical parameters and the buckling stresses of the test cylinders are recorded in Table 1. The buckling loads of the test specimens were determined visually. For most specimens, a visual determination of the buckling load was relatively simple because the buckles often snapped into position. Occasionally, buckles appeared to grow out of relatively large initial irregularities. Incipient buckling of a pressurized cylinder was often indicated by the formation of small circumferential ripples. Although initially very shallow, these ripples (similar in appearance to the shape of an axisymmetrical compression buckle) could easily be seen in the reflecting surface of the cylinder.

Photographs of typical buckle patterns in unpressurized and pressurized cylinders are shown in Figs. 2, 3, and 4. These diamond-shaped buckle patterns are typical for the buckling of unstiffened cylinders loaded in bending or in axial compression. Internal pressure changed the buckle pattern by decreasing the axial and circumferential wavelengths, although the longitudinal wave length was decreased more than the circumferential wave length.

Table 2
Summary of Previous Experimental Investigations*

Reference	Material	No. of Specimens	Geometrical Parameters r	r/t	L/r
Donnell	Brass and Steel	33	0.90–2.8	158–1,500	2.1–26
Imperial	17ST Aluminum	11	2.5–5.0	119–322	2.4–4.8
Lundquist	17ST Aluminum	57	7.5,15	323–1,430	0.50–5.0
Mossman and Robertson	Aluminum Alloy	3	18.0	563–1,286	2.0
Peterson	17ST Aluminum	15	9.6–39	180–749	0.25–3.9

* All specimens unpressurized.

Summary of Other Investigations

An important aspect of the present semiempirical treatment of unpressurized cylinders has been the accumulation of test data from past investigations. A large number of investigations were carefully reviewed to obtain test data, but only the experimental results from the investigations,[8–12] summarized in Table 2, have been used in developing the analysis. Other experimental data were not included in the study for one or more of the following reasons: (1) insufficient data were given; (2) test specimens were fabricated from nonmetallic materials such as paper, celluloid, or rubber which frequently exhibit variations in properties and thickness; (3) critical stresses were above the yield point; (4) critical stresses were above the proportional limit, and insufficient data were given to make a plas-

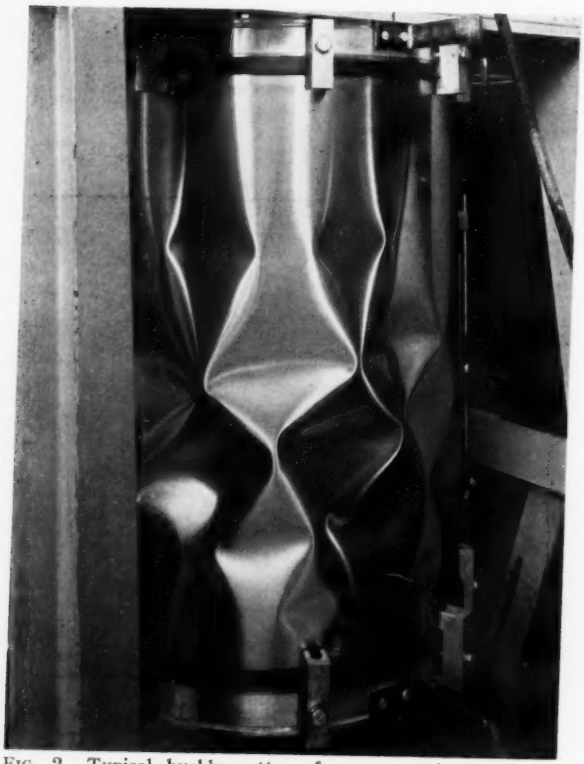

FIG. 2. Typical buckle pattern for unpressurized cylinder.

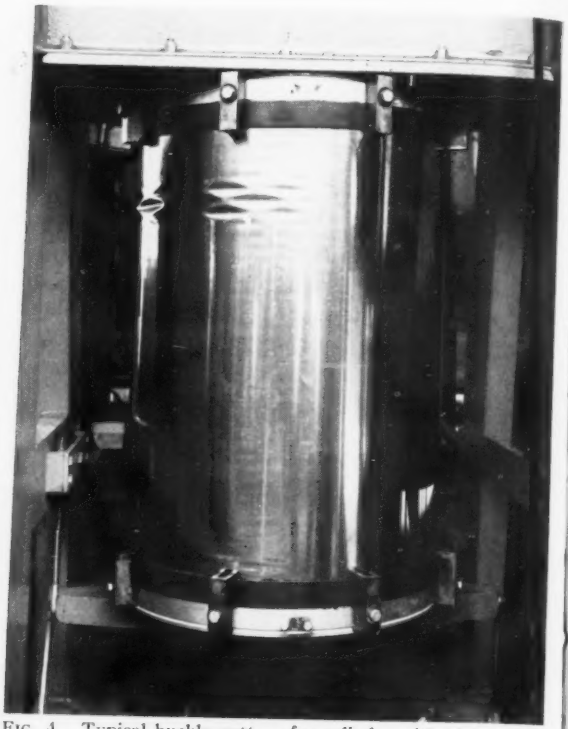

FIG. 4. Typical buckle pattern for cylinder with high internal pressure.

FIG. 3. Typical buckle pattern for cylinder with low internal pressure.

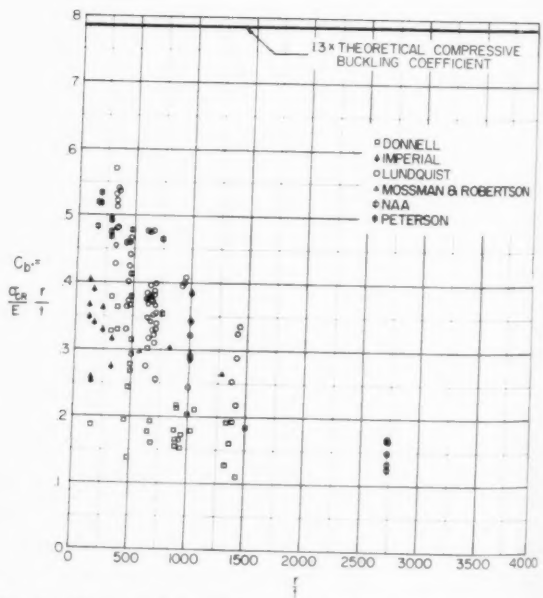

FIG. 5. Unpressurized bending buckling stress coefficients as a function of r/t.

ticity correction; (5) the r/t ratio was less than 100; or (6) the L^2/rt ratio was less than 40.

Analysis of Unpressurized Cylinder Data

The buckling stress for a long unpressurized cylinder in bending can be expressed as

$$\sigma_{cr} = C_b E(t/r) \tag{1}$$

where, for a particular case, the theoretical value of C_b has been found by Flügge[13] to be about 30 per cent higher than the corresponding classical compressive buckling coefficient of 0.605. In Fig. 5, 129 experimental values of the buckling coefficient from the tests of six investigations are plotted as a function of the r/t ratio. As is the case with compressive buckling, there is considerable scatter in the bending test data and the experimental values of the buckling coefficient are considerably lower than the theoretically predicted values. This large scatter and the discrepancy between theory and test has often been attributed to the effects of initial imperfections or defects in the test specimens. In general, experimental values of the buckling coefficient decrease with an increase in the r/t ratio, indicating an apparent increase in the magnitude and/or the effect of the initial imperfections with increasing r/t. The relationship between C_b and r/t will be established by empirically fitting a curve to the test data and deriving design curves on the basis of probability theory.

In Fig. 6, the logarithm of the buckling coefficient, C_b, has been plotted as a function of r/t. In addition to more clearly defining the relationship between C_b and r/t, the semilog plot has the advantage of producing a more uniform scatter band in the range in which data are available. A "best-fit" curve is shown on the graph of log C_b as a function of r/t. The shape of this curve was selected by the investigators as being representative of the trend of the experimental data. The vertical location of the curve with respect to the test data was achieved by satisfying the equation

$$\sum_{i=1}^{N} (y_i - y_a) = 0 \tag{2}$$

where $y_i = \log C_b$, and $y_a = \log C_b$ for points from the best-fit curve at r/t of test point i. If Eq. (2) is satisfied, it can be shown that the following relationship is also satisfied:

$$\sum_{i=1}^{N} (y_i - y_a)^2 = \text{a minimum} \tag{3}$$

Thus, by satisfying Eq. (2), the assumed curve was in the least squares position. Note that the best-fit curve may not be reliable for values of the r/t ratio greater than 1,500 because of the scarcity of test data.

A statistical analysis of the data was performed after a best-fit curve had been established with the sum of the squares of the deviations a minimum. An IBM 701 digital computer was used to solve the equations of the statistical analysis in the following form:

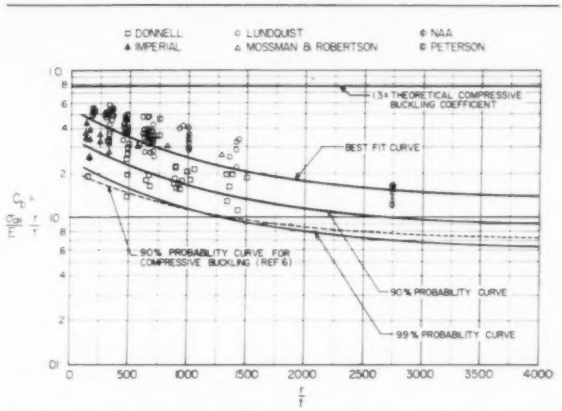

FIG. 6. Unpressurized bending buckling stress coefficients as a function of r/t (semilogarithmic grid).

$$y_p = y_a - K_p S \tag{4}$$

where

$$\left.\begin{aligned} y_p &= \log C_b \text{ for a specified probability} \\ S &= \sqrt{\sum_{i=1}^{N} (y_i - y_a)^2/(N-1)} = \\ &\qquad \text{standard deviation} \\ N &= \text{number of test points} \\ K_p &= \text{small sample probability coefficient} \end{aligned}\right\} \tag{5}$$

The solution of Eq. (5) for the test points gave a value of 0.130 for the standard deviation of the log C_b. The value of $K_p = 1.47$ was selected from a small sample statistical table[14] for a 90 per cent probability design curve. The 90 per cent probability design curve is drawn in Fig. 6. This curve agrees well with and generally parallels the lower bound of the test data. The 99 per cent probability curve is also shown on this graph. The relatively large difference between the 90 per cent and the 99 per cent probability curves is typical of a statistical analysis of test data with a large scatter.

In Fig. 6, the 90 per cent probability bending design curve is compared with the 90 per cent probability design curve for the compressive buckling of thin-walled cylinders from reference 6. It may be observed that there is not a uniform ratio between the buckling coefficients for the two loading conditions over the complete range of r/t. At low values of r/t, the bending critical stress is about 60 per cent greater than that for compression. This difference decreases with increasing r/t to a value of about 25 per cent for large r/t.

In the procedure just described, it has been necessary for the investigators to select a best-fit curve which indicates the general trend of the test data. Because the data is scanty at large values of r/t, the reliability of the selected shape is necessarily somewhat questionable in this region. The similarity between the behavior of a cylinder under axial compression and under bending suggests that the variation of the buckling coefficient with the r/t ratio might be of the same shape for both cases. In compression, considerably more data were available, and it is of interest, therefore, to perform a statistical analysis of the bending data using

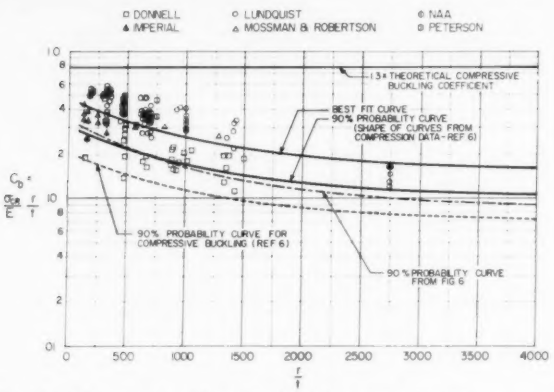
□ DONNELL
▲ IMPERIAL
○ LUNDQUIST
△ MOSSMAN & ROBERTSON
◎ NAA
⊙ PETERSON
1.3 × THEORETICAL COMPRESSIVE BUCKLING COEFFICIENT
BEST FIT CURVE
90% PROBABILITY CURVE (SHAPE OF CURVES FROM COMPRESSION DATA - REF 6)
90% PROBABILITY CURVE FOR COMPRESSIVE BUCKLING (REF 6)
90% PROBABILITY CURVE FROM FIG 6
$C_b = \frac{\sigma_{cr}}{E}\frac{r}{t}$
$\frac{r}{t}$

FIG. 7. Unpressurized bending buckling stress coefficients as a function of r/t (semilogarithmic grid).

the previously selected shape of curve[6] to represent the variation of the compressive buckling coefficient with r/t.

In Fig. 7, the curve with the compression shape is shown in the least squares position for the bending data. A statistical analysis has been performed as before, and the 90 per cent probability curve is drawn in Fig. 7. A comparison of the 90 per cent probability design curve for bending based on the compression curve shape and the 90 per cent probability design curve for compression from reference 6 indicates that the bending coefficients can be obtained by increasing the axial compression coefficients by about 35 per cent. However, the basic shape of the curve from the compression data does not fit the bending data well for all values of r/t. Therefore, the constant ratio between the buckling coefficients determined in the above manner may not be reliable.

Because the final design curve of this study is defined in terms of a statistical probability of failure, it is incumbent on the user of this data to decide what probability is required by the design criteria demands of his particular structure. If the 99 per cent probability design curve is used, there is a slim 1 per cent probability of failure at ultimate load. If the 90 per cent probability curve is selected, there is a 10 per cent probability of failure—associated with a significant weight-saving in the shell.

Analysis of Pressurized Cylinder Data

The critical buckling stress of pressurized cylinders in bending may be expressed by a relationship analogous to that for unpressurized cylinders,

$$\sigma_{crp} = C_{bp}E(t/r) \qquad (6)$$

where experimental results indicate that C_{bp} is a function of the internal pressure as well as the geometry of the cylinder. An accurate theoretical treatment would be difficult to achieve and, as is the case with unpressurized cylinders, a prior knowledge of the initial imperfections would probably be required for an accurate prediction of the buckling stress. For this reason, an empirical treatment has been made using the parameter derived theoretically[7] for the compressive buckling of pressurized cylinders. The similarity in the behavior of cylinders in compression and in bending suggests the validity of this approach.

In Fig. 8, the values of the buckling coefficient C_{bp} are plotted as a function of the parameter $(p/E)(r/t)^2$. The triangular symbols are used to indicate those test specimens axially pretensioned to a stress of $pr/2t$ by the internal pressure on the cylinder heads. The circular symbols indicate those specimens to which an axial compressive load, sufficient to balance the pretension caused by the internal pressure, was applied prior to the application of the bending moment. It should be noted that in computing the value of C_{bp}, the critical bending stress σ_{crp} has been obtained by dividing the critical moment by the section modulus of the cylinder. For pretensioned cylinders, the actual maximum compressive stress is found by subtracting $pr/2t$ from σ_{crp}.

A line is drawn in Fig. 8 to indicate the magnitude of the axial pretension stress $pr/2t$ in terms of C_{bp}. The pretensioned specimens must always fail at a bending stress greater than $\sigma_{cr} = pr/2t$, which represents the compressive bending stress required to balance the longitudinal tensile stress produced by the internal pressure. It can be observed that, in general, the buckling coefficient for most of the axially stressed specimens can be obtained by adding $pr/2t$ to the critical stress for the specimens with the axial pretension balanced. At low values of the pressure parameter, the axial stress has a negligible effect on the buckling stress coefficient. At large values of the pressure parameter, the effect of the axial component of the stress induced by the internal pressure becomes predominant.

In Fig. 8 a line is also drawn to indicate the general region of test data for the compressive buckling of pressurized cylinders. The experimental buckling coefficients for cylinders in bending are significantly greater than those for cylinders in axial compression.

In order to better demonstrate the effect which internal pressure has in increasing the buckling stress

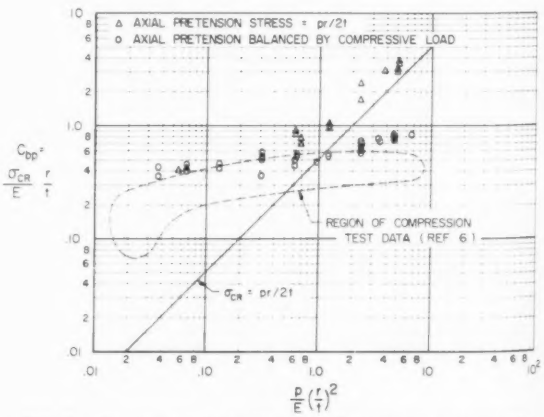
△ AXIAL PRETENSION STRESS = pr/2t
○ AXIAL PRETENSION BALANCED BY COMPRESSIVE LOAD
REGION OF COMPRESSION TEST DATA (REF 6)
$\sigma_{CR} = pr/2t$
$C_{bp} = \frac{\sigma_{CR}}{E}\frac{r}{t}$
$\frac{p}{E}\left(\frac{r}{t}\right)^2$

FIG. 8. Bending buckling stress coefficients for pressurized circular cylinders.

coefficient, the experimental data are replotted in Fig. 9 in terms of the increment ΔC_{bp} to the buckling coefficient C_b. The increase in the buckling stress coefficient ΔC_{bp} represents the beneficial effect of internal pressure. The total value of the buckling coefficient is obtained by adding the buckling coefficient for unpressurized cylinders to the increase in the buckling coefficient due to internal pressure. In order to plot this data, it was first necessary to determine the unpressurized buckling coefficient for each specimen. The 90 per cent probability design curve of Fig. 6 was used for this purpose. The direct benefit of lateral internal pressure to the stability of cylinders in bending is indicated by those specimens with no net axial stress (the balanced specimens) represented by the circular symbols. At large values of the pressure parameter, the additional benefit of the axial pretension is clearly demonstrated by the large increase in ΔC_{bp} of pretensioned specimens, represented by the triangular symbols, over that for the balanced specimens. The limiting value of the increase in the buckling stress coefficient for pretensioned pressurized cylinders at very high values of the pressure parameter is given by the line $\sigma_{cr} = pr/2t$.

The analysis of the pressurized cylinder data was achieved by selecting a best-fit curve for those specimens in which the axial pretension was balanced. This curve (shown in Fig. 9) was selected by the investigators as best indicating the general trend of the experimental data. At large values of the pressure parameter, the curve is drawn to approach an asymptote. A tendency for the buckling stress to approach a maximum value and remain constant with increasing $(p/E)(r/t)^2$ is suggested by the theoretical and experimental investigations of the compressive buckling of pressurized cylinders. Agreement between the best-fit curve and experimental data is apparent from Fig. 9. The best-fit curve has been placed so that the sum of the squares of the deviations of the experimental data from the best-fit curve is a minimum.

A statistical analysis of the test data was performed for the specimens with no axial pretension to establish the 90 per cent probability design curve shown in Fig. 9. Because data were available from the North American Aviation tests only, the sample may not be representative and a lower probability curve should perhaps be used for design purposes. The data were not considered sufficient to permit a statistical analysis of the pretensioned experimental data. Therefore, a lower bound curve is suggested for use in design of pretensioned cylinders.

Conclusions

A semiempirical design procedure has been developed for the prediction of the critical maximum stress for thin-walled circular cylinders under bending. For unpressurized cylinders, 90 per cent probability design curves have been derived for the bending buckling coefficient, C_b, as a function of r/t. For pressurized cylinders, a 90 per cent probability design curve has been derived for the increase in the bending buckling coefficient

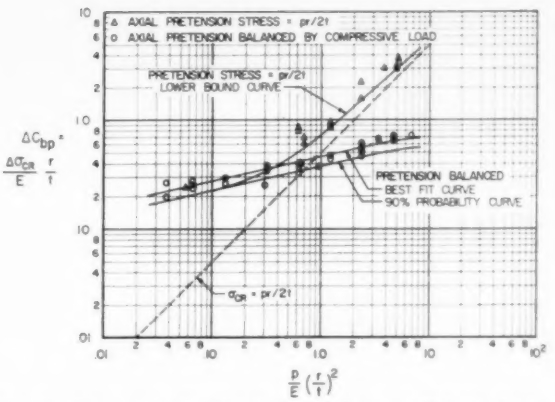

Fig. 9 Increase in bending buckling stress coefficients due to internal pressure.

ΔC_{bp} as a function of the pressure parameter $(p/E)(r/t)^2$.

Additional tests should be made for unpressurized cylinders with r/t ratios greater than 1,500 to verify the shape of the design curve. Tests of pressurized cylinders in bending should also be conducted by other investigators to increase the reliability of the test sample.

References

[1] Donnell, L. H., and Wan, C. C., *Effect of Imperfections on Buckling of Thin Cylinders and Columns Under Axial Compression*, Journal of Applied Mechanics, Vol. 17, No. 1, pp. 73–88, 1950.

[2] Loo, Tsu-Tao, *Effects of Large Deflections and Imperfections on the Elastic Buckling of Cylinders Under Torsion and Axial Compression*, Ph.D. Thesis, Dept. of Mechanics, Illinois Institute of Technology, 1952.

[3] Donnell, L. H., *Effect of Imperfections on the Buckling of Thin Cylinders Under External Pressure*, Journal of Applied Mechanics, Vol. 23, No. 4, pp. 569–575, 1956.

[4] Nash, W. A., *Buckling of Initially Imperfect Cylindrical Shells Subjected to Torsion*, Journal of Applied Mechanics, Vol. 24, No. 1, pp. 125–130, March, 1957.

[5] Nash, W. A., *Effect of Large Deflections and Initial Imperfections on the Buckling of Cylindrical Shells Subject to Hydrostatic Pressure*, Journal of the Aeronautical Sciences, Vol. 22, No. 4, pp. 264–269, April, 1955.

[6] Harris, L. A., Suer, H. S., Skene, W. T., and Benjamin, R. J., *The Stability of Thin-Walled Unstiffened Circular Cylinders Under Axial Compression Including the Effects of Internal Pressure*, Journal of the Aeronautical Sciences, Vol. 24, No. 8, pp. 587–596, August, 1957.

[7] Lo, H., Crate, H., and Schwartz, E. B., *Buckling of Thin-Walled Cylinder Under Axial Compression and Internal Pressure*, NACA TN 2021, January 1950.

[8] Donnell, L. H., *A New Theory for the Buckling of Thin Cylinders Under Axial Compression and Bending*, Trans. ASME, Vol. 56, pp. 795–806, 1934.

[9] Imperial, F. F., *The Criterion of Elastic Instability of Thin Duralumin Tubes Subjected to Bending*, M.S. Thesis, Dept. of Mechanical Engineering, University of California, 1932.

[10] Lundquist, E. E., *Strength Tests of Thin-Walled Duralumin Cylinders in Pure Bending*, NACA TN 479, 1933.

[11] Mossman, R. W., and Robinson, R. G., *Bending Tests of Metal Monocoque Fuselage Construction*, NACA TN 357, 1930.

[12] Peterson, J. P., *Bending Tests of Ring Stiffened Circular Cylinders*, NACA TN 3735, 1956.

[13] Flügge, W., *Die Stabilitat der Kreiszlinderschale*, Ing-Archiv, Bd III, Heft 5, pp. 463–506, December, 1932.

[14] Dixon, W. J., and Massey, F. J., Jr., *Introduction to Statistical Analysis*, 1st Ed., pp. 334–339, McGraw-Hill Book Company, Inc., New York, 1951.

The Effect of an Internal Compressible Fluid Column on the Breathing Vibrations of a Thin Pressurized Cylindrical Shell

J. G. BERRY* AND E. REISSNER**

The Ramo-Wooldridge Corporation and Massachusetts Institute of Technology

SUMMARY

The free oscillations of a thin pressurized cylindrical shell containing a compressible fluid are studied here. The use of an approximate set of shell equations (shallow shell theory) leads to a relatively simple formula for the natural frequencies of the coupled fluid-cylinder system. The results of some computations are presented.

(1) INTRODUCTION

IN THE FOLLOWING, we consider the determination of the inertia and compressibility effects of an internal liquid or gas column on the breathing vibrations of thin pressurized circular cylindrical shells. By breathing vibrations we mean those vibrations of the points of the cylinder walls which correspond to radial deformations proportional to $\cos n\theta$ or $\sin n\theta$, where the integer n has at least the value 2. We do not consider rotationally symmetric vibrations corresponding to $n = 0$ or beam bending vibrations corresponding to $n = 1$.

It has been shown in earlier reports[1, 2] that it is possible to analyze very accurately the breathing vibrations of thin pressurized cylindrical shells which do not contain an internal fluid by means of a system of approximate shell equations. This system, which is considerably simpler than the classical equations as given by Love, consists of the equations of the theory of shallow shells, with an additional simplification due to the omission of certain of the inertia terms.[3, 4] The nature of this theory is such that it is also applicable when the inertia and compressibility of an internal fluid are taken into account. It is this application which is carried out here.

The present paper consists of three main sections. In Section (2) the equations for transverse vibrations of pressurized shallow cylindrical shells are discussed. The section concludes with a formula for the frequencies of free vibrations. This formula includes a term for an apparent inertia of the shell walls due to the presence of an internal fluid.

In Section (3) the equations for the small motion of an inviscid compressible circular cylindrical fluid column are discussed. The surface of the fluid column is assumed to be acted upon by a pressure which is a function of the axial and circumferential space coordinates and time. In particular, we determine the fluctuating pressure over the cylindrical surface of the fluid column in terms of the radial acceleration of points on the cylindrical surface. A specific expression is obtained for the apparent inertia term appearing in the frequency equation of Section (2).

Section (4) contains a discussion of the natural frequencies of the elastic cylinder – internal fluid system. A qualitative discussion is given concerning the effects of fluid compressibility and mass on the frequencies of the coupled system. The results of some numerical calculations are presented.

(2) TRANSVERSE VIBRATIONS OF SHALLOW CYLINDRICAL SHELLS

General Theory

As discussed in reference 4, it is possible to reduce the system of differential equations which govern finite transverse vibrations of shallow shells* with middle surface equation

$$z = z(x, y) \tag{2.1}$$

to the following form:

$$\begin{aligned} D\nabla^4 w + m(\partial^2 w/\partial t^2) = p_z + {} & \\ [(\partial^2 z/\partial x^2) + (\partial^2 w/\partial x^2)]\,(\partial^2 F/\partial y^2) + {} & \\ [(\partial^2 z/\partial y^2) + (\partial^2 w/\partial y^2)]\,(\partial^2 F/\partial x^2) - {} & \\ 2[(\partial^2 z/\partial x \partial y) + (\partial^2 w/\partial x \partial y)]\,(\partial^2 F/\partial x \partial y) & \end{aligned} \tag{2.2}$$

$$\begin{aligned} \nabla^4 F = -Eh[(\partial^2 z/\partial x^2)(\partial^2 w/\partial y^2) + (\partial^2 z/\partial y^2) \times {} & \\ (\partial^2 w/\partial x^2) - 2(\partial^2 z/\partial x \partial y)(\partial^2 w/\partial x \partial y) + {} & \\ (\partial^2 w/\partial x^2)(\partial^2 w/\partial y^2) - (\partial^2 w/\partial x \partial y)^2] & \end{aligned} \tag{2.3}$$

In these equations, w is the deflection of points in the middle surface of the shell in the direction of the z-axis; F is Airy's stress function which serves to describe middle surface stresses in the shell; m is the mass of the shell per unit surface area; p_z is the intensity of surface loading on the shell in the direction of the z-axis; and D is the bending stiffness factor, given by $D = Eh^3 \div 12(1 - \nu^2)$, where ν is Poisson's ratio, E is Young's

Received July 25, 1957.

* Member of the Technical Staff, Guided Missile Research Division, The Ramo-Wooldridge Corporation.

** Professor of Mathematics, Massachusetts Institute of Technology, and Consultant to the Engineering Mechanics Department, The Ramo-Wooldridge Corporation.

* A shell is said to be shallow when the ratio of rise to span is less than 1, say 1/8. In the present case, it turns out that shallow shell theory gives good results[2] when the rise to span ratio is as large as 1/2.

modulus, and h is the constant wall thickness of the shell. The operator ∇^4 is the iterated Laplace operator $\partial^4/\partial x^4 + 2\partial^4/\partial x^2\partial y^2 + \partial^4/\partial y^4$.

We assume that the load intensity p_z is composed of two parts, $p_z = p_0 + p_1$, where p_0 is a constant internal pressure, and p_1 is a fluctuating part which may be the interaction force between the oscillating shell and the oscillating internal fluid. The constant load, p_0, is resisted by membrane stress resultants N_{x0}, N_{y0}, and N_{xy0}, which depend on an Airy stress function, F_0, as follows:

$$N_{x0} = \partial^2 F_0/\partial y^2, \quad N_{y0} = \partial^2 F_0/\partial x^2, \quad N_{xy0} = -(\partial^2 F_0/\partial x\partial y) \tag{2.4}$$

From Eq. (2.2), the relationship between F_0 and p_0 is

$$p_0 + (\partial^2 z/\partial x^2)(\partial^2 F_0/\partial y^2) + (\partial^2 z/\partial y^2) \times (\partial^2 F_0/\partial x^2) - 2(\partial^2 z/\partial x\partial y)(\partial^2 F_0/\partial x\partial y) = 0 \tag{2.5}$$

The complete stress function F, corresponding to the loads $p_0 + p_1$, will be taken in the form

$$F = F_0 + F_1 \tag{2.6}$$

We now assume that the actual states of stress and displacement are small deviations from the state described by F_0 and $w = 0$.* The substitution of Eq. (2.6) into Eqs. (2.2) and (2.3) yields a set of equations which are then linearized with respect to the incremental functions F_1 and w. In this way, the system (2.2) and (2.3) reduces to

$$D\nabla^4 w + m(\partial^2 w/\partial t^2) = p_1 + (\partial^2 F_0/\partial y^2) \times (\partial^2 w/\partial x^2) + (\partial^2 F_0/\partial x^2)(\partial^2 w/\partial y^2) - 2(\partial^2 F_0/\partial x\partial y)(\partial^2 w/\partial x\partial y) + (\partial^2 z/\partial x^2)(\partial^2 F_1/\partial y^2) + (\partial^2 z/\partial y^2)(\partial^2 F_1/\partial x^2) - 2(\partial^2 z/\partial x\partial y)(\partial^2 F_1/\partial x\partial y) \tag{2.7}$$

$$\nabla^4 F_1 = -Eh[(\partial^2 z/\partial x^2)(\partial^2 w/\partial y^2) + (\partial^2 z/\partial y^2) \times (\partial^2 w/\partial x^2) - 2(\partial^2 z/\partial x\partial y)(\partial^2 w/\partial x\partial y)] \tag{2.8}$$

In arriving at Eqs. (2.7) and (2.8), we have made explicit use of Eq. (2.5).

Specialization to the Circular Cylindrical Shell

Eqs. (2.7) and (2.8) are now specialized to the case of a circular cylindrical shell by setting

$$z/H = 1 - (y^2/b^2) \tag{2.9}$$

or

$$z = H - (y^2/2a) \tag{2.10}$$

where H is the rise of the shell, b its half width, and a is the meridional radius of curvature. A comparison of Eqs. (2.9) and (2.10) shows that the rise H, width $2b$, and radius a are related as

$$b^2 = 2Ha \tag{2.11}$$

We now imagine that the complete cylindrical shell, of which the shallow portion of projected width $2b$ is a part, deforms according to the pattern $\cos n\theta$. Furthermore, we stipulate that the region $-\pi/2 \leq n\theta \leq \pi/2$ corresponds to the region $-b \leq y \leq b$ and therefore, in view of the shallowness of this portion, we have

$$y = a\theta \tag{2.12}$$

and thus

$$b = \pi a/2n \tag{2.13}$$

Eqs. (2.7) and (2.8), with z given by Eq. (2.10), now assume the following form:

$$D\nabla^4 w + m(\partial^2 w/\partial t^2) = p_1 + (\partial^2 F_0/\partial y^2) \times (\partial^2 w/\partial x^2) + (\partial^2 F_0/\partial x^2)(\partial^2 w/\partial y^2) - 2 \times (\partial^2 F_0/\partial x\partial y)(\partial^2 w/\partial x\partial y) - (1/a)(\partial^2 F_1/\partial x^2) \tag{2.14}$$

$$\nabla^4 F_1 = (Eh/a)(\partial^2 w/\partial x^2) \tag{2.15}$$

We finally stipulate that, for the class of problems under consideration here, $\partial^2 F_0/\partial x\partial y = 0$; i.e., the load intensity p_0 does not give rise to shearing stresses N_{xy0}. In addition, anticipating a result from Section (3), we write for the fluctuating pressure component p_1,

$$p_1 = -m_f(\partial^2 w/\partial t^2) \tag{2.16}$$

Eq. (2.16) states that the interaction pressure exerted by the internal fluid may be considered as an apparent mass contribution, m_f, to the mass per unit area of the shell. In view of Eq. (2.16) and the fact that $\partial^2 F_0 \div \partial x\partial y = 0$, Eqs. (2.14) and (2.15) become

$$D\nabla^4 w + (m + m_f)(\partial^2 w/\partial t^2) = N_{x0}(\partial^2 w/\partial x^2) + N_{y0}(\partial^2 w/\partial y^2) - (1/a)(\partial^2 F_1/\partial x^2) \tag{2.17}$$

$$\nabla^4 F_1 = (Eh/a)(\partial^2 w/\partial x^2) \tag{2.18}$$

We note that for a constant internal pressure p_0, the quantities N_{x0} and N_{y0} are constants. In particular, for a shell with closed ends,

$$N_{y0} = p_0 a, \quad N_{x0} = (1/2)p_0 a \tag{2.19}$$

The Frequency Equation

We now assume that the motions of the shell wall are such that w and F_1 have the form

$$w = A \sin(\pi x/L) \cos(ny/a) \sin \omega t \tag{2.20}$$

$$F_1 = B \sin(\pi x/L) \cos(ny/a) \sin \omega t \tag{2.21}$$

Substitution of Eqs. (2.20) and (2.21) into Eqs. (2.17) and (2.18) yields the following two simultaneous algebraic equations for the coefficients A and B:

$$A\{D[(\pi/L)^2 + (n/a)^2]^2 + N_{x0}(\pi/L)^2 + N_{y0} \times (n/a)^2 - (m + m_f)\omega^2\} - B\{(1/a)(\pi/L)^2\} = 0 \tag{2.22}$$

$$A\{(1/a)(\pi/L)^2\} + B\{(1/Eh)[(\pi/L)^2 + (n/a)^2]^2\} = 0 \tag{2.23}$$

The vanishing of the determinant of the system (2.22) and (2.23) leads to the following frequency equation:

$$(m + m_f)\omega^2 = \frac{Eh}{a^2}\frac{(\pi/L)^4}{[(\pi/L)^2 + (n/a)^2]^2} + D\left[\left(\frac{\pi}{L}\right)^2 + \left(\frac{n}{a}\right)^2\right]^2 + N_{x0}\left(\frac{\pi}{L}\right)^2 + N_{y0}\left(\frac{n}{a}\right)^2 \tag{2.24}$$

* $w = 0$ must be replaced by a more general expression unless $\nabla^4 F_0 = 0$. In what follows, we assume that $\nabla^4 F_0 = 0$.

The first term on the right in Eq. (2.24) represents the effect of membrane action, the second term the effect of wall bending, and the third term the effect of the pressure p_0.

Due to the simple form of Eq. (2.24), we can easily draw conclusions concerning the relative importance of the various terms. With regard to pressurized cylinders, the conclusion that is of most interest is as follows. If N_{x0} is of the same order as N_{y0}, then wall bending will have a negligible effect on the frequency, as compared to the effect of p_0, providing

$$N_{y0}[(\pi/L)^2 + (n/a)^2] \gg D[(\pi/L)^2 + (n/a)^2]^2 \quad (2.25)$$

or, with $N_{y0} = p_0 a$, $D = Eh^3/12(1 - \nu^2)$,

$$(E/p_0)\ (h/a)^3 \ll 12(1 - \nu^2)/[n^2 + (\pi a/L)^2] \quad (2.26)$$

If we assume that the order-of-magnitude relation (2.26) is satisfied, then Eq. (2.24) reduces to

$$(m + m_f)\omega^2 = \frac{Eh}{a^2}\,\frac{(\pi/L)^4}{[(\pi/L)^2 + (h/a)^2]^2} + N_{x0}\left(\frac{\pi}{L}\right)^2 + N_{y0}\left(\frac{n}{a}\right)^2 \quad (2.27)$$

(3) Small Oscillations of a Compressible Circular Cylindrical Fluid Column

General Theory

Assuming small motions of an inviscid compressible fluid and linearized theory, we have as basic equations

$$\rho_0(\partial v_x/\partial t) = -(\partial p/\partial x) \quad (3.1)$$

$$\rho_0(\partial v_r/\partial t) = -(\partial p/\partial r) \quad (3.2)$$

Table 1. Values of $K = \omega a\sqrt{\frac{\rho}{C}}$

$\frac{\rho_0 a}{\rho h} = 0.200$, $C = 4.000$, $\Omega = 0$

n \ λ	π/10	π/4	π/2	3π/4	π	3π/2	2π
2	0.03750	0.2026	0.6163	0.8772	1.018	1.284	1.435
	0.08047	0.5256	0.7234	1.077	1.231	1.478	1.783
	0.7949	0.8169	0.9035	1.788	1.863	2.050	2.308
	0.03932	0.2182	0.6230	0.9491	1.162	1.384	1.483
3	0.01715	0.1015	0.3405	0.5938	0.8250	1.128	1.300
	1.077	1.092	1.146	1.231	1.342	1.610	1.914
	2.013	2.021	2.049	2.096	2.160	2.333	2.554
	0.01771	0.1047	0.3514	0.6230	0.8541	1.162	1.330
4	0.009771	0.05918	0.2131	0.4112	0.6093	0.9299	1.142
	1.353	1.365	1.407	1.475	1.566	1.798	2.077
	2.329	2.335	2.360	2.401	2.457	2.609	2.809
	0.01001	0.06062	0.2182	0.4207	0.6230	0.9491	1.162
5	0.006297	0.03857	0.1439	0.2913	0.4541	0.7557	0.9854
	1.625	1.635	1.672	1.727	1.804	2.008	2.262
	2.637	2.643	2.665	2.701	2.751	2.888	3.069
	0.006421	0.03932	0.1467	0.2967	0.4622	0.7682	0.9998
6	0.004392	0.02707	0.1031	0.2148	0.3461	0.6144	0.8434
	1.879	1.888	1.918	1.968	2.037	2.224	2.457
	2.941	2.946	2.966	2.998	3.043	3.167	3.333
	0.004465	0.02751	0.1047	0.2182	0.3514	0.6230	0.8541

Table 2. Values of $K = \omega a\sqrt{\frac{\rho}{C}}$

$\frac{\rho_0 a}{\rho h} = 0.200$, $C = 4.000$, $\Omega = \frac{1}{400}$

n \ λ	π/10	π/4	π/2	3π/4	π	3π/2	2π
2	0.08500	0.2054	0.5823	0.8570	1.028	1.300	1.453
	0.7953	0.8174	0.9047	1.074	1.237	1.624	1.785
	1.687	1.696	1.731	1.788	1.864	2.061	2.308
	0.1080	0.2416	0.6334	0.9580	1.172	1.397	1.503
3	0.1068	0.1792	0.3739	0.6199	0.8482	1.147	1.326
	1.077	1.092	1.146	1.232	1.343	1.611	1.915
	2.013	2.021	2.049	2.096	2.160	2.333	2.554
	0.1515	0.1850	0.3861	0.6462	0.8743	1.183	1.357
4	0.1715	0.1974	0.2941	0.4623	0.6488	0.9639	1.179
	1.353	1.365	1.407	1.475	1.566	1.799	2.078
	2.329	2.336	2.360	2.401	2.457	2.609	2.809
	0.2006	0.2108	0.3011	0.4732	0.6637	0.9842	1.200
5	0.2407	0.2532	0.2895	0.3895	0.5275	0.8112	1.039
	1.626	1.636	1.671	1.728	1.805	2.009	2.263
	2.637	2.643	2.665	2.701	2.751	2.888	3.069
	0.2503	0.2546	0.2951	0.3969	0.5371	0.8248	1.054
6	0.2812	0.2986	0.3174	0.3742	0.4680	0.7013	0.9202
	1.882	1.890	1.921	1.973	2.040	2.224	2.457
	2.941	2.946	2.966	2.998	3.043	3.167	3.333
	0.3002	0.3025	0.3226	0.3802	0.4752	0.7113	0.9321

Table 3. Values of $K = \omega a\sqrt{\frac{\rho}{C}}$

$\frac{\rho_0 a}{\rho h} = 0.200$, $C = 4.00$, $\Omega = \frac{1}{200}$

n \ λ	π/10	π/4	π/2	3π/4	π	3π/2	2π
2	0.1074	0.2471	0.5992	0.8570	1.026	1.300	1.470
	0.7958	0.8179	0.9060	1.076	1.242	1.499	1.787
	1.687	1.696	1.731	1.788	1.864	2.062	2.308
	0.1476	0.2630	0.6437	0.9668	1.181	1.411	1.522
3	0.2010	0.2171	0.3989	0.6459	0.8693	1.195	1.351
	1.078	1.093	1.147	1.233	1.344	1.613	1.916
	2.013	2.021	2.049	2.096	2.160	2.333	2.554
	0.2134	0.2398	0.4179	0.6686	0.8940	1.205	1.382
4	0.2693	0.2664	0.3570	0.5083	0.6860	0.9966	1.214
	1.354	1.366	1.408	1.476	1.567	1.799	2.079
	2.329	2.336	2.360	2.401	2.457	2.609	2.809
	0.2835	0.2919	0.3657	0.5204	0.7020	1.018	1.237
5	0.3419	0.3420	0.3832	0.4674	0.5918	0.8631	1.090
	1.626	1.636	1.671	1.728	1.805	2.009	2.263
	2.637	2.644	2.665	2.701	2.751	2.888	3.069
	0.3540	0.3579	0.3908	0.4764	0.6028	0.8778	1.106
6	0.4029	0.4122	0.4279	0.4836	0.5640	0.7784	0.9911
	1.884	1.892	1.923	1.975	2.044	2.229	2.462
	2.941	2.946	2.966	2.998	3.043	3.167	3.333
	0.4246	0.4270	0.4440	0.4914	0.5728	0.7897	1.004

Table 4. Values of $K = \omega a\sqrt{\frac{\rho}{C}}$

$\frac{\rho_0 a}{\rho h} = 0.200$, $C = 4.00$, $\Omega = \frac{1}{100}$

n \ λ	π/10	π/4	π/2	3π/4	π	3π/2	2π
2	0.1627	0.2715	0.6164	0.8754	1.034	1.311	1.502
	0.7967	0.8189	0.9086	1.074	1.255	1.510	1.792
	1.687	1.696	1.731	1.788	1.864	2.054	2.298
	0.2050	0.3011	0.6637	0.9842	1.200	1.437	1.561
3	0.2719	0.3159	0.4629	0.7078	0.8979	1.204	1.399
	1.079	1.094	1.148	1.234	1.347	1.615	1.918
	2.013	2.021	2.049	2.096	2.161	2.333	2.554
	0.3013	0.3226	0.4752	0.7113	0.9321	1.246	1.434
4	0.3807	0.4013	0.4527	0.5890	0.7547	1.059	1.282
	1.355	1.367	1.409	1.477	1.568	1.801	2.080
	2.329	2.336	2.360	2.401	2.457	2.610	2.809
	0.4007	0.4084	0.4690	0.6039	0.7730	1.083	1.307
5	0.4814	0.4956	0.5260	0.5896	0.7027	0.9583	1.184
	1.627	1.637	1.672	1.729	1.806	2.010	2.264
	2.637	2.644	2.665	2.701	2.751	2.888	3.070
	0.5005	0.5046	0.5328	0.6048	0.7162	0.9753	1.203
6	0.5680	0.5770	0.6011	1.6490	0.7183	0.9132	1.119
	1.892	1.900	1.930	1.982	2.051	2.231	2.461
	2.941	2.946	2.966	2.998	3.043	3.167	3.334
	0.6004	0.6032	0.6191	0.6598	0.7299	0.9269	1.134

$$\rho_0(\partial v_\theta/\partial t) = -(1/r)\,(\partial p/\partial\theta) \tag{3.3}$$

$$p - p_0 = c_0^2(\rho - \rho_0) \tag{3.4}$$

$$(\partial\rho/\partial t) + \rho_0\{(1/2)\,[\partial(rv_r)/\partial r] + (1/r)\,(\partial v_\theta/\partial\theta) + (\partial v_x/\partial x)\} = 0 \tag{3.5}$$

where

x, r, θ	=	cylindrical coordinates
v_x, v_r, v_θ	=	velocity components
p_0	=	reference pressure
ρ_0	=	reference density
c_0	=	reference sound velocity, $[(dp/d\rho)_0 = c_0^2]$
t	=	time

Eqs. (3.1) to (3.5) may be reduced to a single differential equation for the pressure fluctuation q, defined as

$$q = p - p_0 \tag{3.6}$$

This equation is

$$(\partial^2 q/\partial r^2) + (1/r)\,(\partial q/\partial r) + (1/r^2)\,(\partial^2 q/\partial\theta^2) + (\partial^2 q/\partial x^2) = (1/c_0^2)\,(\partial^2 q/\partial t^2) \tag{3.7}$$

We note that for an incompressible fluid, $c_0 = \infty$; while for typical compressible gases,

$$c_0 \backsimeq 3 \times 10^4 \text{ in./sec.} \tag{3.8}$$

Solutions of Eq. (3.7) which are suitable for our purposes are of the form

$$q = e^{i\omega t} \cos n\theta \sin (\pi x/L) Q(r) \tag{3.9}$$

where L is the axial half-wavelength. Substitution of Eq. (3.9) into Eq. (3.7) yields an ordinary differential equation for $Q(r)$,

$$(d^2Q/dr^2) + (1/r)\,(dQ/dr) - [(\pi^2/L^2) - (\omega^2/c_0^2) + (n^2/r^2)]Q = 0 \tag{3.10}$$

Solutions of Eq. (3.10) which are regular at $r = 0$ are of the form

$$Q(r) = \begin{cases} AI_n[\sqrt{(\pi^2/L^2) - (\omega^2/c_0^2)}\,r], & \omega/c_0 \le \pi/L \\ AJ_n[\sqrt{(\omega^2/c_0^2) \pm (\pi^2/L^2)}\,r], & \omega/c_0 \ge \pi/L \end{cases} \tag{3.11}$$

where J_n is the Bessel function of the first kind and I_n is the modified Bessel function of the first kind.

Expression for an Apparent Mass Factor

For purposes of determining the interaction effects between the fluid and oscillating shell, we express the fluctuating pressure q at the radius $r = a$ of the fluid column in terms of the radial acceleration $\partial v_r/\partial t$ at $r = a$. In view of Eq. (3.6), Eq. (3.2) becomes

$$\partial v_r/\partial t = -(1/\rho_0)\,(\partial q/\partial r) \tag{3.12}$$

therefore, with

$$q = A\{I_n, J_n\} \cos n\theta \sin (\pi x/L) e^{i\omega t} \tag{3.13}$$

Eq. (3.12) becomes

$$\partial v_r/\partial t = -(A/\rho_0) \begin{Bmatrix} \sqrt{(\pi^2/L^2) - (\omega^2/c_0^2)}\,I_n' \\ \sqrt{(\omega^2/c_0^2) - (\pi^2/L^2)}\,J_n' \end{Bmatrix} \times \cos n\theta \sin (\pi x/L) e^{i\omega t} \tag{3.14}$$

where a prime denotes differentiation with respect to the argument of I_n or J_n. Eqs. (3.13) and (3.14) may be combined to yield the following expression for $q(a)$, the fluctuating pressure at $r = a$, in terms of $\dot{v}_r(a)$, the radial acceleration at $r = a$:

$$q(a) = -\rho_0 a \dot{v}_r(a) \begin{cases} \dfrac{I_n(\sqrt{\lambda^2 - k^2})}{\sqrt{\lambda^2 - k^2}\,I_n'\,(\sqrt{\lambda^2 - k^2})}, & k < \lambda \\ \dfrac{J_n(\sqrt{k^2 - \lambda^2})}{\sqrt{k^2 - \lambda^2}\,J_n'\,(\sqrt{k^2 - \lambda^2})}, & k > \lambda \end{cases} \tag{3.15}$$

Table 5. Values of $K = \omega a\sqrt{\frac{\rho}{C}}$

$\frac{\rho_0 a}{\rho h} = 0.4640$, $C = 9.300$, $\Lambda = 0$

n \ λ	π/10	π/4	π/2	3π/4	π	3π/2	2π
2	0.03380	0.1914	0.3563	0.4095	0.4672	0.6002	0.7468
	0.3561	0.3752	0.6134	0.7513	0.7899	0.8768	0.9834
	0.7300	0.7348	0.7636	0.9473	1.089	1.174	1.256
	0.03932	0.2182	0.6230	0.9491	1.162	1.384	1.483
3	0.01649	0.09742	0.3185	0.4823	0.5496	0.6705	0.8046
	0.4753	0.4826	0.5188	0.6485	0.8316	0.9839	1.084
	0.8697	0.8732	0.8866	0.9112	0.9571	1.163	1.307
	0.01771	0.1047	0.3514	0.6230	0.8541	1.162	1.330
4	0.009478	0.05741	0.2062	0.3928	0.5598	0.7370	0.8663
	0.5930	0.5982	0.6182	0.6556	0.7234	0.9519	1.129
	1.005	1.008	1.019	1.037	1.063	1.138	1.245
	0.01001	0.06062	0.2182	0.4207	0.6230	0.9491	1.162
5	0.006143	0.03763	0.1404	0.2836	0.4396	0.7129	0.8948
	0.7094	0.7136	0.7291	0.7555	0.7929	0.9028	1.052
	1.138	1.140	1.150	1.166	1.187	1.248	1.335
	0.006421	0.03932	0.1467	0.2967	0.4622	0.7682	0.9998
6	0.004302	0.02651	0.1010	0.2104	0.3378	0.5950	0.8037
	0.8286	0.8322	0.8449	0.8658	0.8962	0.9761	1.084
	1.268	1.270	1.279	1.293	1.312	1.351	1.433
	0.004465	0.02751	0.1047	0.2182	0.3514	0.6230	0.8541

Table 6. Values of $K = \omega a\sqrt{\frac{\rho}{C}}$

$\frac{\rho_0 a}{\rho h} = 0.4640$, $C = 9.300$, $\Lambda = \frac{1}{400}$

n \ λ	π/10	π/4	π/2	3π/4	π	3π/2	2π
2	0.09674	0.2099	0.3569	0.4096	0.4673	0.6002	0.7470
	0.3581	0.3787	0.6214	0.7519	0.7901	0.8770	0.9837
	0.7301	0.7350	0.7650	0.9544	1.092	1.174	1.257
	0.1080	0.2416	0.6334	0.9580	1.172	1.397	1.503
3	0.1403	0.1712	0.3460	0.4871	0.5507	0.6710	0.8051
	0.4776	0.4850	0.5244	0.6653	0.8450	0.9856	1.085
	0.8699	0.8735	0.8869	0.9121	0.9620	1.179	1.324
	0.1515	0.1850	0.3861	0.6462	0.8743	1.183	1.357
4	0.1890	0.1988	0.2831	0.4380	0.5691	0.7411	0.8687
	0.5954	0.6006	0.6211	0.6611	0.7377	0.9784	1.149
	1.006	1.009	1.019	1.038	1.064	1.142	1.258
	0.2006	0.2108	0.3011	0.4732	0.6637	0.9842	1.200
5	0.2386	0.2427	0.2814	0.3775	0.5076	0.7518	0.9148
	0.7118	0.7161	0.7317	0.7586	0.7976	0.9179	1.086
	1.138	1.141	1.150	1.166	1.188	1.249	1.331
	0.2503	0.2546	0.2951	0.3969	0.5371	0.8248	1.054
6	0.2883	0.2905	0.3099	0.3653	0.4560	0.6781	0.8791
	0.8286	0.8322	0.8449	0.8678	0.8982	0.9807	1.094
	1.268	1.271	1.279	1.293	1.313	1.367	1.440
	0.3002	0.3025	0.3226	0.3802	0.4752	0.7113	0.9321

Table 7. Values of $K = \omega a\sqrt{\frac{\rho}{G}}$

$\frac{\rho_o a}{\rho h} = 0.4640$, $C = 9.300$, $\Omega = \frac{1}{200}$

n \ λ	π/10	π/4	π/2	3π/4	π	3π/2	2π
2	0.1313	0.2260	0.3574	0.4097	0.4674	0.6003	0.7471
	0.3604	0.3827	0.6291	0.7524	0.7903	0.8771	0.9839
	0.7303	0.7352	0.7665	0.9613	1.094	1.175	1.258
	0.1476	0.2630	0.6437	0.9668	1.181	1.411	1.522
3	0.1965	0.2205	0.3695	0.4908	0.5516	0.6713	0.8056
	0.4803	0.4879	0.5313	0.6822	0.8570	0.9870	1.086
	0.8702	0.8737	0.8873	0.9130	0.9679	1.196	1.342
	0.2134	0.2398	0.4179	0.6686	0.8940	1.205	1.382
4	0.2657	0.2737	0.3417	0.4762	0.6019	0.7451	0.8706
	0.5983	0.6036	0.6248	0.6683	0.7570	1.003	1.164
	1.006	1.009	1.020	1.038	1.066	1.146	1.276
	0.2835	0.2919	0.3657	0.5204	0.7020	1.018	1.237
5	0.3357	0.3395	0.3707	0.4504	0.5647	0.7809	0.9275
	0.7150	0.7192	0.7350	0.7627	0.8040	0.9406	1.121
	1.138	1.141	1.151	1.166	1.188	1.251	1.334
	0.3540	0.3579	0.3908	0.4764	0.6028	0.8778	1.106
6	0.4059	0.4083	0.4247	0.4699	0.5468	0.7463	0.9318
	0.8308	0.8344	0.8481	0.8699	0.8991	0.9890	1.110
	1.269	1.271	1.280	1.294	1.313	1.368	1.441
	0.4246	0.4270	0.4440	0.4914	0.5728	0.7897	1.004

Table 8. Values of $K = \omega a\sqrt{\frac{\rho}{G}}$

$\frac{\rho_o a}{\rho h} = 0.4640$, $C = 9.300$, $\Omega = \frac{1}{100}$

n \ λ	π/10	π/4	π/2	3π/4	π	3π/2	2π
2	0.1795	0.2521	0.3584	0.4099	0.4675	0.6005	0.7474
	0.3659	0.3925	0.6438	0.7533	0.7906	0.8773	0.9842
	0.7307	0.7357	0.7701	0.9750	1.098	1.176	1.259
	0.2050	0.3011	0.6637	0.9842	1.200	1.437	1.561
3	0.2731	0.2916	0.4075	0.4963	0.5531	0.6720	0.8063
	0.4875	0.4957	0.5533	0.7155	0.8763	0.9891	1.087
	0.8707	0.8743	0.8881	0.9155	0.9845	1.226	1.359
	0.3013	0.3226	0.4752	0.7113	0.9321	1.246	1.434
4	0.3701	0.3772	0.4301	0.5340	0.6245	0.7483	0.8733
	0.6069	0.6122	0.6358	0.6611	0.7995	1.046	1.181
	1.006	1.009	1.020	1.039	1.067	1.161	1.322
	0.4007	0.4084	0.4690	0.6039	0.7730	1.083	1.307
5	0.4679	0.4719	0.4979	0.5614	0.6521	0.8142	0.9413
	0.7246	0.7289	0.7453	0.7761	0.8348	0.9994	1.192
	1.139	1.142	1.151	1.167	1.190	1.253	1.343
	0.5005	0.5046	0.5328	0.6048	0.7162	0.9753	1.203
6	0.5661	0.5689	0.5842	0.6218	0.6848	0.8479	0.9960
	0.8393	0.8429	0.8555	0.8812	0.9141	1.021	1.172
	1.270	1.272	1.280	1.295	1.314	1.370	1.444
	0.6004	0.6032	0.6191	0.6598	0.7299	0.9269	1.134

Table 9. Values of $K = \omega a\sqrt{\frac{\rho}{G}}$

$\frac{\rho_o a}{\rho h} = 300.0$, $C = 2.500$, $\Omega = 0$

n \ λ	π/10	π/4	π/2	3π/4	π	3π/2	2π
2	0.003213	0.01820	0.05537	0.09171	0.1226	0.1714	0.2095
	2.051	2.071	2.142	2.255	2.404	2.784	3.243
	3.358	3.370	3.414	3.486	3.584	3.850	4.194
	0.03932	0.2182	0.6230	0.9491	1.162	1.384	1.483
3	0.001766	0.01055	0.03664	0.06828	0.09918	0.1521	0.1942
	2.547	2.563	2.620	2.713	2.838	3.167	3.577
	3.893	3.904	3.942	4.004	4.090	4.325	4.633
	0.01771	0.1047	0.3514	0.6230	0.8541	1.162	1.330
4	0.001150	0.007006	0.02576	0.05130	0.07908	0.1318	0.1765
	3.028	3.042	3.090	3.169	3.276	3.565	3.934
	4.413	4.422	4.456	4.511	4.587	4.798	5.078
	0.01001	0.06062	0.2182	0.4207	0.6230	0.9491	1.162
5	0.0008228	0.005060	0.01915	0.03963	0.06353	0.1131	0.1584
	3.499	3.511	3.553	3.622	3.716	3.973	4.307
	4.921	4.929	4.959	5.009	5.077	5.268	5.524
	0.006421	0.03932	0.1467	0.2967	0.4622	0.7682	0.9998
6	0.0006255	0.003866	0.01487	0.03150	0.05184	0.09697	0.1412
	3.963	3.974	4.011	4.072	4.156	4.387	4.692
	5.419	5.427	5.454	5.499	5.562	5.736	5.973
	0.004465	0.02751	0.1047	0.2182	0.3514	0.6230	0.8541

Table 10. Values of $K = \omega a\sqrt{\frac{\rho}{G}}$

$\frac{\rho_o a}{\rho h} = 300.0$, $C = 2.500$, $\Omega = \frac{1}{400}$

n \ λ	π/10	π/4	π/2	3π/4	π	3π/2	2π
2	0.008827	0.02015	0.05630	0.09257	0.1236	0.1731	0.2123
	0.1080	0.2416	0.6334	0.9580	1.172	1.397	1.503
3	0.01510	0.01864	0.04026	0.07082	0.1015	0.1549	0.1981
	0.1515	0.1850	0.3861	0.6462	0.8743	1.183	1.357
4	0.02303	0.02436	0.03556	0.05771	0.08424	0.1367	0.1823
	0.2006	0.2108	0.3011	0.4732	0.6637	0.9842	1.200
5	0.03208	0.03276	0.03853	0.05299	0.07382	0.1214	0.1670
	0.2503	0.2546	0.2951	0.3969	0.5371	0.8248	1.054
6	0.04206	0.04251	0.04580	0.05489	0.07010	0.1107	0.1541
	0.3002	0.3025	0.3226	0.3802	0.4752	0.7113	0.9321

Table 11. Values of $K = \omega a\sqrt{\frac{\rho}{G}}$

$\frac{\rho_o a}{\rho h} = 300.0$, $C = 2.500$, $\Omega = \frac{1}{200}$

n \ λ	π/10	π/4	π/2	3π/4	π	3π/2	2π
2	0.01206	0.02193	0.05721	0.09342	0.1246	0.1748	0.2151
	0.1476	0.2630	0.6437	0.9668	1.181	1.411	1.522
3	0.02128	0.02416	0.04358	0.07327	0.1038	0.1576	0.2020
	0.2134	0.2398	0.4179	0.6686	0.8940	1.205	1.382
4	0.03255	0.03374	0.04318	0.06347	0.08910	0.1413	0.1878
	0.2835	0.2919	0.3657	0.5204	0.7020	1.018	1.237
5	0.04535	0.04605	0.05101	0.06361	0.08284	0.1292	0.1752
	0.3540	0.3579	0.3908	0.4764	0.6028	0.8778	1.106
6	0.05948	0.05999	0.06304	0.07094	0.08450	0.1229	0.1660
	0.4246	0.4270	0.4440	0.4914	0.5728	0.7897	1.004

Table 12. Values of $K = \omega a\sqrt{\frac{\rho}{G}}$

$\frac{\rho_o a}{\rho h} = 300.0$, $C = 2.500$, $\Omega = \frac{1}{100}$

n \ λ	π/10	π/4	π/2	3π/4	π	3π/2	2π
2	0.01675	0.02511	0.05898	0.09509	0.1266	0.1781	0.2205
	0.2050	0.3011	0.6637	0.9842	1.200	1.437	1.561
3	0.03004	0.03250	0.04955	0.07795	0.1082	0.1630	0.2094
	0.3013	0.3226	0.4752	0.7113	0.9321	1.246	1.434
4	0.04602	0.04719	0.05536	0.07364	0.09809	0.1503	0.1985
	0.4007	0.4084	0.4690	0.6039	0.7730	1.083	1.307
5	0.06413	0.06492	0.06955	0.08075	0.09842	0.1435	0.1905
	0.5005	0.5046	0.5328	0.6048	0.7162	0.9753	1.203
6	0.08410	0.08474	0.08790	0.09524	0.1077	0.1442	0.1875
	0.6004	0.6032	0.6191	0.6598	0.7299	0.9269	1.134

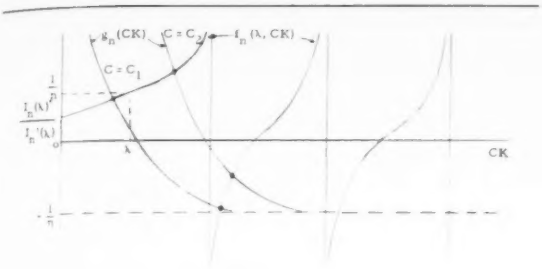

FIG. 1.

where $$k = \omega a/c_0 \tag{3.16}$$

is a reduced frequency and $\lambda = \pi a/L$. Eq. (3.15) may be rewritten in the form

$$q(a) = -\rho_0 a f_n(\lambda, k)\ddot{w} \tag{3.17}$$

where $f_n(\lambda, k)$ is defined by reference to Eq. (3.15) and w is the radial deflection at the surface of the fluid column—i.e., $\dot{w} = v_r(a)$.

The fluid column and the elastic shell are now coupled by imposing continuity requirements at the interface of the fluid and the surrounding shell. These requirements are

$$p_1 = q(a),\ \ddot{w}_{\text{shell}} = \ddot{w}_{\text{fluid}} = \ddot{w} \tag{3.18}$$

In view of Eq. (2.16) we then have for the apparent mass contribution m_f in Eq. (2.24),

$$m_f = \rho_0 a f_n(\lambda, k) \tag{3.19}$$

(4) Frequencies of the Combined Cylinder – Fluid Column System

Some General Conclusions

In order to facilitate a discussion of the effect that an internal fluid has on the frequencies of a cylindrical shell, we recast Eq. (2.24) as follows. Let

$$\left.\begin{aligned} &\Omega = \rho_0 a/Gh,\quad K = \omega a\sqrt{\rho_s/G} = \omega a/c_s, \\ &\qquad\qquad C = c_s/c_0,\quad k = CK, \\ &m = \rho_s h,\quad \lambda = \pi a/L,\quad N_{y0} = p_0 a, \\ &\qquad\qquad N_{x0} = (1/2)p_0 a,\quad \eta = \rho_0 a/\rho_s h \end{aligned}\right\} \tag{4.1}$$

where $G = E/2(1 + \nu)$ is the shear modulus and ρ_s is the density of the shell material. Using the definitions provided by Eqs. (3.19) and (4.1), we rewrite Eq. (2.24) in the form

$$K^2[1 + \eta f_n(\lambda, CK)] = (8/3)\ [\lambda^4/(n^2 + \lambda^2)^2] + (1/4)\ (h/a)^2\ (\lambda^2 + n^2)^2 + \Omega[n^2 + (1/2)\lambda^2] \tag{4.2}$$

where we have assumed that Poisson's ratio has the value 1/3. We now let

$$\bar{K}_n^2 = (8/3)\ [\lambda^4/(n^2 + \lambda^2)^2] + (1/4)\ (h/a)^2 \times (\lambda^2 + n^2)^2 + \Omega[n^2 + (1/2)\lambda^2] \tag{4.3}$$

or, if the order-of-magnitude relation (2.26) is satisfied,

$$\bar{K}_n^2 = (8/3)\ [\lambda^4/(n^2 + \lambda^2)^2] + \Omega[n^2 + (1/2)\lambda^2] \tag{4.4}$$

$\bar{K}_n$ is the value of the frequency parameter K for a pressurized shell vibrating in vacuo. Finally, we write Eq. (4.2) in the form

$$f_n(\lambda, CK) = (1/\eta)\ [(C^2\bar{K}_n^2/C^2K^2) - 1] \tag{4.5}$$

or if, for the sake of brevity, we define

$$g_n(CK) = (1/\eta)\ [(C^2\bar{K}_n^2/C^2K^2) - 1] \tag{4.6}$$

then $$f_n(\lambda, CK) = g_n(CK) \tag{4.7}$$

When both sides of Eq. (4.7) are plotted against CK, a system of curves similar to that shown in Fig. 1 is obtained.

The solutions of Eq. (4.7) are those values of CK at which the curve $g_n(CK)$, see Fig. 1, intersects the various branches of the curve $f_n(\lambda, CK)$.

Referring to Fig. 1, the following qualitative observations may be made.

(1) The intersection of the g_n-curve with the CK-axis gives the value of the frequency parameter K in the absence of any inertia effect of the internal fluid.

(2) The intersections of the f_n-curve with the CK-axis give the values of the frequency parameter K for vibrations of the fluid column in the absence of the surrounding thin shell. The first intersection corresponds to a vibration with one nodal circle, the second to a vibration with two nodal circles, and so on. The existence of these vibrations depends on finite compressibility of the fluid.

(3) The values of CK at which f_n becomes infinite give the values of the frequency parameter K for vibrations of the fluid column if the surrounding cylindrical shell is assumed to be rigid. The existence of these vibrations also depends on finite compressibility of the fluid.

(4) The lowest frequency of the fluid vibration with rigid enclosing cylinder has a lower value than the corresponding frequency for the fluid column with a free cylindrical boundary.

(5) The effect of inertia and compressibility of an internal fluid is to *lower* the frequency of the wall vibrations of the shell in comparison with the value of this frequency when inertia and compressibility of the internal fluid are absent. In addition to this lowered frequency, there occur higher frequencies each of which is associated with a particular number of nodal circles in the oscillating fluid.

An Approximate Frequency Formula for Heavy Liquids

Inspection of Fig. 1 reveals that as the value of the mass ratio η increases, the lowest value of the frequency parameter decreases. When η is quite large, we may with good approximation replace the actual value of the function f_n by its value for $K = 0$ and determine K from the relation

$$K = \bar{K}_n/\sqrt{\eta f_n(\lambda, 0) + 1} \tag{4.8}$$

The second term inside the square root will be negligible, and we have in first approximation, when $1 \ll \eta$,

the following formula:

$$K = \bar{K}_n/\sqrt{\eta[I_n(\lambda)/\lambda I_n'(\lambda)]} \qquad (4.9)$$

for that frequency of vibration which takes place when no nodal circles are present in the fluid.

We also note that the higher frequencies, for vibrations with nodal circles, are very nearly equal to the frequencies of vibration of the free-boundary column of liquid.

Numerical Results for Some Special Cases

The first three roots of Eq. (4.5) have been obtained for some specific values of $\eta = \rho_0 a/\rho_s h$, $C = c_s/c_0$, and $\bar{K}_n$. The computations were carried out for the following three pairs of values of η and C:

$$\eta = 0.200, \quad C = 4.0;$$
$$\eta = 0.464, \quad C = 9.3;$$
$$\eta = 300.0, \quad C = 2.5$$

and for values of $\bar{K}_n$, as defined by Eq. (4.4), associated with the following values of N, λ, and Ω:

$$n = 2, 3, 4, 5, 6;$$
$$\Omega = p_i a/Gh = 0, 1/400, 1/200, 1/100;$$
$$\lambda = \pi a/L = \pi/10, \pi/4, \pi/2, \pi, 3\pi/2, 2\pi$$

The results of these computations are presented in Tables 1 through 12. The four rows for each value of n in these tables have the following significance: the first three rows represent vibrations with zero, one, and two nodal circles in the fluid, respectively; the fourth row contains the corresponding value of $\bar{K}_n$, which holds when inertia and compressibility of the internal fluid column are neglected. A comparison of the numerical values in the first and in the fourth rows shows that the effects which are determined in this report may be quite appreciable.

Tables 10, 11, and 12 contain only the values of K corresponding to the first root of Eq. (4.5) and $\bar{K}_n$. The second and third roots of Eq. (4.5) are the same, to within four figures, for all values of Ω considered here—i.e., the same as given in Table 9.

REFERENCES

[1] Reissner, E., *Notes on the Vibrations of Thin, Pressurized, Cylindrical Shells*, The Ramo-Wooldridge Corporation, Report No. AM 5-4, November, 1955.

[2] Fung, Y. C., Sechler, E. E., and Kaplan, A., *On the Vibration of Thin Cylindrical Shells Under Internal Pressure*, Journal of the Aeronautical Sciences, Vol. 24, No. 9, pp. 650–660, September, 1957.

[3] Reissner, E., *Nonlinear Effects in Vibrations of Cylindrical Shells*, The Ramo-Wooldridge Corporation, Report No. AM 5-6, September, 1955.

[4] Reissner, E., *On Transverse Vibrations of Thin, Shallow, Elastic Shells*, Quarterly of Applied Mathematics, Vol. 13, pp. 169–176, 1955.

IAS Twenty-Seventh Annual Meeting

Hotel Sheraton-Astor, New York City, January 26–29, 1959

The scope of the meeting will be broad to cover the many fields of interest to IAS members. The meetings committee plans to schedule papers on aerodynamics, hypersonics, aeroelasticity, missiles and rockets, missile propulsion, space propulsion, satellites and spacecraft, space medicine, VTOL/STOL aircraft, rotary wing aircraft, meteorology, etc.

Members or organizations wishing to have papers considered for presentation at this meeting should submit outlines or short abstracts to the Meetings Committee, 2 East 64th St., New York 21, N.Y., no later than August 1, 1958.

Last Call for Roster Listing

All members are reminded to send in their completed Roster Data Cards if they wish to change their listing in the next edition of the Roster. Members whose names do not appear in the 1957–1958 Roster are especially urged to return their cards immediately.

Those members for whom we do not have data cards by May 30 will be listed by repeating the entry that appeared for them in last year's Roster. This is your last opportunity to be listed correctly in the 1958–1959 IAS Roster.

A Power-Spectrum Equation for Stationary Random Gusts, Including a Sample Problem

K. D. SAUNDERS*

Douglas Aircraft Company, Inc.

SUMMARY

A general power-spectrum equation for stationary random gusts is derived on the basis of a mathematical abstraction that models the probability-density distributions of observed meteorological data. The scale and intensity of turbulence are given in terms of the modes and moments of simple probability-density distributions for the magnitude, duration and occurrence. Statistical parameters are tabulated for use to altitudes of 50,000 ft. Extreme spectra are given for clear-sky and thunderstorm gusts.

A sample problem is worked for expected incremental load factors at the c.g. of a swept-wing fighter in flight through low-level random gusts at Mach Number 0.86.

INTRODUCTION

Gust power-spectrum equations are used in getting outputs—e.g., incremental load factors, pitch attitudes, airframe stresses, autopilot outputs, etc.—of an airplane in flight through random gusts. The product of the gust spectrum and the modulus-squared of the transfer function is the output spectrum. The integral of the output spectrum over the frequency half-plane is representable as the variance of the output of a normal distribution with mean zero. The probability of an output exceeding a given value is expressible in terms of the complimentary error function. The expected number of times per second an output passes through a given value is measured by the output spectrum—see, for instance, references 1–9.

POWER SPECTRA

Consider a model of rectangular pulses that satisfy probability-density functions for velocity, duration, and occurrence, $p(v)$, $p(l)$, and $p(n)$. Assume the pulses are uncorrelated so that

$$\overline{(v_i - \bar{v})\,(v_j - \bar{v})} = 0,\ i \neq j \qquad (1)$$
$$= v_i^2,\ i = j$$

Truncate the model in the interval $2T$, $T \to \infty$. Let v_i stand for pulse of duration l at time t_i. Let τ stand for a time shift overlapping v_i with $v_i(t + \tau)$, Fig. 1. Let $R(\tau)_{ri}$ be the autocorrelation of this pulse. Then

$$R(\tau)_{ri} = \frac{1}{2T} \lim_{T \to \infty} \int_{ti+\tau}^{ti+l} v_i^2 dt$$
$$= \frac{1}{2T} \lim_{T \to \infty} (l - |\tau|)v_i^2,\ |\tau| \leq l \qquad (2)$$
$$= 0,\ |\tau| > l$$

Received August 6, 1957.

* Special Assignments Group Leader, Strength and Dynamic Stability Section, Long Beach Engineering Division.

τ takes on the absolute sign since $R(\tau)$ is even. The expected value of $R(\tau)_{ri}$ is

$$R(\tau)_{ri} = \frac{1}{2T} \lim_{T \to \infty} \int_l \int_v p(l)\ (l - |\tau|)p(v)v_i^2 dl\ dv$$

Shifts of τ greater than l add nothing to $R(\tau)_{ri}$ because of Eq. (1), so

$$R(\tau)_{ri} = \frac{1}{2T} \lim_{T \to \infty} \int_{l=|\tau|}^{\infty} \int_{-\infty}^{\infty} p(l) \times (l - |\tau|)p(v)v_i^2 dl\ dv \qquad (3)$$

Now returning to the ensemble of pulses: the expected value of v_i^2 is the variance of v, σ_v^2, $p(n)$ gives the mean $\bar{n}$, and $p(l)$ gives the mean $\bar{l}$. The number of pulses like v_i in an ensemble referenced to an airplane in flight at speed V for time $2T$ is $\bar{n}V2T$. So the autocorrelation for the ensemble is

$$R(\tau) = \bar{n}V\sigma_v^2 \int_{|\tau|}^{\infty} (l - |\tau|)p(l)dl \qquad (4)$$

Let l_m be the mid-point of the least class interval of $p(l)$ and ξ_l be the mode of $p(l)$. Investigations show that the probability-density functions for $p(l)$ are shaped as shown in Fig. 2. These functions fit a $(l - l_m)$ product exponential $(l - l_m)$ function with two undetermined coefficients. To get the function, take $p(l)$ as

$$p(l) = 0,\quad l < l_m$$
$$= a(l - l_m) \exp\left\{-b(l - l_m)\right\},\quad l \geq l_m \qquad (5)$$

then impose constraints

$$\left.\begin{aligned} \int_l p(l)dl &= 1 \\ \frac{d[p(l)]}{dl}\Big)_{l=\xi l} &= 0 \end{aligned}\right\} \qquad (6)$$

From Eqs. (5) and (6) it follows that

$$p(l) = [1/(\xi_l - l_m)^2]\,(l - l_m) \times \exp\left\{-[(l - l_m)/(\xi_l - l_m)]\right\} \qquad (7)$$

Substituting Eq. (7) in Eq. (4), performing the integration, and simplifying gives the autocorrelation of $v(t)$,

$$R(\tau) = \bar{n}V\sigma_v^2\left\{[|\tau|/(\xi_l - l_m)] - [l_m/(\xi_l - l_m)] + 2\right\} \exp\left[-|\tau|/(\xi_l - l_m)\right] \qquad (8)$$

Eq. (8) is the autocorrelation of the ensemble of pulses.

Writing $l_{ms} = Vl_m$, and $\xi_{ls} - l_{ms} = V(\xi_l - l_m)$, and transforming to obtain the power spectrum of $v(t)$, gives

$$W(\omega) = \frac{\bar{n}\sigma_v^2(\xi_{ls} - l_{ms})^2 \exp\left\{l_{ms}/(\xi_{ls} - l_{ms})\right\}}{\pi V\left\{1 + \omega^2[(\xi_{ls} - l_{ms})^2/V^2]\right\}^2}\left\{3 + \omega^2\frac{(\xi_{ls} - l_{ms})^2}{V^2} - \frac{l_{ms}}{\xi_{ls} - l_{ms}}\left[1 + \omega^2\frac{(\xi_{ls} - l_{ms})^2}{V^2}\right]\right\} \quad (9)$$

Now observe that the data-reduction procedures reduce a maximum frequency $\pi V/l_{ms}$. Irregularities smaller than crossing irregularities are not modeled. The sample trace in Fig. 3 demonstrates the filter operation in the reduction of the trace to an ensemble of rectangular gusts. The maximum harmonic of the smoothed trace is shown dashed in. The time trace is smoothed to a maximum frequency content $\pi V/l_{ms}$. Accordingly,

$$W(\omega) \geq W(\pi V/l_{ms}) = 0$$

A filter operation is required on Eq. (9). A natural filter to use is a one-minus-unit-step at $\omega = \pi V/l_{ms}$.

The final form of the power-spectrum equation is

$$W(\omega) = \frac{\bar{n}\sigma_v^2(\xi_{ls} - l_{ms})^2 \exp\left\{l_{ms}/(\xi_{ls} - l_{ms})\right\}}{\pi V[1 + \omega^2(\xi_{ls} - l_{ms})^2/V^2]^2}\left\{3 + \omega^2\frac{(\xi_{ls} - l_{ms})^2}{V^2} - \frac{l_{ms}}{\xi_{ls} - l_{ms}}\left[1 + \omega^2\frac{(\xi_{ls} - l_{ms})^2}{V^2}\right]\right\} \times \left[1 - U\left(\omega - \frac{\pi V}{l_{ms}}\right)\right] \quad (10)$$

For turbulence with small eddies, $l_{ms} \to 0$, and Eq. (10) becomes

$$W(\omega) = \frac{3\bar{n}\sigma_v^2\xi_{ls}^2[1 + (\omega^2\xi_{ls}^2/3V^2)]}{\pi V[1 + (\omega^2\xi_{ls}^2/V^2)]^2} \quad (11)$$

In this form ξ_{ls} is recognized as the scale of turbulence, usually denoted L. The spectrum at $\omega = 0$ gives the intensity of turbulence

$$W(0) = (3\bar{n}\,\sigma_v^2\,\xi_{ls}^2)/\pi V \quad (12)$$

The units for $W(0)$ in Eq. (12) are (ft.^{2}/sec.^{2})/(rad./ft.).

In Eq. (11), where $l_{ms} \to 0$ for turbulence with small eddies, it is readily seen that this equation is, except for a constant, the approximation for the Kármán-Howarth[10] power spectrum for isentropic turbulence of fluid-velocity fluctuations normal to the direction of mean flow. The spectrum is written

$$\phi(\omega) = \frac{\phi(0)\,[1 + (3\omega^2L^2/V^2)]}{V[1 + (\omega^2L^2/V^2)]^2} \quad (13)$$

This equation is usually used to represent the power spectra of gusts, sometimes putting

$$\phi(0) = 780, \quad L = 300$$

Sometimes other values are used for $\phi(0)$ and L. Regardless of the selection of these parameters, Eq. (13) does not lead to a prediction of outputs. The moments of the output spectra are divergent.

Momentarily turning to $p(n)$: the probability-density distribution for n closes on $n = 0$. Substituting n for l in Eq. (7) and putting $l_m = 0$, gives the distribution for $p(n)$. Now let ξ_n denote the mode of $p(n)$. Then $\bar{n}$ is $2\xi_n$. With this substitution for $\bar{n}$ in Eq. (10), the power spectra of gusts are given in terms of the moments and modes of $p(v)$, $p(l)$, and $p(n)$; l_{ms}, and V. When the variable of transformation is ω/V, then speed is out.

Sample Problem

An airplane in flight through random gusts for certain wanted outputs is representable as a linear system. The gusts subject the airplane to random lifts and moments. If the wanted output is c.g. incremental load factor, then the airplane is adequately represented by the linear, rigid-body, longitudinal equations of motion. The typical output spectrum of c.g. incremental load factor in gusts is shown in Fig. 4. The spectrum is concentrated about the short-period frequency, showing that the motion is rigid body.

In this section, a sample problem is worked demonstrating the use of Eq. (10). Expected c.g. incremental load factors are predicted for a swept-wing fighter in flight through low-level gusts. The airplane flight condition is 14,000 lbs. gross weight, 16,500 slugs-ft.^{2} pitch inertia, c.g. at 25 per cent M.A.C., Mach Number 0.86, free in linear, rigid-body, longitudinal motion. Starting from the transformed equations of motion, the problem of predicting expected outputs leads naturally to Rice's equation for the number of times per second an output equals or exceeds a given value. Eq. (10) is zero for frequencies $\geq \pi V/l_{ms}$ rad., so the integrals

$$\left.\begin{aligned} \bar{X}_r^2 &= \int_0^\infty |T|^2 W(\omega)d\omega \\ I_{X_r} &= \int_0^\infty |T|^2 W(\omega)\omega^2 d\omega \end{aligned}\right\} \quad (14)$$

converge and can be used to predict expected outputs. Gust-spectrum equations $\alpha\ 1/\omega^2$ on the interval $(0, \infty)$ do not give convergent integrals and are not useful for this purpose.

Start the sample problem with the matrix equation,

$$AX = B\nu \quad (15)$$

where

$$A = \begin{bmatrix} 1 & -(Vp/g) & (1/g)p \\ 0 & (V + z_q)p & (z_{\dot{w}} - 1)p + z_w \\ 0 & (-p + M_q)p & M_{\dot{w}}p + M_w \end{bmatrix}$$

X = column (Δ_n, θ, w)

B = column $(0, Z_{\dot{w}}p + Z_w, M_{\dot{w}}p + M_w)$

Δ_n = incremental load factor

θ = pitch angle

W = plunge velocity
v = transformed gust velocity, $v(p)$
p = $i\omega$
M_q, M_w, $M_{\dot{w}}$, z_q, z_w, $z_{\dot{w}}$ = dimensional stability derivatives

The transfer function, Δ_n/V, is obtained from Eq. (15). But first it is convenient to rewrite this equation. Let X_r stand for any one of the unknowns. Let repeated indices denote summation on the repeated symbol. Now rewrite Eq. (15)

$$a_{ir}X_r = d_i v$$

Multiply by the cofactor A_{ij}

$$A_{ij}a_{ir}X_r = A_{ij}d_i v$$

But, $$A_{ij}a_{ir} = |a|\delta_{jr}$$

where $|a|$ is determinant of A, and δ_{jr} is the Kronecker delta, so that

$$|a|X_r = A_{ir}d_i v$$

and
$$T(X_r/v) = A_{ir}d_i/|a| \tag{16}$$

The symbol T is placed before X_r/V to denote that it is a transfer function for X_r and v.

Eqs. (10), (14), and (16) give information for determining the expected number of times per second that an output equals or exceeds a given value,

$$N(X_r \geq X_{ri}) = (1/2\pi)\ (I_{X_r}/\overline{X_r^2})^{1/2} \exp\{-X_{ri}^2/2\overline{X_r^2}\} \tag{17}$$

Eqs. (14) and (17) are given in reference 1.

It remains to put values in Eq. (16) for $T(X_r/v)$ and obtain a spectrum equation from Eq. (10) for flight through low-level gusts at 963 ft./sec.

The expansion of Eq. (16) for $T(\Delta_n/v)$ gives

$$T(\Delta_n/v) = \frac{-(1/g)p(p^2 - M_q p)\ (z_w + z_{\dot{w}}) - (p^2/g)\ (M_w + M_{\dot{w}}p)z_q}{(p^2 - M_q p)\ (z_w - pz_{\dot{w}} - p) + (M_{\dot{w}}p + M_w)\ (pz_q + V_p)} \tag{18}$$

Putting

$$V = 963 \text{ ft./sec.}, \quad g = 32.2 \text{ ft./sec.}^2, \quad z_q = -12.5 \text{ rad.}^{-1}, \quad z_w = -3.88 \text{ rad.}^{-1},$$

$$Z_{\dot{w}} = -0.002 \text{ rad.}^{-1}, \quad M_q = -4.87 \text{ rad.}^{-1}, \quad M_w = -0.014 \text{ rad.}^{-1}, \quad M_{\dot{w}} = -0.002 \text{ rad.}^{-1}$$

and substituting in Eq. (18) gives the result,

$$T\left(\frac{\Delta_n}{v}\right) = \frac{-0.00006p^4 - 0.120p^3 - 0.580p^2}{p^3 + 10.666p^2 + 32.203p} \tag{19}$$

Eq. (19) is the gust velocity-c.g. incremental load-factor transfer function for a typical swept-wing fighter in flight through low-level gusts at 14,000 lbs. gross weight, 16,500 slugs-ft.^{2} pitch inertia, c.g. at 25 per cent M.A.C., at Mach Number 0.86, when free in linear, rigid-body, longitudinal motion.

The next item required is a spectrum equation from Eq. (10).

In most cases flight-test data for gusts are not complete and some compromises must be made to obtain the information required in Eq. (10). The variance is readily obtained from information on the number of gusts within set intervals of gust velocity. This information is usually given. The mean number of occurences can be obtained from the number of gusts, flight hours and mean speed, provided the percentage of flight time in gusts is known. Percentages of flight distance in turbulence versus altitude are given in reference 11. This table can be used in case the percentages of flight time in gusts are not available from test records. Some duration data on gusts are given in references 12–14. For the problem at hand, an analysis of unpublished flight test data over low-level mountains puts

$$\hat{n} = 0.001 \text{ gust/ft.}, \quad \sigma_v^2 = 292 \text{ (ft./sec.)}^2$$

ξ_{ls} and l_{ms} are taken from measurements of duration of ground gusts reported in reference 12. Using the preceding values for $\hat{n}$ and σ_v^2, and

$$\xi_{ls} = 60 \text{ ft.}, \quad l_{ms} = 10 \text{ ft.}$$

from reference 12, and

$$V = 963 \text{ ft./sec.},$$

for airplane velocity, and putting these values in Eq. (10) gives

$$W(\omega) = \frac{0.296\ (2.8 + 0.00215\omega^2)}{(1 + 0.00269\omega^2)^2} \times [1 - U(\omega - 96.3\ \pi)] \tag{20}$$

Eq. (20) is a power spectrum equation for low-level gust over continuous mountains when flight velocity is 963 ft./sec.

The operations required in Eqs. (14) and (17) are conveniently handled by numerical integration, replacing the integrals in Eqs. (14) by

$$\overline{\Delta_n^2} \cong \sum_k a_k |T(\omega_k)^2| W(\omega_k)$$

$$I_{\Delta n} \cong \sum_k a_k |T(\omega_k)^2| W(\omega_k)\omega_k^2$$

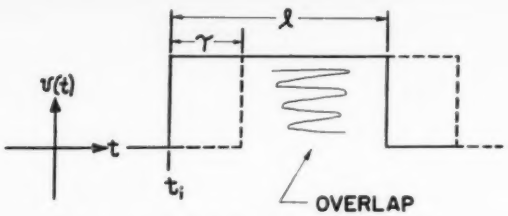

FIG. 1. Overlap of pulse $v_i(t)$ with $v_i(t + \tau)$.

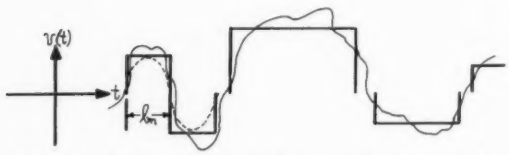

FIG. 3. Smoothing of data-reduction procedures in sample of a time trace.

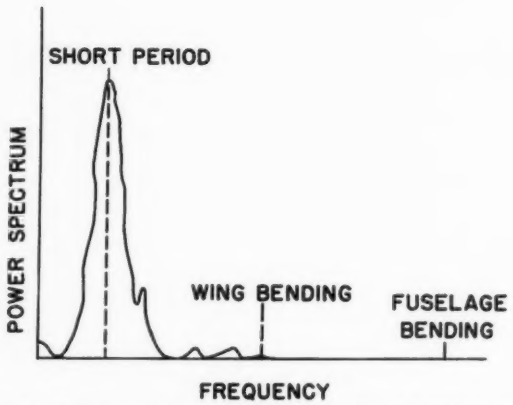

FIG. 4. Output spectrum of c.g. incremental gust load factors of an airplane in flight through random gusts.

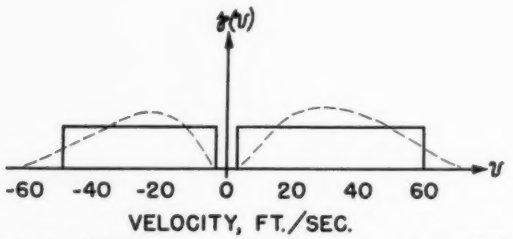

FIG. 5. $p(v)$ for extreme clear-sky gusts, $\sigma_v^2 = 1{,}000$

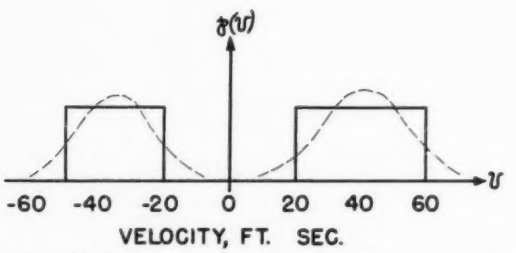

FIG. 6. $p(v)$ for extreme thunderstorm gusts, $\sigma_v^2 = 1{,}500$.

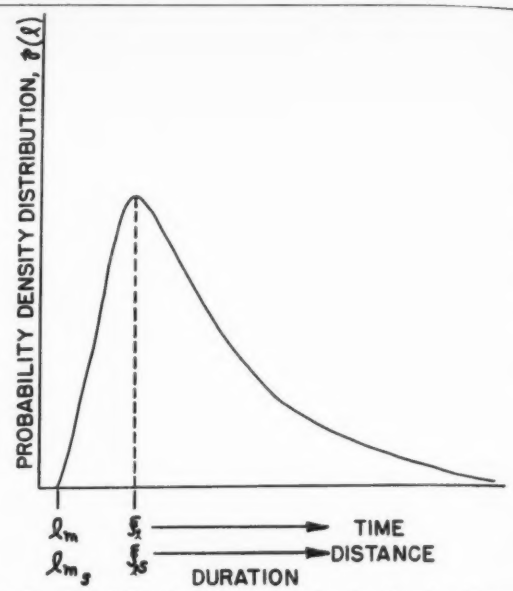

FIG. 2. Probability-density function for the duration of gusts.

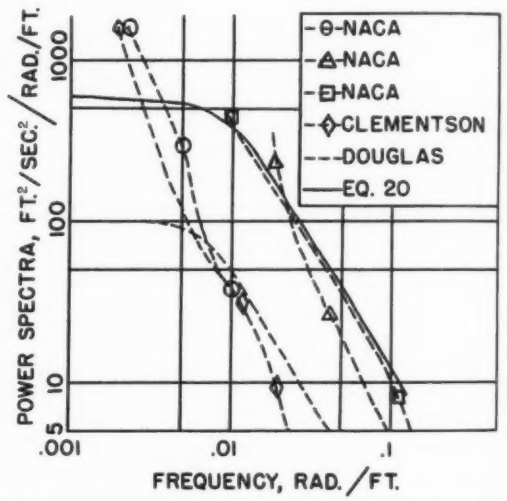

FIG. 7. Power spectra reduced from measured gust velocities and Eq. (20) for low level gusts.

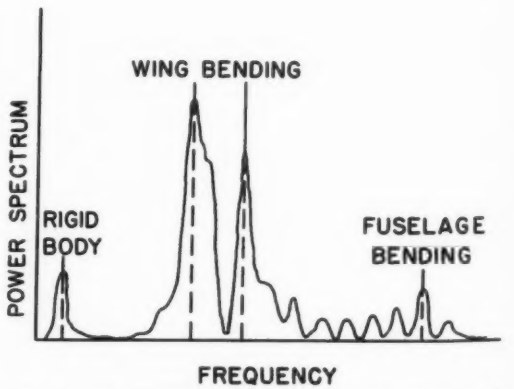

FIG. 8. Output spectrum of wing-tip normal acceleration of an airplane in flight through random gusts.

TABLE 1

Expected c.g. Incremental Gust Load Factors, V = 963 ft./sec.

Col. 1; Δn_i, g's
Col. 2; $N(\Delta n \geq \Delta n_i)$/sec.
Col. 3; no./100 hours, 40% flight time in gusts
Col. 4; no./1,000 miles, 40% flight time in gusts

1	2	3	4
0.1	3.831	551,657	20,993
0.2	3.115	448,528	17,069
0.3	2.206	317,682	12,089
0.4	1.361	196,008	7,459
0.5	0.732	105,351	4,009
0.6	0.342	49,326	1,877
0.7	0.140	20,119	765
0.8	0.050	7,148	272
0.9	0.015	2,212	84
1.0	0.004	596	22
1.1	0.001	140	5
1.2	—	28	1
1.3	—	5	—
1.4	—	0.8	—

where the a_k's are suitable integrating elements. Using parabolic row integrating elements and frequency intervals of 0.1 rad. on the frequency interval (0,6), 0.2 rad. on (6,50) and 1 rad. on (50,96) gives the numerical results

$$\overline{\Delta_n^2} = 0.07248, \quad I_{\Delta n} = 48.207$$

Substituting these values in Eq. (17) gives the results tabulated in Table 1.

The operations described above were performed on high-speed digital computing equipment.

In Table 1, column 1 is expected incremental load factor, Δ_{ni}, Column 2 is the number of times per second Δ_n is $\geq \Delta_{ni}$, Column 3 is this information for 100 hours when 40 per cent flight time is in low-level gusts, and Column 4 is this information for 1,000 miles of flight. Flight speed is 963 ft./sec.

OTHER FLIGHT CONDITIONS

Statistical parameters for other flight conditions and altitudes are listed in Table 2. These values are from an analysis of unpublished data and references cited in the preceding section.

EXTREME GUST SPECTRA

Aside from the use of test records, it is easy to construct probability-density distributions from gust velocities, select expected and extreme values for the other parameters for use in Eq. (10), and in this way obtain extreme-spectra equations for clear-sky and thunderstorm gusts.

To do this for clear-sky gusts, construct a probability-density function for a velocity distribution on interval $(-50,-2)$ and $(2,60)$, e.g., Fig. 5. Say that all velocities are equally likely to occur. Compute σ_v^2 = 1,000 ft.^{2}/sec.^{2} from $p(v)$. For low-level gusts use ξ_{ls} = 60 ft. For gusts at other altitudes use ξ_{ls} = 300 ft. Take l_{ms} = 10 ft. and $\bar{n}$ = 6/5,280, no./ft. Put Eq. (10) in terms of the transformed variable $\Omega = \omega/V$ to get rid of velocity. Then,

$$W(\Omega) = \frac{1{,}105\ (2.8 + 2{,}000\ \Omega^2)}{(1 + 2{,}500\ \Omega^2)^2} \times \left[1 - U\left(\Omega - \frac{\pi}{10}\right)\right] \quad (21)$$

$$W(\Omega) = \frac{31{,}500\ (2.965 + 81{,}200\ \Omega^2)}{(1 + 84{,}100\ \Omega^2)^2} \times \left[1 - U\left(\Omega - \frac{\pi}{10}\right)\right] \quad (22)$$

Eqs. (21) and (22) give extreme spectra for clear-sky gusts, Eq. (21) is for low-level gusts, and Eq. (22) is for other altitudes.

For thunderstorm gusts, eliminate the small velocities in the preceding distribution. Make the velocities equally likely to occur on intervals $(-50,-20)$ and $(20,60)$—e.g., Fig. 6. Compute σ_v^2 = 1,500 ft.^{2}/sec.^{2} from this distribution. Use thunderstorm[14] data for the mode of duration and put ξ_{ls} = 130 ft. Take l_{ms} = 10 ft. and $\bar{n}$ = 6.7/5,280, no./ft. Then,

$$W(\Omega) = 9{,}470\ \frac{(2.9166 + 13{,}200\ \Omega^2)}{(1 + 14{,}400\ \Omega^2)^2} \times \left[1 - U\left(\Omega - \frac{\pi}{10}\right)\right] \quad (23)$$

Spectra reduced from flight-test measurements summarized in reference 9 and spectra from Eq. (20) are shown in Fig. 7.

REMARKS

It is common practice to design for gust load factors on the basis of a simplified representation of an aircraft that is free in plunge in flight through a discrete gust. Of course, it is recognized that in the past these simplifications were necessary because fast computing machines were not available and advances in the mathematics of the analysis of random processes were not developed enough to use. But these conditions are not present now since fast computing machines are available and adequate methods of analysis of random

TABLE 2

List of Statistical Parameters*

Col. 1; Interval of altitude, multiply by 1,000
Col. 2; $\bar{n}$, no./5,280 ft.
Col. 3; ξ_{ls}, mode of duration, ft.
Col. 4; σ_v^2, variance of gust velocity, ft.^{2}/sec.^{2}

1†	2	3	4
(a) Clear-sky[12, 13]			
Ground	5.3	60	292
0–10	3.6	300	250
10–20	3.4	300	197
20–30	3.2	300	178
30–40	2.5	300	157
40–50	1.4	300	113
(b) Thunderstorm[14]			
0–20	6.7	130	324

* $\bar{n}$ and σ_v^2 for clear-sky gusts from analysis of unpublished data; ξ_{ls} = 300, from reference 12, assuming thickness and width of turbulence areas distributed the same; ξ_{ls} = 60, from reference 13. Use l_{ms} = 10 ft. for both clear-sky and thunderstorm gusts.
† In 1,000-ft. intervals.

processes are known for a realistic analysis for the gust problem. Therefore it is no longer necessary to stick to the previous simplifications. As a matter of fact, the transition stage is already here since enlightened design decisions can be made on the basis of information from both methods of analysis.

However use of the random-gust method of analysis for design purposes is limited because of the lack of critical design spectra. These criteria need to be established. Also it is necessary to set requirements on system representation. System representation requires the inclusion of airframe modes of vibration. This need is demonstrated in Fig. 8, a finite output spectrum of wing-tip normal accelerations in flight through gusts that caused a maximum c.g. incremental load factor of 0.75*g*. Airframe-coupled modes through fuselage first-bending are excited.

References

[1] Rice, S. O., *Mathematical Analysis of Random Noise*, Bell System Technical Journal, Vol. 23, 1944, Vol. 24, 1945.

[2] Lawson, J. L., Uhlenbeck, G. E., *Threshold Signals*, Massachusetts Institute of Technology, Radiation Laboratory Series, Vol. 24, McGraw-Hill Book Company, Inc., New York, 1950.

[3] James, H. M., Nichols, N. B., and Phillips, R. S., *Theory of Servo-Mechanisms*, Massachusetts Institute of Technology, Radiation Laboratory Series, Vol. 25, McGraw-Hill Book Company, Inc., New York, 1947.

[4] Wiener, N., *Extrapolation and Smoothing of Stationary Time Series*, John Wiley & Sons, New York, 1950.

[5] Liepmann, H. W., *On the Application of Statistical Concepts to the Buffeting Problem*, Journal of the Aeronautical Sciences, Vol. 19, No. 12, pp. 793–800, 822, December, 1952.

[6] Liepmann, H. W., *Extension of the Statistical Approach to the Buffeting and Gust Response of Wings of Finite Span*, Journal of the Aeronautical Sciences, Vol. 22, No. 3, pp. 197–200, March, 1955.

[7] Miles, J. W., *An Approach to the Buffeting of Aircraft Structures by Jets*, Journal of the Aeronautical Sciences, Vol. 21, No. 11, pp. 753–762, November, 1954.

[8] Luskin, Harold, and Lapin, Ellis, *An Analytical Approach to the Fuel Sloshing and Buffeting Problems of Aircraft*, Journal of the Aeronautical Sciences, Vol. 19, No. 4, pp. 217–228, April, 1952.

[9] Press, Harry, and Houbolt, John C., *Some Applications of Generalized Harmonic Analysis to Gust Loads on Airplanes*, Journal of the Aeronautical Sciences, Vol. 22, No. 1, pp. 17–26, January, 1955.

[10] von Kármán, T., and Howarth, L., *On the Statistical Theory of Isotropic Turbulence*, Proceedings of the Royal Society, Series A, Vol. 164, pp. 192–201, 1938.

[11] Copp, M. R., and Coleman, T. L., *Influence of Flight Plan on Load Histories and Riding Comfort of Transport Airlines*, Langley Aeronautical Laboratory, NACA Conference on Some Problems of Aircraft Operations, Lewis Flight Propulsion Laboratory, pp. 8–8.10, 1954.

[12] Tolefson, H. B., and Press, H., *A Review of Flight Data on Atmospheric Turbulence*, Langley Aeronautical Laboratory, NACA Conference on Some Problems of Aircraft Operations, Lewis Flight Propulsion Laboratory, pp. 7–7.9, 1954.

[13] Tolefson, H. B., Pratt, K. G., and Thompson, J. K., *An Experimental Study of the Relation between Airplane and Wind-Vane Measurements of Atmospheric Turbulence*, Langley Aeronautical Laboratory, NACA RM L52L29b, 1953.

[14] U.S. Department of Commerce, *The Thunderstorm*, Report of the Florida and Ohio Thunderstorm Project, 1946

Faculty of Science of the University of Paris

Symposium on Rarefied Gas Dynamics and Aerothermodynamics

Centre Universitaire Méditerranéen, Nice, France, July 2–5, 1958

This Symposium will be mainly concerned with the present position in regard to research being carried out on Rarefied Gas Dynamics and Aerothermodynamics. It will include theoretical and experimental studies on (1) aerodynamic and thermodynamic phenomena in highly rarefied atmospheres; (2) fundamental physical values that occurred in the preceding investigations—that is, on the accommodation coefficient and exchange momentum coefficients; and (3) apparatus and methods of measurement that relate to the field already covered in previous investigations.

Participants should submit a title and brief outline of the proposed paper as soon as possible to the Secretary: *Dr. F. M. Devienne, Laboratoire Méditerranéen de Recherches Thermodynamiques, 2 Avenue Villebois Mareuil, Nice, France.*

Members Please Note:

Have you returned your Roster Card?

(See page 294 of this issue.)

Oscillating Shock Boundary-Layer Interaction†

LEON TRILLING*

Massachusetts Institute of Technology

Summary

A simple model of the interaction of an oscillating shock wave with a laminar boundary layer is proposed. It involves a small perturbation of the steady interaction pattern found by Chapman, Larsen, and Kuehn[1] and Hakkinen, Greber, Trilling, and Abarbanel.[2] It is found that for any local Mach Number above 1.5 and for any Reynolds Number there is a combination of frequency and shock strength for which shock oscillations are neutrally stable. In particular, normal shocks reach the stability threshold when the local upstream Mach Number is between 1.57 and 1.65, depending on the Reynolds Number. A viscous interaction mechanism of this type may play a role in exciting transonic buffeting and buzz.

Symbols

c_f = skin-friction coefficient
Δc_f = change in skin-friction coefficient from flat plate value
c_p = pressure coefficient
c_{ppl} = pressure-coefficient rise from undisturbed to plateau value
Δc_p = change in pressure coefficient from flat plate value
Δc_{psh} = pressure-coefficient rise across shock
h = normal distance from solid surface to inner edge of separated boundary layer
h_0 = maximum mean height of separation region
k = reduced frequency based on free-stream velocity and distance from origin of boundary layer to shock position
K = reduced frequency based on backflow velocity and length of separated region
K_i = eigenvalues of reduced frequency K
l = length of separated region
L = distance from origin of boundary layer to mean shock position
M = mean flow Mach Number
n = exponent of the viscosity-temperature relation
r = recovery factor
R = Reynolds Number based on free-stream velocity and distance from boundary-layer origin to shock position
s = ratio of free-stream density to gas density at the wall
t = time variable
T = local temperature
T_0 = reference temperature
u = velocity (variable)
U_∞ = free-stream velocity
$\bar{u}$ = average backflow velocity in the separated region
x = length coordinate measured along solid surface
X = position of moving shock measured with respect to its mean position
α = inclination of incident shock
β = Mach parameter $\beta = (M^2 - 1)^{1/2}$
γ = ratio of specific heats
δ = boundary-layer displacement thickness
ϵ = increase in boundary-layer thickness due to pressure rise
θ = angle between separated boundary layer and solid surface
λ = ratio of backflow velocity in separated region to free-stream velocity
μ = viscosity of fluid
μ_w = viscosity at the wall
μ_0 = viscosity at a reference temperature
ρ = gas density
ρ_w = gas density at the wall
ω = frequency of shock oscillation

Received July 23, 1957.

† The research presented in this paper was supported by the U.S. Air Force under Contract No. 33(616) 3064.

* Assistant Professor of Aeronautical Engineering.

Introduction

It is well known that most shock waves observed in wind tunnels and in flight are not steady, but oscillate slightly about a mean position. In the case of oblique waves whose position is anchored by the flow geometry (angle, generating wedge, etc.) these oscillations remain of small amplitude, but the normal shock waves which occur on transonic wings and control surfaces are observed to oscillate with large amplitude and their motion causes severe buffeting and control problems in transonic flight. The mechanism by which these shock oscillations are set off is not yet understood; it may involve the effect of pressure disturbances traveling upstream from a trailing edge or other flow irregularities. In the present paper, it is shown that the interaction of a shock with a laminar boundary layer is also capable of originating self-supported (eigenvalue) oscillations and may therefore contribute to the initiation of transonic buffeting and buzz.

Discussion

The mechanism of the interaction of a laminar boundary layer with a shock wave of finite strength has been described recently by Chapman, Larsen, and Kuehn[1] and by Hakkinen, Greber, Trilling, and Abarbanel.[2] It operates essentially as follows (see Fig. 1). If the shock is strong enough to separate the boundary layer, the high pressure downstream of the shock pushes some fluid forward under the separated boundary layer which is lifted to form a free jet, but preserves its inner structure almost without change. If the separation point is situated several boundary-layer thicknesses ahead of the shock impact point, it is found that the separation phenomenon is essentially independent of the shock structure, and is self-induced and self-similar.

In fact, the separation conditions are obtained by stating that the pressure rise associated with separation is proportional to the rate of change of displacement thickness

$$\Delta c_p = (2/\beta)\,(d\epsilon/dx) \qquad (1)$$

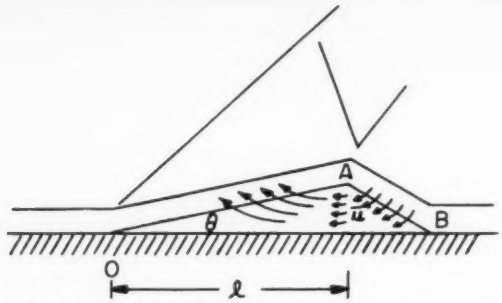

FIG. 1. Sketch of shock laminar boundary-layer interaction.

Furthermore, if the boundary layer thickens by backflow of low momentum fluid near the wall, the momentum thickness does not change appreciably so that the momentum balance relation becomes

$$-\Delta c_f = \Delta\epsilon(dc_p/dx) \tag{2}$$

where Δc_f is the difference between the skin-friction coefficient at the wall and at the lower edge of the lifted boundary layer.

Elimination of ϵ from Eqs. (1) and (2) yields the following result for the pressure rise associated with self-induced boundary-layer separation:

$$\Delta c_p = \sqrt{2\Delta c_f/\beta} \tag{3}$$

This result is derived and discussed in detail in reference 1, pp. 35–37 and compared to measurements in Fig. 34 of the same reference. The pressure rise up to separation involves a shear change $\Delta c_f = c_f$ where c_f is the boundary-layer skin-friction coefficient observed in the absence of the shock. After separation the pressure continues to rise as the backflow builds up to a limiting intensity, and the skin friction reaches a value approximately equal to $-c_f$; then the pressure ceases to rise and reaches a plateau, and the separated boundary layer forms a straight jet inclined to the stream by an angle θ, under which flows a uniform backflow of velocity $\bar{u}$.

The height of the separated region depends on the mass of fluid forced into the separated backflow region by the overpressure due to the shock. Integrating the momentum equation from A to B (see Fig. 1) one finds

$$\int_A^B [\rho u u_x + \rho v u_y + p_x]dx = \int_A^B (\mu u_y)_y dx$$

But along AB, u vanishes and experiments[2] indicate that $(\mu u_y)_y$ is small. Therefore,

$$(u_y)_{\text{ave.}} \int_A^B (-\rho v)dx = [(c_f)_{\text{ave.}}/\mu_w]\,(1/2)\rho_\infty U_\infty{}^2 \times \rho_w \bar{u}\bar{h}_0 = (1/2)\rho_\infty U_\infty{}^2 \Delta c_{p_{sh}}$$

or

$$\rho_w(\bar{u}l\theta/\mu_w) = \Delta c_{p_{sh}}/(c_f)_{\text{ave.}}$$

In the separated region, momentum is destroyed by the action of viscous forces alone, at the rate $\rho_w\bar{u}^2 dh/dx = \rho_w\bar{u}^2\theta$ per unit length, so that

$$\rho_w\bar{u}^2\theta = \rho_\infty U_\infty{}^2 c_f$$

The parameters of the separated flow region are, therefore,

$$c_{p_{pl}} = 2\sqrt{c_f/\beta}, \quad \bar{u}/U_\infty = -\sqrt{s}(c_f/\beta)^{1/4}, \quad \theta = \sqrt{\beta c_f} \tag{4}$$

$$\rho_w(\bar{u}l/\theta/\mu_w) = \Delta c_{p_{sh}}/c_f \tag{5}$$

where $\Delta c_{p_{sh}}$ is the pressure rise due to the shock, and equals the shock strength less the pressure rises needed to separate and reattach the boundary layer. Some manipulation and the introduction of the law which relates c_f to the distance L from shock to leading edge then gives the approximate formula

$$l/L = 2(c_f/\beta)^{1/4}s^{n+(1/2)}\Delta c_{p_{sh}} \tag{6}$$

where n is the exponent of the viscosity-temperature relation $\mu/\mu_\infty = (T/T_\infty)^n$.

Eqs. (4)–(6)* describe the steady shock boundary-layer interaction mechanism and are described in detail and compared to measurements in reference 2. In the following pages, an attempt is made to examine the flow pattern which results from small harmonic oscillations of the shock wave, both in strength and position.

Changes in the position of the shock induce changes in the position of the separation point and therefore in c_f, $c_{p_{pl}}$, $\bar{u}$, and l/L. Changes in the shock strength induce changes in mass flow and, therefore, essentially in l/L and θ. Both of these modify the shape of the separated boundary layer which acts as an almost impermeable perfectly flexible membrane and separates a region of slow viscous backflow near the wall from an outer region of supersonic potential flow. Any distortion of this membrane induces pressure disturbances in the potential flow which affect the motion and strength of the shock. This model suggests the possibility that under some conditions the original shock perturbations and the shock perturbations induced by the wiggling of the separated boundary layer so interact that a neutrally stable eigenvalue problem results.

A simplified model of the oscillating perturbation is now constructed. The principal feature of the disturbed flow is the distortion of the separated boundary layer under the action of variable backflow mass input. It is assumed that backflow mass fluctuations travel upstream at the mean backflow velocity without distortion so that the height of the separated boundary layer above solid wall at any point and at any time is given by an equation of the form

$$h(x,t) = \theta(\bar{x}/l) + h_0 e^{i\omega[t+\bar{x}/(|\bar{u}|)]} = \theta x + h_0 e^{iK(t+x)}; \quad K = \omega l/|\bar{u}| \tag{7}$$

where x is the distance from the mean position of the separation point (made dimensionless by division

* The numerical values of the constants in Eqs. (4)–(6) and the form of Eq. (6) are slightly different from those of reference 2, mainly to simplify the subsequent analysis at little cost in accuracy.

through l) and K is the reduced frequency based on the backflow velocity. Note that the reduced frequency based on the overall parameters L, U_∞ is obtained from Eqs. (4)–(6) as

$$k = \omega L/U_\infty = K/2s^n\Delta c_{p_{sh}} \tag{8}$$

When the boundary of the potential flow oscillates in the manner suggested by Eqs. (7), it creates an oscillating pressure field in the outer potential stream given by (see reference 3, p. 357):

$$c_p(x,t) = (2iKh_0/\beta)\,(1+\lambda)e^{iK(t+x)} \times \{e^{-[i\lambda M^2Kx/(M^2-1)]}\,J_0[\lambda KMx/(M^2-1)] + i(1+\lambda)K\int_0^x e^{-i[1+[\lambda M^2/(M^2-1)]]K\xi} \times J_0[\lambda KM\xi/(M^2-1)]\,d\xi\} \tag{9}$$

where $\lambda = |\bar{u}|/U_\infty$ so that λK is the reduced frequency based on free-stream velocity U_∞ and length of separated flow l.

The motion of the shock is given by Xe^{iKt} and the motion of the separation point is then the sum of the shock travel and the change in length of the separated region due to deformation of the separated boundary layer, $[-(h_0/\theta)e^{iKt}]$. If the boundary layer reacts instantaneously to a change in conditions (and this is a reasonable assumption since its characteristic time is δ/U_∞ as compared to $l/\bar{u}$ for the separated flow, and l is 80 to 150 boundary-layer thicknesses while $\bar{u}$ is 1/5 to 1/3 of U_∞), then the pressure perturbation at the origin is obtained by perturbing Eq. (4) as follows (from now on the multiplier e^{iKt} will be dropped from all perturbation terms):

$$c_{p_0}/c_{p_{pl}} = (1/2)\,(\Delta c_f/c_f) = -(\Delta x_{\text{sep.}}/4L) = -[(X - h_0/\theta)/4L] \tag{10a}$$

or, solving for X and substituting Eqs. (4), (6), and (9) to rewrite c_{p_0} and $c_{p_{pl}}$,

$$\theta X/h_0 = 1 - [2iK(1+\lambda)/\lambda s^n\Delta c_{p_{sh}}] \tag{10b}$$

The backflow velocity perturbation at $x = 0$ is also obtained from a perturbation of Eq. (4) as follows:

$$u(0)/\bar{u}_\infty = (1/2)\,(c_{p_0}/c_{p_{pl}}) \tag{11}$$

If the backflow velocity perturbation is transported with the particle velocity, then from Eq. (11) it follows that

$$\theta u/h_0\bar{u} = [iK(1+\lambda)/2]\,e^{iKx} \tag{12}$$

It remains to discuss the conditions at the shock ($x = 1$). If the shock motion is specified by a physical mechanism such as a moving shock generator, then X is specified and the problem is determined. However, a more interesting problem consists in requiring merely that the Rankine Hugoniot conditions be satisfied across the shock, and that the rate of backflow be given by a perturbation of Eq. (5)

$$(u/\bar{u}) + (h/\theta) = [c_p'(1+)/\Delta c_{p_{sh}}] - (c_f'/c_f) \tag{13}$$

where $c_p'(1+)$ denotes the pressure perturbation immediately behind the shock and c_f' the perturbation in mean skin friction over the boundary layer between shock and reattachment. The pressure behind the shock fluctuates for two reasons—the pressure level ahead of it fluctuates according to Eq. (9) and the incoming Mach Number fluctuates since the shock moves at a velocity $\dot{X} = iKXe^{iKt}$.

Thus one has, for the pressure perturbation immediately behind the shock,

$$c_p'(1+) = -c_p'(1-) - (\dot{X}/u_\infty)\,(d\Delta c_{p_{sh}}/dM) \tag{14}$$

where

$$c_p'(1-) = [2iKh_0(1+\lambda)/\beta]e^{iK}\{e^{i\lambda M^2K/(M^2-1)} \times J_0[\lambda MK/(M^2-1)] + i(1+\lambda)K \times \int_0^1 e^{-i[1+[\lambda M^2/(M^2-1)]]K\xi}\,J_0[\lambda KM\xi/(M^2-1)]\,d\xi\} \tag{15a}$$

$$(\dot{X}/U_\infty)\,(d\Delta c_{p_{sh}}/dM) = i\lambda KX(d/dM)\{[4/(\gamma+1)] \times [\cos^2\alpha - (1/M^2)]\} = [8i\lambda KX/(\gamma+1)M^3] \tag{15b}$$

The skin-friction disturbance is due to the fact that the region behind the shock moves with the shock motion and the mean c_f changes. Since the average c_f fluctuation is needed, it is expected that it will have a time lag with respect to X. The details of the flow structure behind the shock have not yet been determined so that the time lag cannot be estimated very accurately; it is of order e^{iK} and has so been assumed in the analysis. Thus,

$$c_f'/c_f = -(X/2L)e^{iK} \tag{16}$$

Substitution of Eqs. (7), (10b), (12), (14), (15a), (15b), and (16) into boundary condition (13) gives a relation which the flow parameters M, $\Delta c_{p_{sh}}$, K, λ must satisfy if there are to be neutral self-sustained oscillations:

$$\{(1-\lambda s^n\Delta c_{p_{sh}}) + [5iK(1+\lambda)/2]\}e^{iK} = [8K/M^3(\gamma+1)\Delta c_{p_{sh}}]\{[-2K(1+\lambda) \div s^n\Delta c_{p_{sh}}] - i\lambda\} - [2iK\lambda^2(1+\lambda)/s\Delta c_{p_{sh}}] \{J_0[\lambda MK/(M^2-1)] \times e^{iK[1-[\lambda M^2/(M^2-1)]]} + iK(1+\lambda)e^{iK}(I_c - iI_s)\} \tag{17}$$

where

$$I_c - iI_s = \int_0^1 e^{-i[1+[\lambda M^2/(M^2-1)]]K\xi} \times J_0[\lambda KM\xi/(M^2-1)]\,d\xi \tag{18}$$

Eq. (17) defines a complex eigenvalue problem for the frequency K of the oscillation. When a given flow is defined by its Mach Number and Reynolds Number, the two equations obtained by equating the real and imaginary parts of Eq. (17) to zero give a series of characteristic frequencies and a critical shock strength for each frequency.

Note that the Reynolds Number appears in the problem only through the parameter λ which is related to R by

$$\lambda = \bar{u}/U_\infty = \sqrt{s}(c_f/\beta)^{1/4} = 0.905 \times \left(\left\{1 + [(\gamma - 1)/2]rM^2\right\}^{1/2}/[(M^2 - 1)R_e]^{1/8}\right) \quad (19)$$

The Reynolds Number dependence is therefore weak; in fact, the parameter λ goes from zero to 0.3 when R goes from infinity to 100,000 at $M = 1.5$. The Mach Number ahead of the shock is seldom below 1.5 and R is in most cases appreciably above 10^5. The significant range of the parameter λ is therefore between 0 and 0.3, and in the approximate solution of Eq. (17) several terms are expanded in powers of λ and only three terms are retained.

In particular, the integrals I_s, I_c may be evaluated as follows:

$$\left.\begin{aligned} I_c &= [1/K(1 + \lambda)] \sin K + 0(\lambda^2); \\ I_s &= [1/K(1 + \lambda)] (1 - \cos K) + 0(\lambda^2) \end{aligned}\right\} \quad (20)$$

Separation of real and imaginary parts in Eq. (17) then gives

$$\cos K(1 - \lambda s^n \Delta c_{p_{sh}}) - \sin K\left\{(5/2)K(1 + \lambda) + [4K\lambda^2(1 + \lambda)/s\Delta c_{p_{sh}}]\right\} = -[16K^2 \times (1 + \lambda)/(\gamma + 1)M^3 s^n \Delta c_{p_{sh}}{}^2] + \ldots \quad (21a)$$

$$\sin K(1 - \lambda s^n \Delta c_{p_{sh}}) + \cos K\left\{(5/2)K(1 + \lambda) + [4K\lambda^2(1 + \lambda)/s\Delta c_{p_{sh}}]\right\} = (2K\lambda/\Delta c_{p_{sh}}) \times \left\{[2\lambda(1 + \lambda)/s] - [8/(\gamma + 1)M^3]\right\} + \ldots \quad (21b)$$

Elimination of the trigonometric functions from Eqs. (21a) and (21b) then gives the following algebraic relation for $\Delta c_{p_{sh}}(\lambda, K, M)$:

$$[16K^2(1 + \lambda)/(\gamma + 1)M^3 s^n \Delta c_{p_{sh}}{}^2]^2 + (4K^2\lambda^2/\Delta c_{p_{sh}}{}^2)\left\{[2\lambda(1 + \lambda)/s] - [8/(\gamma + 1)M^3]\right\}^2 = (1 - \lambda s^n \Delta c_{p_{sh}})^2 + \left\{(5K/2)(1 + \lambda) + [4K\lambda^2(1 + \lambda)/s\Delta c_{p_{sh}}]\right\}^2 \quad (22)$$

In the special case when $\lambda \to 0$, $R \to \infty$ the solution of Eq. (22) is found as

$$\Delta c_{p_{sh}} = \sqrt{32K/5(\gamma + 1)M^3 s^n}\,[1 + 0(1/12K^2)] \quad (23)$$

and the characteristic frequency K satisfies the equation

$$\left.\begin{aligned} \tan K = -(5/2)K \qquad K_1 &= 1.79 \qquad K_3 = 7.88 \\ K_2 &= 4.80 \qquad \text{etc.} \ldots \end{aligned}\right\} \quad (24)$$

In all cases, $\left\{[(5/2)K]^2 + 1\right\}^{1/2}$ may reasonably be replaced by $5/2\,K$ and in fact, Eq. (23) gives the pressure rise up to terms in λ^2 with reasonable accuracy. The frequency for finite values of λ is given by

$$\tan K = -(5/2)K[1 + \lambda(1 - 3\sqrt{1.2s^n/M^3})] + 0(\lambda^2) \quad (25)$$

and the total pressure rise is found by adding to $\Delta c_{p_{sh}}$ the plateau pressure and reattachment pressure rise

$$\Delta c_p = \sqrt{32K/5(\gamma + 1)M^3 s^n} + [32\lambda/25(\gamma + 1)M^3] + (3\lambda^2/s) + \ldots \quad (26)$$

Eqs. (25) and (26) give the shock strengths and frequencies at which neutral self-excited oscillations are possible. The critical frequency is seen to be rather insensitive to either Mach Number or Reynolds Number changes over a wide range of values of these parameters. The critical shock strength is plotted as a function of Mach Number in Fig. 2 for several values of the Reynolds Number parameter λ.

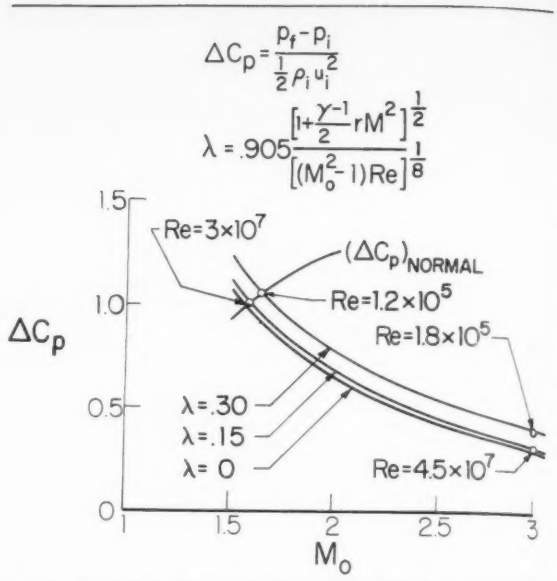

FIG. 2. Intensity of the neutrally stable oscillating shock wave as a function of upstream Mach Number.

The curves $\Delta c_{p_{cr}}(M)$ intersect the $\Delta c_{p_{\text{norm.}}}(M)$ curve—the curve which gives the pressure coefficient jump across a normal shock $\Delta c_{p_{\text{norm.}}} = [4/(\gamma + 1)]\,[1 - (1/M^2)]$—in the neighborhood of $M = 1.6$. This means that at Mach Numbers below 1.6 the oscillation is always stable; normal shocks are unstable near $M = 1.57$ ($\lambda = 0$) to 1.65 ($\lambda = 0.3$, $R \sim 1.2 \times 10^5$). At higher Mach Numbers the critical shock is much weaker than a normal shock. For example at $M = 2$, the critical shock strength corresponds to a flow deflection of 6° and at $M = 3$ to a flow deflection of 4°.

Conclusion

It has been shown that the interaction of an oscillating shock with a laminar boundary layer gives rise to an eigenvalue problem and that for certain values of shock strength and frequency, self-supported oscillations of the flow pattern occur. This mechanism or an analogous mechanism involving a turbulent boundary layer may contribute to the initiation of transonic buzz and buffeting.

References

[1] Chapman, D. R., Larson, H. K., and Kuehn, D. M., *Investigation of Separated Flows in Supersonic and Subsonic Streams with Emphasis on the Effect of Transition*, NACA TN 3869, 1957.

[2] Hakkinen, R. J., Greber, I., Trilling L., and Abarbanel, S. S., *The Interaction of an Oblique Shock Wave with a Laminar Boundary Layer*, MIT, FDRG Report #57-1, May, 1957. To be published as an NACA Technical Note.

[3] Bisplinghoff, R. L., Ashley, H., and Halfman, R. L., *Aeroelasticity*, p. 357; Addison-Wesley Publishing Co., Cambridge, Mass., 1955.

Transformation of the Compressible Turbulent Boundary Layer†

ARTUR MAGER*

Marquardt Aircraft Company

Summary

The transformation of the compressible turbulent boundary-layer equations to their incompressible equivalent is demonstrated analytically. The transformation is essentially the same as that for the laminar layer, first given by Stewartson, except that the explicit relation between the viscosity and temperature is not required. A key point in the analysis is the modification of the stream function to include a mean of the fluctuating components and the postulate that the apparent turbulent shear, associated with an elemental mass, remains invariant in the transformation.

The values of the incompressible friction coefficients and of pressure rise causing separation thus transformed show good agreement with the experimentally measured and independently reported results. An application of the transformation to the self-preserving boundary layers and to the computations of general boundary-layer flow is shown.

Symbols

a	= speed of sound
c_p	= specific heat
c_f	= friction coefficient
F, G	= functions of x
f	= Maskell's functions of Γ^* and H^*
H	= form parameter ($= \Delta/\theta$)
h	= mean total enthalpy
i	= modified total enthalpy
$k, k_1, k_2, \ldots$	= constants
L	= characteristic length
M	= Mach Number at $y = \delta$
$\mathfrak{M}$	= function of M
p	= mean pressure
q	= resultant velocity
R	= gas constant
R_x	= Reynolds Number at $y = \delta$ and based on streamwise length
t	= mean temperature
U	= u at $y = \delta$
u, v	= mean velocities
X, Y	= transformed coordinates
x, y, z	= real coordinates
α	= friction coefficients ratio
Γ	= pressure gradient parameter
γ	= specific heats ratio
Δ	= displacement thickness
δ	= boundary-layer thickness
Θ, Θ_1	= generalized momentum thicknesses
θ	= momentum thickness
κ	= thermal conductivity
μ	= absolute viscosity
ν	= kinematic viscosity
ρ	= mean density
σ	= Prandtl Number
τ	= shear
ψ	= stream function
ω	= exponent in temperature-viscosity relation

Subscripts and Superscripts

e	= at $y = \delta$
f	= final
i	= initial
in	= incompressible at same Re
0	= stagnation
or	= virtual origin
s	= separation
coordinate subscripts	designate partial differentiation
*	= transformed
′	= fluctuating value
bar	= mean value

Received October 21, 1957.

† Presented at the Meeting of Heat Transfer and Fluid Mechanics Institute, Pasadena, Calif., June 19–21, 1957.

* Technical Consultant.

Introduction

For laminar flow, the computation of the compressible boundary-layer development is greatly facilitated by the use of a transformation which establishes the corresponding incompressible flow. This transformation, first suggested by Dorodnitsyn[1] and later modified by Howarth,[2] Illingworth,[3] and Stewartson,[4] is extremely useful since it enables one to interpret all the hitherto available knowledge of the incompressible laminar boundary layer in terms of its compressible equivalent. The transformation from the compressible to the incompressible form is accomplished, in strict sense, only when the Prandtl Number is unity and there is no heat transfer between the wall and the fluid. However, even in cases where the equations do not transform exactly, the use of the transformation eliminates the varying density from most of the terms and thus simplifies considerably the solution of the problem. In this way, for example, it was possible to apply the Thwaites method[5] to the compressible laminar boundary-layer flow with heat transfer.[6]

It has been shown, independently, by Dorodnitsyn[7] and by Van Le[8] that the transformation valid in the laminar boundary layer also eliminates the varying mean density from the momentum-integral equations of the turbulent boundary layer. This, of course, is not surprising, since in the integrated form, certain terms involving the mean of the product of the fluctuating density and velocities are neglected, with the justification that, while these terms can possibly be large locally, when integrated over the whole boundary layer they will tend to cancel themselves out.[9] Consequently, the momentum-integral equations for the compressible turbulent boundary layer are identical in form to those for the laminar layer, and one may expect the same transformation to apply.

In spite of this fact, however, one may not be confident that the laminar transformation is actually valid for the turbulent flow. The main objections that can be raised are as follows: (a) the transformation converts the once-integrated form of the equations instead of the differential ones and consequently does not ensure that the effect of the terms eliminated by averaging is not lost; (b) the transformation requires a certain change in the wall shear, which in view of our limited knowledge of the turbulent shear, may or may not be correct; and (c) the transformation (at least in reference 8) requires a redefinition of the displacement thickness, which is not convenient conceptually.*

The goal of this paper is to overcome these objections so that the application of the transformation to the turbulent boundary layer can be justifiable on more solid theoretical grounds and thus more acceptable. Furthermore, a comparison between the theoretical and experimental results for the skin friction of flat plates as well as for the separation pressure ratio of the turbulent layer will be made. Finally, a conversion of the quantities essential to the computation of the general compressible turbulent boundary-layer development will be demonstrated.

Transformation of the Turbulent Boundary Layer

The equations of the steady compressible turbulent boundary layer were derived by Young.[10] This derivation requires, in addition to the conventional assumptions, that the partial derivatives with respect to x of the mean stresses due to fluctuations be neglected, as small, when compared with the corresponding derivatives with respect to y. Furthermore, a number of terms involving triple correlations, the fluctuating thermal conductivity, and the dilatation were also neglected. When the mean values are taken, the equations become

$$(\rho u)_x + (\rho v + \overline{\rho' v'})_y = 0 \tag{1}$$

$$\left.\begin{aligned} \rho u u_x + (\rho v + \overline{\rho' v'}) u_y &= -p_x + (\mu u_y - \overline{\rho u' v'})_y \\ p_y &= O(1) \end{aligned}\right\} \tag{2}$$

$$\rho u h_x + (\rho v + \overline{\rho' v'}) h_y = \left\{ \left(\frac{\kappa}{c_p}\right) [h + 0.5(\sigma - 1) q^2] - \overline{\rho v' h'} \right\}_y \tag{3}$$

In these equations the primes denote the fluctuating terms and h, the total enthalpy, includes the mean kinetic energy associated with the turbulent velocity components—e.g., $h = (c_p t + 0.5\ \overline{q^2})$, where q is the magnitude of the resultant velocity. It is quite obvious from Eq. (3) that one solution of this equation, when there is no heat transfer and when $\sigma = 1.0$, is given by $h =$ constant and $\overline{v'h'} = 0$.

The essence of the laminar boundary-layer transformation lies in the stretching of the physical coordinates into an imaginary incompressible system (without varying density) in which the properties of the fluid are evaluated at certain reference conditions. In addition, in order to ensure that the two boundary layers are really corresponding, the stream function, which is the measure of mass flow contained in the boundary layer, remains unchanged by the transformation.

In the turbulent boundary layer, however, where the stream function does not describe the boundary layer completely, because of the presence of the turbulent stress, one may expect additional requirements which will ascertain that the transformed and the original layers really do correspond. In particular, if one assumes that at any point in the flow field the turbulent shear is a property of the flow which is essentially constant over an infinitesimal mass of the fluid, then, in view of the invariance of the stream function, it seems logical to require that the total amount of shear associated with such elemental mass should also remain invariant. From a physical standpoint, this means that the mechanism of the turbulent process is unchanged by the compressibility effect; however, the fluid is allowed to expand or contract in response to the internal heating.† In addition to this specific assumption on the mode of transformation of the turbulent stress, one also should choose the reference conditions at the stagnation value so that the total enthalpy (for $\sigma = 1.0$ and adiabatic flow) is the same. This choice then ensures that the internal heating affecting the turbulent stress transformation is properly scaled. It should be noted that this is somewhat different from the laminar transformation, where the choice of the reference condition is essentially unimportant.‡ It is these

* Since the presentation of this paper and as this manuscript goes to press, author's attention has been called to three additional contributions to the problem of compressible turbulent boundary-layer transformation. One of these is a note by R. E. Meyer, *Turbulent Boundary Layers on Nozzle Liners* (Journal of the Aeronautical Sciences, Vol. 22, No. 8, pp. 572–573, August, 1955), in which the compressible flow transformation of the momentum-integral equation is postulated and then the thus computed results are shown to agree with those obtained from empirically derived formula. The other two papers are by G. W. Englert, *Estimation of Compressible Boundary Layer Growth Over Insulated Surfaces With Pressure Gradient* (NACA TN 4022, June, 1957), and by F. E. C. Culick and J. A. F. Hill, *A Turbulent Analog of the Stewartson-Illingworth Transformation* (Journal of the Aeronautical Sciences, Vol. 25, No. 4, pp. 259–262, April, 1958). In both of these papers it is pointed out, as already noted by Van Le, that the possibility of transforming the momentum-integral equation hinges on the relation between the compressible and incompressible friction laws. The authors then substitute the experimentally obtained friction laws, involving a certain reference temperature, and show that the resulting transformation is very nearly equivalent to that of Stewartson. Although such a procedure weakens some of the objections raised above, still all of these treatments do not ensure that the effect of the terms eliminated by averaging in the original momentum-integral equation is not lost.

† This meaning has been pointed out to the author by Prof. Hans W. Liepmann.

‡ This has been called to the author's attention by Prof. Nicholas Rott during discussion at the 1957 Heat Transfer and Fluid Mechanics Institute.

requirements on the turbulent stress transformation that will be used in the present paper.

First, a transformation, similar to that used for the laminar boundary layer, may be postulated:

$$\left.\begin{aligned} X &\equiv \int_0^x FG\,dx; \\ \partial/\partial x &= FG(\partial/\partial X) + Y_x(\partial/\partial Y) \\ Y &\equiv F\int_0^y (\rho/\rho_0)dy; \quad \partial/\partial y = F(\rho/\rho_0)\,(\partial/\partial Y) \end{aligned}\right\} \tag{4}$$

with the additional requirements that

$$\psi \equiv \psi^*; \quad (\rho\overline{u'v'})\rho dx\,dy\,dz \equiv (\rho_0\overline{u'v'^*})\rho_0 dX\,dY\,dz \tag{5}$$

In these equations, X, Y, and the quantities denoted by the star are understood to be in the transformed system, while the functions $F(x)$ and $G(x)$ are as yet undetermined.

The original velocities may now be expressed in terms of the stream function, so that the continuity condition (1) is identically satisfied;

$$\rho u = \rho_0\psi_y; \quad -(\rho v + \overline{\rho' v'}) = \rho_0\psi_x \tag{6}$$

and the transformed velocities should be defined in the conventional incompressible manner;

$$u^* = \psi_Y^*, \quad -v^* = \psi_X^* \tag{7}$$

In view of the condition on the stream function [Eq. (5)], Eqs. (6) and (7) furnish a relation between the velocities in the two systems and Eq. (1) transforms to its incompressible form:

$$u = Fu^*; \quad \rho v + \overline{\rho' v'} = \rho_0(FGv^* - Y_x u^*) \tag{8}$$

$$u_X^* + v_Y^* = 0 \tag{1a}$$

To proceed further, one first has to determine the explicit relation between the turbulent shears in both systems. Therefore, using Eqs. (4) and (5) one obtains the elemental area transformation

$$dX\,dY = [\partial(X, Y)/\partial(x, y)]dx\,dy = (\rho/\rho_0)F^2G\,dx\,dy$$

leading to

$$\rho\overline{u'v'} = F^2G\,\rho_0\overline{u'v'^*} \tag{9}$$

With this condition, Eq. (2) may be put, after some manipulation, into the form

$$u^*u_X^* + v^*u_Y^* = U^*\frac{dU^*}{dX}\frac{[(1/\rho) + (1/F)\,(dF/dp)u^2]}{[(1/\rho_e)(1/F)(dF/dp)U^2]} + \frac{1}{\rho_0F^2G}\left(\frac{\rho\mu}{\rho_0}F^2u_Y^* - F^2G\rho_0\overline{u'v'^*}\right)_Y \tag{10}$$

One must now so choose the functions F and G that Eq. (10) will obtain the incompressible form when $\sigma = 1.0$ and when the flow is adiabatic. Realizing that the total enthalpy is given approximately by $h \approx i = (c_pt + 0.5\,u^2)$, and that this quantity must be a constant for $\sigma = 1.0$ and adiabatic flow, one requires that F satisfy the differential equation

$$dF/F = (R/2c_p)\,(dp/p) = [(\gamma - 1)/2\gamma]\,(dp/p) \tag{11}$$

for then the first term on the right-hand side becomes $U^*(dU^*/dX)$. Incidentally, if the flow is not adiabatic then this term becomes $U^*(dU^*/dX)\,(i/i_e)$, just as in the laminar boundary layer.[6] The differential equation (11) must be solved, in view of relations (8), with the requirement that at the reference condition $F = 1.0$. This solution gives, just as in Stewartson's transformation,

$$F = (p/p_0)^{(\gamma-1)/(2\gamma)} = a_e/a_0 = (t_e/t_0)^{1/2} \tag{12}$$

The second term on the right-hand side of Eq. (10) can similarly be converted to the incompressible form when it is realized that the product of viscosity and density must behave very nearly like the pressure—that is, it may be considered independent of y. Consequently, it is permissible to set

$$G = (\rho\mu/\rho_0\mu_0) = (\rho_e\mu_e/\rho_0\mu_0) = (\mu_e/\mu_0)\,F^{2/(\gamma-1)} \tag{13}$$

without specifying the explicit dependence of viscosity on temperature. It should be noted that if the viscosity is assumed to vary directly in proportion with the temperature, then the function G is identical with that given by Stewartson,

$$(\mu/\mu_0) = k(t/t_0) \rightarrow G = k(p/p_0) \tag{13a}$$

Using Eqs. (12) and (13), one is able to convert Eq. (10) to the desired incompressible form,

$$u^*u_X^* + v^*u_Y^* = U^*(dU^*/dX) + \nu_0u_{YY}^* - (\overline{u'v'^*})_Y \tag{2a}$$

and demonstrate that the application of the thus postulated transformation to the turbulent boundary layer is indeed valid from the analytical standpoint. The slight modification of the Stewartson transformation, which was here introduced, should permit a closer description of the variation of viscosity with temperature and should, of course, be also applicable in the laminar boundary layer.

Experimental Verification

Flat Plate Skin Friction

The usefulness of the transformation in the turbulent flow may be demonstrated by deriving the appropriate formulas for the local and average skin-friction coefficients of flat plates. This derivation is especially important since the comparison of the thus obtained friction coefficients with experimentally measured values, as well as with values derived by entirely different methods, can readily be made. This comparison can thus serve as some measure of the transformation's validity.

Now in incompressible flow a modified Blasius formula for the local coefficient is known to be applicable up to $R_e = 10^7$ (see reference 11):

$$0.5\,c_f^* = 0.0296\,(R_e^*)^{-0.2} \tag{14}$$

To convert this formula to the compressible flow, one

must first find the transformations between the friction coefficients and between the Reynolds Numbers. Using Eqs. (8) and (9) one finds that

$$c_f^* = (\mu_0/\mu_e)c_f; \quad R_e^* = (\mu_e/\mu_0)^2 R_e \tag{15}$$

With these relations the Blasius formula may be written as

$$0.5\, c_f = 0.0296\, (R_e)^{-0.2}\, (\mu_e/\mu_0)^{0.6} \tag{14a}$$

The variation of viscosity with temperature can be most accurately described by the Sutherland formula. Here, however, in order to avoid analytical complications, one can take the simplified relation

$$(\mu_e/\mu_0) \doteq (t_e/t_0)^{\omega} \tag{16}$$

so that the ratio of the compressible to incompressible skin-friction coefficients, *at the same Reynolds Number*, becomes

$$(c_f/c_{f,\,in}) = (t_e/t_0)^{0.6\omega} \tag{14b}$$

This relation, with $\omega = 0.76$, is shown in Fig. 1, together with an analogous relation obtained by Eckert's "reference temperature" method[11] and a few experimental points of Coles[12] and Korkegi.[13] As may be seen from this Figure, despite the assumption of $\sigma = 1.0$, the agreement is reasonably good.

To illustrate that the good agreement is not due to the particular expression used for the incompressible coefficient [Eq. (14)], one may compute the average skin-friction coefficients by a different formula, equally acceptable. According to reference 11, the Kármán-Schoenherr formula is valid up to $R_e = 10^9$:

$$0.242\, (\bar{c}_f^*)^{-(1/2)} = \log_{10}(\bar{R}_e^* \bar{c}_f^*) \tag{17}$$

By the application of Eqs. (15), this expression may be restated for compressible flow as

$$0.242\, (\bar{c}_f)^{-(1/2)}\, (\mu_e/\mu_0)^{1/2} = \log_{10}(\bar{c}_f \bar{R}_e) - \log_{10}(\mu_0/\mu_e) \tag{17a}$$

Using Eq. (16) and setting the ratio of the compressible to incompressible skin-friction coefficients (at same $\bar{R}_e$) equal to $(1/\alpha)$, Eq. (17a) can be written in a more convenient form for computation as

$$\log_{10}(\bar{c}_{f,\,in}\, \bar{R}_e)\, [1 - \sqrt{\alpha(t_e/t_0)^{\omega}}] = \log_{10}\, [\alpha(t_0/t_e)^{\omega}] \tag{17b}$$

The solution of Eq. (17b) for $\bar{R}_e = 10^7$ and $\omega = 0.76$ is shown in Fig. 2. Also shown in this Figure are the analytical results of Van Driest,[14] obtained by the similarity mixing-length method, and the directly measured experimental data of Chapman and Kester.[15] Again, in spite of the assumed $\sigma = 1.0$, the agreement with the experiment and with the Van Driest analysis is very good.

Shock-Separated Turbulent Boundary Layer

Since the transformation represents a certain correspondence between the compressible and incompressible boundary layers, if this correspondence is real, the transformation should be able to convert not only the various analytical results, but also purely empirical relations. Indeed, an experimental verification of the so-transformed empirical laws could be considered as one of the proofs of the transformation's validity. An indication that the empirical laws transform properly has already been obtained in the previous section, where it was shown that the transformed skin-friction relations, which, after all, do involve some empiricism in their original form, agree reasonably well with experiment and with other theories. An even more spectacular illustration of the usefulness of the transformation and its validity is furnished by the estimation of the pressure rise occurring with a shock-separated turbulent boundary layer.

As is well known, the separation of the incompressible turbulent boundary layer, in the presence of very steep pressure gradients, has been observed to occur when the velocities outside the boundary layer satisfy

$$U_s^{2*} = k_1 U_i^{2*} \tag{18}$$

with $k_1 \doteq 0.55$. This relation between the velocities can also be argued on the basis of the semiempirical equation relating the shape of the velocity profile to the pressure gradient and to the shear at the wall. In compressible flow, applying Eq. (8), this purely empirical relation becomes

$$M_s^2 = k_1 M_i^2 \tag{18a}$$

and consequently one is in a position to evaluate the pressure rise connected with shock-caused separation. The details of such an analysis have been explained in reference 16; here we shall only show the final result. This is presented in Fig. 3, along with the experimentally measured separation pressure ratio for a number of shock-causing configurations plotted against the Mach number before the shock. As can be seen from this Figure, (and considering the difficulty with which the separation pressure is experimentally determined), the agreement between the transformed results and the experimental data is fair.

As is well known, the pressure at which the separation occurs is not the highest pressure measured for such an interaction. This, of course, is the reason why it is so difficult to determine the separation pressure properly. The highest pressure reached can be determined with considerably greater certainty. On the other hand, assuming that the additional pressure rise occurs due to the centrifugal effects and once more using the transformation, the ultimate pressure rise can also be found analytically and the details of such a computation are also given in reference 16. In Fig. 4 are shown the results of such computations, together with the experimental data obtained by number of investigators. As may be seen, the analytical results appear to be confirmed closely by experiment.

It is important to note that, in any boundary layer, both the shear at the wall and the pressure gradient play an important role. In a laminar layer there seems to be a certain correlation between the two, as indicated by the success of the Thwaites method. In

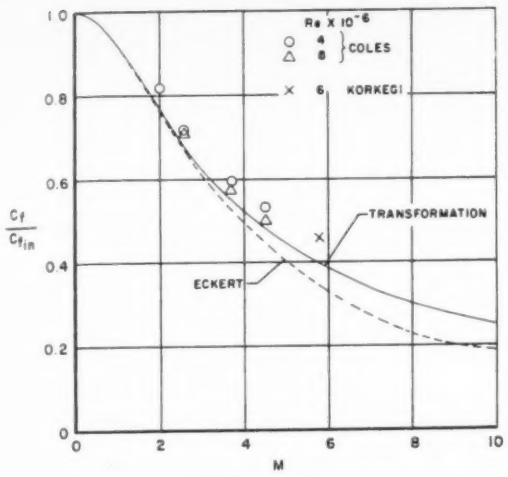

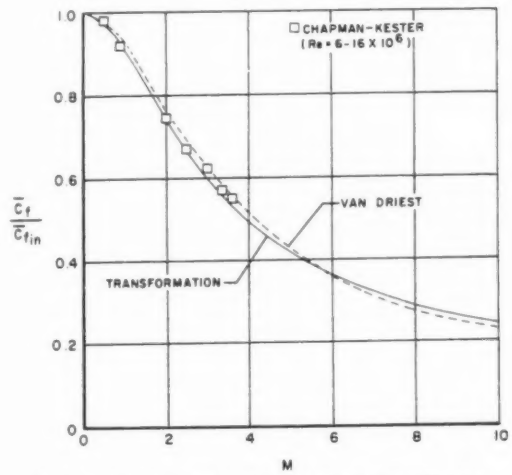

FIG. 1 (*top*). Local flat plate skin-friction coefficient.
FIG. 2 (*bottom*). Mean flat plate skin-friction coefficient, $\bar{R}_x = 10^7$.

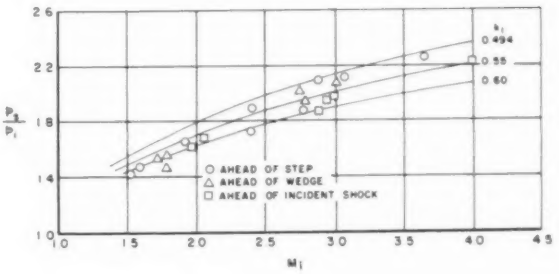

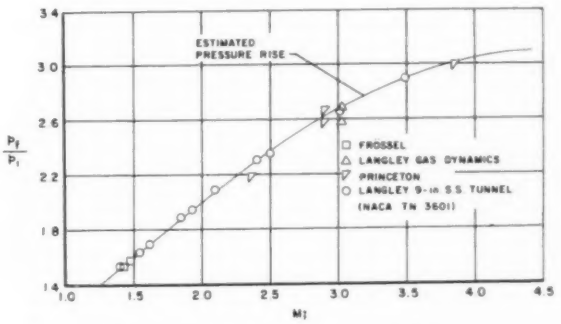

FIG. 3 (*top*). Separation pressure ratio.
FIG. 4 (*bottom*). Pressure ratio of free shock—separated turbulent boundary layer, $\gamma = 1.4$, plane shock.

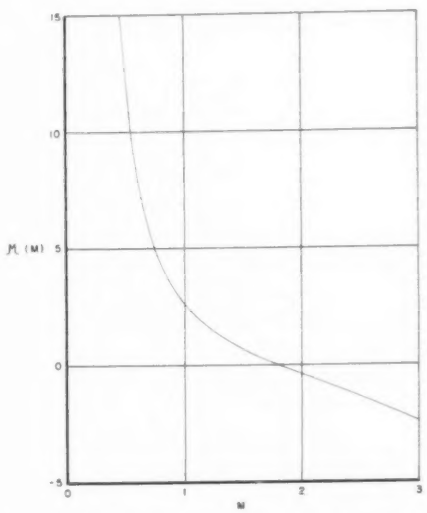

FIG. 5. $\mathfrak{M}(M)$ for $k_2 = -1/3$, $M < M_s$, $\gamma = 1.4$

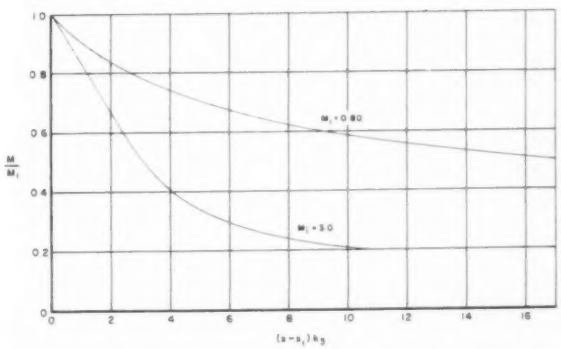

FIG. 6. Mach Number distribution for self-preserving boundary layer, $k_2 = -1/3$, $\gamma = 1.4$.

a turbulent layer, however, the pressure gradient and the shear at the wall appear to play an essentially independent role. This is indicated, for example, by the fact that in the absence of pressure gradient, the so-called universal velocity distribution is obtained only when the effect of the shear at the wall is taken into account.

Now it has been shown in the previous section that the compressible flow transformation gives correct results in the absence of the pressure gradient, while in this section, good results have been obtained for flows with strong pressure gradients but negligible wall shear. Thus, so to speak, two extremes of the turbulent boundary-layer problem have been tested. For a complete experimental verification, one should also check a case when both the wall shear and the pressure gradient play an equally important role. Unfortunately, however, the absence of experimental data for such a general case does not permit one to carry this out.†

Applications

Self-Preserving Boundary Layer

Townsend has recently shown[17] that when $(\rho_0 \overline{u'v'^*})$ is the only component of the turbulent shear, then a self-preserving (equilibrium) incompressible turbulent boundary-layer flow can occur if

$$(U^*/U_i^*) = [(X - X_{or})/(X_i - X_{or})]^{k_2} \qquad (19)$$

where subscripts i and or denote the initial point and the virtual origin of the flow, respectively, while constant k_2 signifies the appropriate pressure gradient. Of greatest interest are, of course, the cases when the pressure gradient is unfavorable—that is, when $X > X_{or}$ and $k_2 < 0$. For such cases, Townsend has shown that the smallest possible value of k_2 is $k_2 = -1/3$. Applying the transformation and assuming for simplicity a linear dependence of viscosity on the temperature, Eq. (19) can be stated as

$$\frac{M}{M_i} = \left\{\left[\int_{x_{or}}^{x}\left(1 + \frac{\gamma - 1}{2}M^2\right)^{-[(3\gamma-1)/2(\gamma-1)]} dx\right] \times \left[\int_{x_{or}}^{x_i}\left(1 + \frac{\gamma - 1}{2}M^2\right)^{-[(3\gamma-1)/2(\gamma-1)]} dx\right]^{-1}\right\}^{k_2} \qquad (19a)$$

and the required distribution of the Mach Number is given by

$$M^{1/k_2} = k_3 \int_{x_{or}}^{x}\left(1 + \frac{\gamma - 1}{2}M^2\right)^{-[(3\gamma-1)/2(\gamma-1)]} dx \qquad (19b)$$

where k_3 is a constant permitting the correct match between the pressure gradient and the boundary layer—that is, ensuring that the flow comes from the appropriate virtual origin. Eq. (19b) can be differentiated, rearranged and integrated for $\gamma = 1.4$, with the initial conditions at $x = x_i$, $M = M_i$, to give

$$\left.\begin{aligned} \mathfrak{M}(M) - \mathfrak{M}(M_i) &= k_3(x - x_i) \\ \mathfrak{M}(M) = M^{1/k_2}\{1 &+ [0.8/(1 + 2k_2)]M^2 + \\ [0.24/(1 + 4k_2)]M^4 &+ [0.032/(1 + 6k_2)]M^6 + \\ [0.0016/(1 + 8k_2)]M^8\}& \end{aligned}\right\} \qquad (20)$$

The function $\mathfrak{M}(M)$ is shown in Fig. 5, while in Fig. 6 the distribution of M/M_i vs. $(x - x_i)\,k_3$ is plotted. It may be seen that for a flow with the same virtual origin, a much steeper decrease of Mach Number is possible in supersonic flow than in subsonic flow.

General Boundary-Layer Flow

The compressible flow transformation is particularly valuable in the computation of the general boundary-layer flow. The methods for such a computation in incompressible flow are always somewhat empirical and an establishment of analogous methods for the compressible flow, in a conventional way, would require a tremendous amount of experimental information. Using the transformation, however, one can immediately reinterpret the incompressible flow methods for the compressible flow. One such method has been given by Maskell[18] and it appears to give very satisfactory results.[19] This method allows to solve for the momentum thickness directly from

$$\left.\begin{aligned} (U^{*4.2}\,\Theta^*/L) &= (U^{*4.2}\Theta^*/L)_i + \\ &\quad 0.01173\int_{X_i/L}^{X/L} U^{*4.2}\,d(X/L) \\ (\theta^*/L) &= (\Theta^*/L)^{0.8225}\,(U^*L/\nu_0)^{-0.1775} \end{aligned}\right\} \qquad (21)$$

It should be noted that since Θ^* is only an auxiliary parameter, all one has to find is the conversion from $\Theta^*(X)$ to $\Theta^*(x)$. This can be accomplished by assuming a power law for viscosity

$$(M^{4.2}\Theta^*/L) = (M^{4.2}\Theta^*/L)_i + 0.01173 \times \int_{x_i/L}^{x/L} M^{4.2}\{1 + [(\gamma - 1)/2]M^2\}^{-(k_4+\omega)}\,d(x/L) \qquad (21a)$$

with $k_4 = 0.5(\gamma + 1)/(\gamma - 1)$. Also, since it can be shown that

$$\theta = \{1 + [(\gamma - 1)/2]M^2\}^{k_4}\,\theta^* \qquad (22)$$

one has

$$\theta/L = \{1 + [(\gamma - 1)/2]M^2\}^{k_4}\,(\Theta^*/L)^{0.8225} \times (Ma_0L/\nu_0)^{-0.1775} \qquad (23)$$

In addition to the momentum thickness, one also has to compute the form factor H^*. Now the Maskell equation for this involves a number of functions, some of which are in graphical form. Therefore, instead of elaborating on the details, one can indicate the general form of the equation and give the appropriate conversions which will permit to use the graphically plotted functions of Maskell. The equation can be written

$$\left.\begin{aligned} \Theta_1^*\,(dH^*/dX) &= f(\Gamma^*, H^*) \\ \Theta_1^* &\equiv \theta^*\,(\theta^*U^*/\nu_0)^{0.268} \\ \Gamma^* &\equiv (\Theta_1^*/U^*)\,(dU^*/dX)\,(10)^{0.678H^*} \end{aligned}\right\} \qquad (24)$$

† The data quoted by Englert and by Culick and Hill give some evidence that the transformation is also valid when the wall shear and the pressure gradient are equally important.

Again, it is only necessary to convert from $H^*(X)$ to $H^*(x)$, and this can be done by writing

$$\left.\begin{aligned} dH^* &= \{1 + [(\gamma - 1)/2]M^2\}^{-(k_4+\omega)} \times \\ &\qquad (L/\Theta_1^*) f(\Gamma^*, H^*)\, d(x/L) \\ (\Theta_1^*/L) &= (\Theta^*/L)\Big(M\{1 + [(\gamma - 1)/2]M^2\}^{-k_4} \\ &\qquad \times (\theta/L)\,(a_0 L/\nu_0)\Big) \\ \Gamma^* &= \{1 + [(\gamma - 1)/2]M^2\}^{(k_4+\omega)} \times \\ &\qquad (\Theta_1^*/L)\,(1/M)\,[dM/d(x/L)]\,(10)^{0.678H^*} \end{aligned}\right\} \quad (24a)$$

Eqs. (24a) can be numerically integrated knowing $M(x)$, $\Theta^*(x)$, and $\theta(x)$. Once $H^*(x)$ is known, the displacement thickness may be found by using the expression suggested in reference 6,

$$\Delta/L = \theta/L\,\big(H^*\{1 + [(\gamma - 1)/2]M^2\} + [(\gamma - 1)/2]M^2\big) \quad (25)$$

Finally, the separation of the boundary layer is assumed to occur where the Ludwieg-Tillmann skin-friction coefficient extrapolates to zero. In Maskell's nomenclature this coefficient can be written as

$$c_f^* = (0.246/\Gamma^*)\,(\theta^*/U^*)\,(dU^*/dX) \quad (26)$$

so that in compressible flow it can be computed from

$$c_f = (0.246/\Gamma^*)\,(\theta/L)\,(1/M)\,[dM/d(x/L)] \quad (26a)$$

Using Eqs. (21a), (23), (24a), (25), (26a), and the f functions of Maskell, general boundary-layer flow can be easily computed. It should be noted that any other method can similarly be converted to the compressible flow. The Maskell method was chosen only for the purpose of illustration and because it appears to give good results in incompressible flow.

References

[1] Dorodnitsyn, A. A., *Laminar Boundary Layer in a Compressible Gas*, DAN, Vol. XXXIV, No. 8, 1942.

[2] Howarth, L., *Concerning the Effect of Compressibility on Laminar Boundary Layers and Their Separation*, Proc. Roy. Soc., (London), Ser. A, Vol. 194, No. A1036, July, 1948.

[3] Illingworth, C. R., *Steady Flow in the Laminar Boundary Layer of a Gas*, Proc. Roy. Soc. (London), Ser. A, Vol. 199, No. A1059, December, 1949.

[4] Stewartson, K., *Correlated Incompressible and Compressible Boundary Layers*, Proc. Roy. Soc. (London), Ser. A, Vol. 200, No. A1060, December, 1949.

[5] Thwaites, B., *Approximate Calculation of the Laminar Boundary Layer*, Aero. Quart., Vol. I, pp. 245–280, November, 1949.

[6] Cohen, C. B., and Reshotko, E., *The Compressible Laminar Boundary Layer With Heat Transfer and Arbitrary Pressure Gradient*, NACA TN 3326, 1955.

[7] Dorodnitsyn, A. A., *Boundary Layer in a Compressible Gas*, Prikl. Matem, i Mekh, Vol. VI, No. 6, 1942.

[8] Van Le, N., *Transformation Between Compressible and Incompressible Boundary-Layer Equations*, Journal of the Aeronautical Sciences, Vol. 20, No. 8, pp. 583–584, August, 1953.

[9] Shapiro, A. H., *The Dynamics and Thermodynamics of Compressible Fluid Flow*, Vol. II; The Ronald Press Co., New York, 1953.

[10] Howarth, L., (Ed.), *Modern Developments in Fluid Dynamics, High Speed Flow*, Vol. I, pp. 453–455; Clarendon Press, Oxford, 1953.

[11] Eckert, E. R. G., *Survey on Heat Transfer at High Speeds*, WADC Tech. Rep. 54-70, April, 1954.

[12] Coles, D., *Measurements of Turbulent Friction on a Smooth Flat Plate in Supersonic Flow*, Journal of the Aeronautical Sciences, Vol. 21, No. 7, pp. 433–438, July, 1954.

[13] Korkegi, R. H., *Transition Studies and Skin-Friction Measurements on an Insulated Flat Plate at a Mach Number of 5.8*, Journal of the Aeronautical Sciences, Vol. 23, No. 2, pp. 97–107, February, 1956.

[14] Van Driest, E. R., *The Problem of Aerodynamic Heating*, Aeronautical Engineering Review, Vol. 15, No. 10, pp. 26–41, October, 1956.

[15] Chapman, D. R., and Kester, R. H., *Measurements of Turbulent Skin Friction on Cylinders in Axial Flow at Subsonic and Supersonic Velocities*, Journal of the Aeronautical Sciences, Vol. 20, No. 7, pp. 441–448, July, 1953.

[16] Mager, A., *On the Model of the Free, Shock-Separated Turbulent Boundary Layer*, Journal of the Aeronautical Sciences, Readers' Forum, Vol. 23, No. 2, pp. 181–184, February, 1956.

[17] Townsend, A. A., *The Structure of Turbulent Shear Flow*, Cambridge University Press, Cambridge, 1956.

[18] Maskell, E. C., *Approximate Calculation of the Turbulent Boundary Layer in Two-Dimensional Incompressible Flow*, Rep. No. Aero. 2443, British RAE, November, 1951.

[19] Sandborn, V. A., *Preliminary Experimental Investigation of Low-Speed Turbulent Boundary Layers in Adverse Pressure Gradients*, NACA TN 3031, October, 1953.

Change of Address

Since the Post Office Department does not as a rule forward magazines to forwarding addresses, it is important that the Institute be notified of changes in address 30 days in advance of publishing date to ensure receipt of every issue of the JOURNAL and REVIEW.

Notices should be printed legibly and sent directly to:

Subscription Department
Institute of the Aeronautical Sciences, Inc.
2 East 64th Street, New York 21, N.Y.

Supersonic Flutter of a Cylindrical Shell—II†

JOHN W. MILES*

University of California, Los Angeles

SUMMARY

The theory of Part I (see reference 1) is applied to pressurized shells filled with either gas or liquid. The flutter speeds and negative damping ratios are calculated; the latter also are presented in graphical form. A summary of the symbols in both Parts I and II is given below.

SYMBOLS

A	= space wave amplitude, see Eq. (3.3) in reference 1
A_1	= surface wave amplitude, see Eq. (3.5) in reference 1
C	= see Eq. (7.16)
C_m	= Fig. 12
D	= bending stiffness $[Eh^3/12(1-\nu^2)$ for panel]
E	= Young's modulus
F	= see Eq. (7.14) and Fig. 9
G	= see Eq. (7.18)
G_m	= Fig. 10
K_n	= modified Bessel function of second kind (Macdonald's function)
L	= see Eq. (3.2) et seq. in reference 1
M	= free-stream Mach Number ($M = U/a$)
M_1	= see Eqs. (7.20), (7.21), and Fig. 11
N_x	= axial force per unit width of shell
N_y	= circumferential force per unit length of shell
R	= radius of circular cross section
U	= air speed
U_c	= critical air speed (at which $V_0 = U - a \sec\alpha$)
U^*	= flutter speed—viz., minimum value of U_c
V	= axial wave speed, see Eq. (3.14) in reference 1
V_0	= V for free shell
V^*	= see Eq. (6.4) in reference 1
a	= velocity of sound in air
a_1	= velocity of sound—i.e., compression waves—in shell material
c	= wave speed of *surface* wave relative to coordinate system (x, y, z, t) fixed in still air, see Eqs. (3.6), (3.8), (3.14) in reference 1
f	= frequency
g	= structural damping factor, such that structural forces are multiplied by exp $(ig\ sgn\ \omega)$ for the harmonic motion exp $(i\omega t)$
h	= shell wall thickness
h^*	= minimum value of h required to prevent flutter in absence of prestresses or damping
i	= imaginary unit
m	= mass per unit area of shell wall
n	= displacement normal to wavefront, see Eq. (3.3) in reference 1; also denotes integer
p	= normal loading per unit area on shell wall
p_a	= aerodynamic pressure resulting from wave motion
p_i	= internal pressure in shell
sgn	= $sgn\ x = +1$ if $x > 0$ or -1 if $x < 0$
t	= time measured in (x, y, z) coordinate system fixed in still air
t_1	= time measured in (x_1, y_1, z_1) coordinate system fixed in shell
u, v, w	= axial, circumferential, and normal (radially inward) displacement of element of shell
w	= mapping function, see Eq. (4.5) in reference 1
x, y, z	= Cartesian coordinates fixed in still air, see Eq. (3.1) in reference 1
x_1, y_1, z_1	= Cartesian coordinates fixed in (and moving with) shell, see Eq. (3.1)
z	= argument of K_n, see Eq. (A-6) in reference 1
α	= azimuthal angle in polar coordinates (Fig. 2); helix angle of surface wave on shell
β	= see Eq. (4.6) in reference 1
γ	= see Eq. (4.6) in reference 1; also specific heat ratio for air
δ	= damping ratio, see Eq. (4.12) in reference 1
δ_0	= $-\delta$ at $g = 0$, see Eq. (4.13) in reference 1
$\delta_0{}^*$	= maximum negative damping ratio
ϵ	= see Eq. (7.17)
ϵ_x, ϵ_y	= strain parameters, see Eq. (5.7) in reference 1
ζ	= transverse displacement of panel ($\zeta = -w$ for cylindrical shell of circular cross section)
η	= see Eqs. (4.3b), (4.4) in reference 1
θ	= polar angle (Fig. 2); see Eqs. (3.9a), (3.9b) in reference 1
κ_x, κ_y	= stress parameters, see Eq. (7.11)
λ	= wavelength of *space* wave in x, y, z coordinates
λ_1	= wavelength of *surface* wave in x_1, y_1, z_1 coordinates
$\lambda_1{}^*$	= see Eq. (6.5) in reference 1
μ	= see Eq. (3.19) in reference 1
ν	= Poisson's ratio
ξ	= see Eq. (4.3b) in reference 1
ρ_a	= air density
ρ_f	= density of internal fluid
ρ_1	= density of shell material
σ_x, σ_y	= axial and circumferential prestresses
$\sigma_x{}^*$	= see Eqs. (7.5), (7.6)
υ	= see Eq. (4.3a) in reference 1
ϕ	= velocity potential (see Appendix A of reference 1)
ψ_n	= see Eq. (A-8) in reference 1

Received September 20, 1956.

† The material in this paper was taken from Ramo-Wooldridge Corporation Report GM-TR-32, May 25, 1956.

* Professor of Engineering; also Consultant, The Ramo-Wooldridge Corporation.

INTRODUCTION

The following analysis is continued from reference 1 and applies the theory of that paper to the flutter analysis of prestressed shells. An important example would be a liquid-fueled rocket.

The Sections, Equations, and Figures are numbered continuously from Part I (see reference 1).

(7) PRESTRESSED SHELL

WE NOW CONSIDER a prestressed shell, for which the wave speed given by Eq. (5.5) when the inertia of the internal fluid is neglected (a liquid-filled shell will be considered in the following section) may be expressed as‡

‡ $V^* = [3(1-\nu^2)]^{-1/4}(h/R)^{1/2}a_1$

$\lambda_1{}^* = 2\pi[12(1-\nu^2)]^{-1/4}(Rh)^{1/2}$

cf. Eqs. (6.4) and (6.5).

$$V_0^2(\lambda_1, \alpha) = (1/2)\,V^{*2}\{[(\lambda_1 \cos \alpha)/\lambda_1^*]^2 + [\lambda_1^*/(\lambda_1 \cos \alpha)]^2\} + [(\sigma_x + \sigma_y \tan^2 \alpha)/\rho_1] \quad (7.1)$$

The first term on the right-hand side of Eq. (7.1) is identical with Eq. (6.3), and σ_x and σ_y denote the axial and circumferential stresses, respectively. It then follows that the minimum wave speed for the prestressed shell is given by

$$(V_0)_{min} = \sqrt{V^{*2} + (\sigma_x/\rho_1)} \quad \text{at} \quad \lambda_1 = \lambda_1^* \text{ and } \alpha = 0 \quad (7.2)$$

The corresponding flutter speed is given by

$$U^* = a + \sqrt{V^{*2} + (\sigma_x/\rho_1)} \quad (7.3)$$

It follows from Eq. (7.3) that axial prestress increases the theoretical flutter speed, but that circumferential prestress has no effect on this speed. The prestress required to prevent flutter at any given speed, as determined from Eqs. (6.4) and (7.3), is

$$\sigma_x^* = \rho_1\{(U - a)^2 - [(h/R)/\sqrt{3(1 - \nu^2)}]a_1^2\}, \quad U > a \quad (7.4a)$$

$$= \rho_1(U - a)^2[1 - (h/h^*)] \quad (7.4b)$$

where h^*, the wall thickness required to prevent flutter in the absence of prestress, is given by Eq. (6.7). The result (7.4) is, of course, invalid for values of U too close to a, and the appropriate result at the sonic point is

$$\sigma_x^* = [E/\sqrt{3(1 - \nu^2)}][(h^* - h)/R] \quad \text{at } U = a \quad (7.5)$$

where h^* is given by Eq. (6.8). If h exceeds h^* the results (7.4) and (7.5) give the maximum compressive stress that could be allowed without producing flutter.

The stresses given by Eq. (7.4b) for duralumin and steel, evaluating a at sea level, are

$$\sigma_x^* = 4.3 \times 10^4[1 - (h/h^*)](M - 1)^2 \text{ psi (duralumin)} \quad (7.6a)$$

$$= 1.3 \times 10^5[1 - (h/h^*)](M - 1)^2 \text{ psi (steel)} \quad (7.6b)$$

If h is small compared with h^* it is evident that the prestresses required to prevent flutter may be of the same order as the ultimate allowable stresses. We also remark that if the axial prestress σ_x^* is produced by internal pressure the resulting circumferential stress is $2\sigma_x^*$.

We turn now to the calculation of the negative damping ratio δ_0 for speeds in excess of the flutter speed. If the wave speed given by Eq. (7.1) is substituted in the constraint (4.11)—viz., $V_0 = U - a \sec \alpha$—we obtain

$$(U - a \sec \alpha)^2 = (1/2)\,V^{*2}\{[(\lambda_1 \cos \alpha)/\lambda_1^*]^2 + [\lambda_1^*/(\lambda_1 \cos \alpha)]^2\} + [(\sigma_x + \sigma_y \tan^2 \alpha)/\rho_1] \quad (7.7)$$

Solving Eq. (7.7) for $\lambda_1 \cos \alpha$ yields two values having the geometric mean λ_1^*, of which, according to Eq. (4.13), the larger gives the larger value of δ_0; moreover, if, as we shall assume,

$$\sigma_y > \sigma_x \gg Eh/R \quad (7.8)$$

the effects of bending are negligible at the larger wavelength, which then is given approximately by [substituting V^* and λ_1^* in Eq. (7.7) from Eqs. (6.4) and (6.5) and dropping the bending term]

$$\lambda_1 = 2\pi R \sec \alpha \times \sqrt{[(U - a \sec \alpha)/a_1]^2 - [(\sigma_x + \sigma_y \tan^2 \alpha)/E]} \quad (7.9)$$

Substituting this value of λ_1 in Eq. (4.13b), we may express δ_0 as a function of α—viz.,

$$\delta_0 = (\sqrt{3}/4)(a_1\rho_a U^2 R/aEh)^{2/3} \times (M \cos \alpha)^{-4/3}\,(M \cos \alpha - 1)^{-5/3} \times [(M \cos \alpha - 1)^2 - (\kappa_x \cos^2 \alpha + \kappa_y \sin^2 \alpha)]^{1/3} \quad (7.10)$$

where the new stress parameters

$$\kappa_x = \sigma_x/\rho_1 a^2 = (a_1/a)^2\epsilon_x \quad (7.11a)$$

$$\kappa_y = \sigma_y/\rho_1 a^2 = (a_1/a)^2\epsilon_y \quad (7.11b)$$

have been introduced. We remark that the velocity of sound is relatively insensitive to changes of altitude; κ_x and κ_y are, therefore, relatively direct measures of the static stresses. The minimum Mach Number at which flutter can occur, say M_0, as obtained from Eqs. (7.3) and (6.4), may be expressed as

$$M_0 = 1 + \{1 + [Eh/\sigma_x R\sqrt{3(1 - \nu^2)}]\}^{1/2}\kappa_x^{1/2} \quad (7.12a)$$

$$\doteq 1 + \kappa_x^{1/2} \quad (7.12b)$$

where the approximation (7.12b) is based on the assumption (7.8).

The flutter motion at the initial Mach Number ($M = M_0$) is necessarily axially symmetric ($\alpha = 0$), but if $M > M_0$ (for fixed κ_x) flutter is possible over a range of values of α. We may anticipate, however, that maximum instability will correspond to $\alpha = 0$ in a finite range of Mach Numbers, say $M_0 \leq M \leq M_1$, while if $M > M_1$ the value of α will increase in consequence of the constraint $V_0 = U - a \sec \alpha$. In the former range it is expedient to write the maximum value of δ_0 in the form [setting $\alpha = 0$ in Eq. (7.10)]

$$\delta_0^* = [(a/a_1)(R/h)(\rho_a U^2/2\sigma_x)]^{2/3}\,F(M, \kappa_x), \quad M_0 \leq M \leq M_1 \quad (7.13)$$

$$F(M, \kappa_x) = 3^{1/2}2^{-4/3}\kappa_x^{2/3}M^{-4/3} \times (M - 1)^{-5/3}\,[(M - 1)^2 - \kappa_x]^{1/3} \quad (7.14)$$

F is plotted in Fig. 9 for values of M between M_0 and M_2, where M_2 is the value at which F achieves its maximum value as a function of M; it may be proved that $M_2 > M_1$, so that F is of no direct interest outside of this range.

The determination of M_1 and δ_0^* if $M > M_1$ is expedited by rewriting (7.10) in the form

$$\delta_0 = [(a/a_1)(R/h)(\rho_a U^2/2\sigma_y)]^{2/3}G(C; \kappa_y, \epsilon) \quad (7.15a)$$

$$= [(a/a_1)(\rho_a U^2/2p_i)]^{2/3}G(C; \kappa_y, \epsilon) \quad \text{if } \sigma_y = p_i R/h \quad (7.15b)$$

where

$$C = M \cos \alpha \tag{7.16}$$

$$\epsilon = M^{-2}[1 - (\sigma_x/\sigma_y)] \tag{7.17}$$

$$G(C; \kappa, \epsilon) = 3^{1/2}2^{-4/3}\kappa_y^{2/3}C^{-4/3}(C - 1)^{-5/3} \times [(C - 1)^2 - \kappa_y(1 - \epsilon C^2)]^{1/3} \tag{7.18}$$

The form (7.15b) exhibits the dependence of δ_0 on the ratio of dynamic $(\rho_a U^2/2)$ to internal (p_i) pressure when σ_y is a result of pressurization. The function $G(C)$ vanishes for some value of $C > 1$, say $C_0 (C_0 = M_0$ at $\alpha = 0)$, and is real and positive for all $C > C_0$. The derivative $G'(C)$—namely

$$G'(C) = 3^{-1/2}2^{-4/3}\kappa_y^{2/3}C^{-7/3}(C - 1)^{-8/3} \times [(C - 1)^2 - \kappa(1 - \epsilon C^2)]^{-2/3} \cdot \{\kappa_y[(9C - 4) - \epsilon C^2(7C - 2)] - (7C - 4)(C - 1)^2\} \tag{7.19}$$

has, by Descartes' rule of signs, one and only one zero in $C > 1$, say C_m, corresponding to a maximum value of G, say G_m. It follows that the maximum instability occurs at $\alpha = 0$ if $C_m \geq M$ (since then $M \cos \alpha = C_m$ does not yield a real value of α) and at $\alpha = \cos^{-1}(C_m/M)$ if $C_m \leq M$. The Mach Number at which $C_m = M$ is the aforementioned M_1.

The maximum value of δ_0 for $M \geq M_1$ may be expressed as

$$\delta_0^* = [(a/a_1)(\rho_a U^2/2p_i)]^{2/3} G_m(\kappa_y, \epsilon), \quad M \geq M_1 \tag{7.20}$$

where G_m is obtained by equating the cubic in the braces of (7.19) to zero, solving for C_m, and substituting the result in (7.18). The value of M_1 is determined implicitly by $C_m(\kappa_y, \epsilon)$, since, for fixed (σ_x/σ_y),

$$M_1 = C_m\{\kappa_x, M_1^{-2}[1 - (\sigma_x/\sigma_y)]\} \tag{7.21}$$

M_1 is plotted as a function of κ_x for various stress ratios in Fig. 10. A rough approximation is found to be

$$M_1 \doteq 1 + (5\kappa_x/3)^{1/2} \tag{7.22}$$

and also is plotted in Fig. 10. G_m is plotted as a function of ϵ for various κ_y in Fig. 11. C_m, which is required in determining the helix angle and frequency of maximum instability is plotted in Fig. 12.

The graphical presentation of δ_0^* as an explicit function of M for $M > M_1$ would require the introduction of both κ_x and κ_y as parameters, and the results would be too cumbersome for arbitrary stress ratios. This presentation is made in Fig. 13 for the important, special case $\sigma_x = (1/2)\sigma_y$, however, in order to exhibit more clearly the variations of δ_0^* with M.

It is very likely that panel flutter would be most serious for Mach Numbers in the neighborhood of M_1, and, in any event, the value of δ_0^* calculated at $M = M_1$ furnishes an approximate upper bound to the value at other Mach Numbers (provided, of course, that the actual dynamic pressure is used in the calculation). Using the approximation to $M_1 - 1$ given by Eq. (7.22), the corresponding approximation to the upper bound of δ_0^* given by Eqs. (7.13) and (7.14) is

$$\delta_0^* < 0.393\,(\sigma_x/\rho_1 a^2)^{1/6}[1 + (5\sigma_x/3\rho_1 a^2)^{1/2}]^{-4/3} \times [(a/a_1)(R/h)(\rho_a U^2/2\sigma_x)]^{2/3} \tag{7.23a}$$

or, for a pressurized cylinder,

$$\delta_0^* < 0.393\,(a/a_1)^{1/3}(\sigma_y/\sigma_x)^{1/2}(p_i R/Eh)^{1/6} \times [1 + 1.29(a_1/a)(\sigma_x/\sigma_y)^{1/2}(p_i R/Eh)^{1/2}]^{-4/3} \times (\rho_a U^2/2p_i)^{2/3} \tag{7.23b}$$

The frequencies corresponding to Eqs. (7.13) and (7.15) may be determined by substituting λ_1 from Eq. (7.9) in Eq. (6.12) and expressing the result in the dimensionless forms

$$2\pi f R/a_1 = \cos^2 \alpha (M \cos \alpha - 1)[(M \cos \alpha - 1)^2 - (\kappa_x \cos^2 \alpha + \kappa_y \sin^2 \alpha)]^{-1/2} \tag{7.24a}$$

$$= (3^{3/4}/4)M^{-2}\kappa_y^{1/4} \times [\kappa_y^{-1/2}(C - 1)G(C; \kappa_y, \epsilon)]^{-3/2} \tag{7.24b}$$

$$= (M - 1)[(M - 1)^2 - \kappa_x]^{-1/2} \quad \text{at } \alpha = 0 \tag{7.24c}$$

where C and G are defined by Eqs. (7.16) and (7.18). The frequency of maximum instability may be determined by substituting $\kappa_y^{-1/2}(C_m - 1)$ and G_m (from Figs. 11 and 12) in Eq. (7.24b) if $M \geq M_1$ and directly from Eq. (7.24c) if $M \leq M_1$. We note that the approximation (7.22) yields 1.58 for the right-hand side of Eq. (7.24c), giving a frequency 12 per cent higher than Eq. (6.13) for an unpressurized shell at the minimum flutter speed.

(8) Liquid-Filled Pressurized Cylinder

We consider in this section a pressurized, liquid-filled cylinder—typically, a fuel tank. We shall assume that the density of the liquid is such that

$$\rho_i \lambda_1 \gg 2\pi\rho_1 h \tag{8.1}$$

so that the inertia of the shell (m_1) may be neglected in calculating the wave speed; this assumption usually would be satisfied for practical fuel tanks, since ρ_i would be of the same order of magnitude as (although smaller than) ρ_1, while λ_1 must be large compared with the wall thickness. We also shall neglect bending, the implicit assumption being that of Eq. (7.8); other things being equal, bending is less important for a liquid-filled than for a gas-filled tank in virtue of the larger wavelength at which the wave speed exhibits its minimum value.

The preloads are given by

$$N_x = (1/2)N_y = p_i R/2 \tag{8.2}$$

and the wave speed given by Eq. (5.5) may be placed in the form

$$V_0^2(\lambda_1, \alpha) = (Eh/\rho_i R)[(\lambda_1 \cos^2 \alpha)/2\pi R] + (p_i/\rho_i)[(\lambda_1 \cos^2 \alpha)/2\pi R]^{-1}[1 - (1/2)\cos^2 \alpha] \tag{8.3}$$

This wave speed has the minimum value

$$(V_0)_{min} = (2Ep_i h/\rho_i^2 R)^{1/4} \quad \text{at } \lambda_1 = \lambda_1^* = 2\pi R\sqrt{p_i R/2Eh} \text{ and } \alpha = 0 \tag{8.4}$$

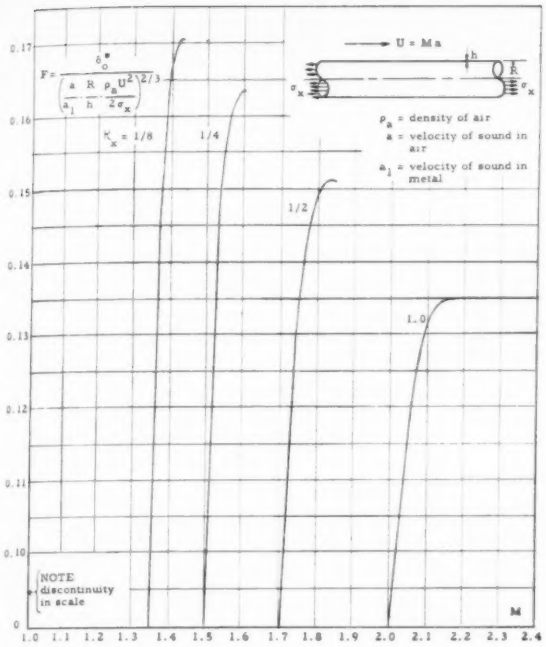

FIG. 9. The damping ratio for a pressurized cylindrical shell, as given by Eqs. (7.13) and (7.14), on the assumption that both bending of the shell and the inertia of the internal fluid are negligible and that $M < M_1$ (see Fig. 10); if $M > M_1$, the damping ratio is given by Fig. 11.

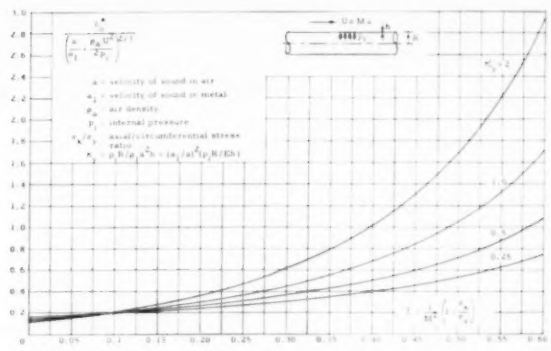

FIG. 11. The damping ratio for a pressurized cylindrical shell, as given by Eq. (7.20), on the assumptions that both bending of the shell and the inertia of the internal fluid are negligible and that $M > M_1$ (see Fig. 10); use Fig. 9 if $M < M_1$.

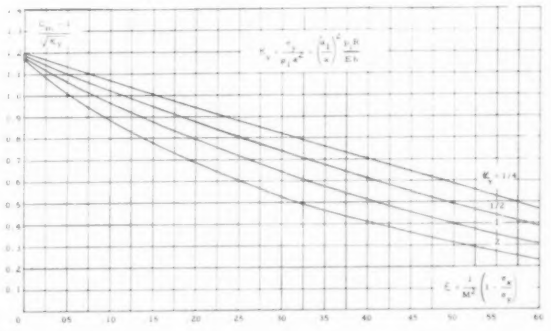

FIG 12. $\kappa_y^{-1/2}\,(C_m - 1)$ vs. ϵ_y where C_m is determined by $G'(C) = 0$.

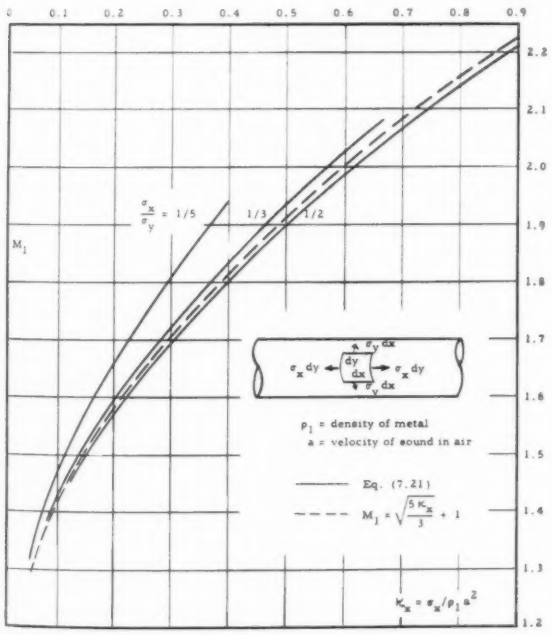

FIG. 10. The parameter M_1, required in determining whether Eq. (7.13) or Eq. (7.20), corresponding to Figs. 9 and 11, respectively, should be used to determine the damping ratio for maximum instability.

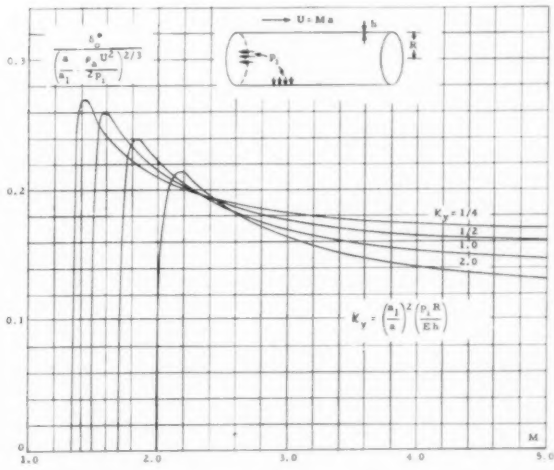

FIG. 13. The damping ratio for a pressurized cylindrical shell, assuming that both bending of the shell wall and the inertia of the internal fluid are negligible and that the (static) axial stress is one-half the circumferential stress.

and the corresponding flutter speed is

$$U^* = a + (2Ep_i h/\rho_i^2 R)^{1/4} \tag{8.5}$$

It follows that the internal pressure required to prevent flutter is

$$p_i^* = \rho_i^2 (U - a)^4 R/2Eh \tag{8.6}$$

The negative damping ratio when U exceeds U^*, obtained by neglecting the shell inertia in Eq. (4.13b), is

$$\delta_0 = (\sqrt{3}/4)(\rho_a/\rho_i)^{2/3}(M \cos \alpha - 1)^{-5/3} \tag{8.7}$$

subject to the constraint ($V_0 = U - a \sec \alpha$)

$$(Eh/\rho_i R)[(\lambda_1 \cos^2 \alpha)/2\pi R] + (p_i/\rho_i)[(\lambda_1 \cos^2 \alpha) \div 2\pi R]^{-1}[1 - (1/2)\cos^2 \alpha] = (U - a \sec \alpha)^2 \tag{8.8}$$

It is evident that the maximum value of δ_0 given by Eq. (8.7) corresponds to the smallest value of cos α permitted by Eq. (8.8); this, in turn, requires the left-hand side of Eq. (8.8) to be a minimum with respect to variations of λ_1. Imposing the latter condition, we may place the results in the form

$$\lambda_1 = \lambda_1^* \sqrt{2 - \cos^2 \alpha} \sec^2 \alpha \tag{8.9a}$$

$$(M \cos \alpha - 1) = (M^* - 1)(2 - \cos^2 \alpha)^{1/4} \cos \alpha \tag{8.9b}$$

where λ_1^* is given by Eq. (8.4), and M^* is the Mach Number specified by Eq. (8.5).

The exact determination of cos α from Eq. (8.9b) requires the solution of a sextic equation, but the approximation

$$\cos \alpha \doteq (M - M^* + 1)^{-1} \tag{8.10}$$

obtained by neglecting the variation of cos α in the factor $(2 - \cos^2 \alpha)^{1/4}$, is exact for $M = M^*$ and exhibits a maximum error of $0.19(M^* - 1)(M - 1.19M^* + 1.19)^{-1}$ relative to unity. Substituting Eq. (8.10) in the right-hand side of Eq. (8.9b) to determine the corresponding approximation to $M \cos \alpha - 1$, the damping ratio given by Eq. (8.7) becomes

$$\delta_0^* = (\sqrt{3/4})(\rho_a/\rho_i)^{2/3}[(M - M^* + 1)/(M^* - 1)]^{5/3} \times [2 - (M - M^* + 1)^{-2}]^{-5/12} \tag{8.11a}$$

$$= 0.43(\rho_i/\rho_a)^{1/6}(p_0^2 R/Ep_i h)^{5/12}(M - M^* + 1)^{5/3} \times [2 - (M - M^* + 1)^{-2}]^{-5/12} \tag{8.11b}$$

where the specific heat ratio has been taken as 1.4 in evaluating a in Eq. (8.11b), and p_0 is the free-stream pressure.

It might be thought that, in analogy with the action of oil on disturbed water, the friction between the internal fluid and the shell could provide appreciable damping. This analogy is, in fact, exact for a wave of given length (λ_1) and speed ($V \cos \alpha$) insofar as the wavelength is (as already assumed) short and the oil film is inextensible, and we find for the (positive) damping ratio[2]

$$\delta_i = (1/2)\sqrt{\pi \nu_i / V \lambda_1 \cos \alpha} \tag{8.12}$$

where ν_i is the kinematic viscosity of the internal fluid. It does not appear that δ_i could exceed 10^{-3} for practical configurations and a fluid having dynamical properties approximating those of water. We remark that we have not proved that δ_i is directly additive to the damping ratio calculated in the absence of internal friction, but in view of the negligible magnitude of δ_i the question is of little importance.

References

[1] Miles, J. W., *Supersonic Flutter of a Cylindrical Shell*, Journal of the Aeronautical Sciences, Vol. 24, No. 2, pp. 107–118, February, 1957.

[2] Lamb, H., *Hydrodynamics*, Dover Publications, p. 632, New York, 1945.

Notice to Contributors

Manuscripts submitted for publication *must* be double- or triple-spaced originals. There should be wide margins on all sides of the sheets and triple spacing around formulas to allow for the marking of directions to the printer.

Original drawings (jet black India ink on white paper or tracing cloth) should accompany the manuscript. *(Blueprints are not acceptable.)* Photographs *must* be on glossy white paper. The smallest lettering on 8- by 10-in. figures should be no less than 1/4 in. high.

Formulas should be typewritten or carefully written in pen and ink. The difference between capital and lower-case letters and Greek symbols should be clearly distinguished.

See Inside Back Cover of this issue for further details

On Unsteady Interaction Between a Weak Thermal Layer and a Strong Plane Oblique Shock†

C. T. CHANG*

The Johns Hopkins University

SUMMARY

A problem of unsteady interaction between a weak upstream temperature disturbance and a plane oblique shock is investigated. The shock is assumed to be located at the concave corner of a wall. The temperature disturbance is taken as a layer of hot air of constant strength—namely, a step function. Its wave front is inclined at a definite angle with respect to the upstream unperturbed flow (see Fig. 1). It is found for such a configuration that, even for weak upstream disturbance, mixed flow (a supersonic region outside and a subsonic region inside a sonic circle, respectively) usually occurs downstream of the shock. Using a general concept of conical flow, the qualitative nature of the flow field downstream is predicted. Subsequently, a method for its quantitative investigation is presented. Based on the concept of constant states, the flow in the supersonic region is determined by the method of characteristics; the flow in the subsonic region is determined by following a procedure similar to the one used by Lighthill in his investigation about the diffraction of blast waves.

SYMBOLS

U_1, U = velocity of the unperturbed main flow upstream and downstream of the shock, respectively

A_1, A = speed of sound of the unperturbed main flow upstream and downstream of the shock, respectively

M_1, M = Mach Number of the unperturbed main flow upstream and downstream of the shock, respectively

ϵ = inclination of the unperturbed shock plane with respect to the main flow direction upstream of the shock

β = inclination of the unperturbed shock plane with respect to the main flow direction downstream of the shock

N = component of the downstream Mach Number normal to the shock, $N = M \sin \beta$

x^*oy^* = coordinate system pertaining to the shock, with y^* axis taken in the plane of the shock, Fig. 1

xoy = coordinate system pertaining to the downstream unpertarbed flow with x axis taken in the direction of the main flow velocity, U, Fig. 1

p_m = pressure of the unperturbed main flow

T_m = temperature of the unperturbed main flow

C_p = specific heat of the medium at constant pressure

γ = ratio of specific heats of the medium

Δp, ΔT, $\Delta \vec{u}$ = perturbation of pressure, temperature, and velocity of the flow field, respectively

p, T, $\vec{u}$ = dimensionless quantities of the above perturbations as defined in Section 2, Eq. (2.2)

$\vec{u}_l$, $\vec{u}_s$ = irrotational part and rotational part of the perturbed velocity field $\vec{u}$, respectively

u^*, v^* = components of velocity perturbation normal to and parallel to the unperturbed shock plane, respectively

δ = inclination of the upstream temperature jump with respect to the main flow velocity U_1, Fig. 1

C_s = drift speed of the upstream temperature jump along the shock, Fig. 1

$\psi(y^*, \tau)$ = shock displacement

ψ_y^*, $A\psi_\tau$ = local shock angle and local shock propagation speed, respectively

ξ, η = conical coordinates corresponding to the physical coordinates x, y, and τ, Eq. (2.4)

ξ^*, η^*; ξ', η'; $\bar{\xi}$, $\bar{\eta}$ = derived conical coordinates appearing in the text

r, θ = polar coordinates corresponding to ξ', η'

r, $\bar{\theta}$ = polar coordinates corresponding to $\bar{\xi}$, $\bar{\eta}$

σ = a characteristic coordinate for the flow in the hyperbolic region, Eq. (3.2)

ρ = a radius vector, defined by Tschaplygin's transformation, Eq. (3.11)

Subscripts

m refers to the unperturbed main flow

$-$ refers to upstream flow parameters in the vicinity of the shock

$+$ refers to downstream flow parameters in the vicinity of the shock

(1) INTRODUCTION

RECENT INVESTIGATIONS SHOWED—both theoretically and experimentally—a great interest regarding problems of interaction between thermal layers and shock waves.[1-3] Most of these investigations, however, are confined to interactions steady in time. Two types of interaction were considered; the upstream temperature disturbance was taken either as weak[1, 2] or strong.[3] For weak interaction, the perturbed pressure field downstream of the shock, depend-

Received October 14, 1957.

† This investigation was sponsored by Project Squid, which is jointly supported by the Office of Naval Research, the Office of Scientific Research (Air Force), and the Office of Ordnance Research (Army) under Contract Number N6-ORI-105 T.O. III, NR-098-038. The author wishes to thank Professors F. H. Clauser and L. S. G. Kovasznay for their encouragement and discussion.

* Formerly, Research Assistant, Aeronautics Department. Now, Research Fellow in Hydrodynamics, Harvard University.

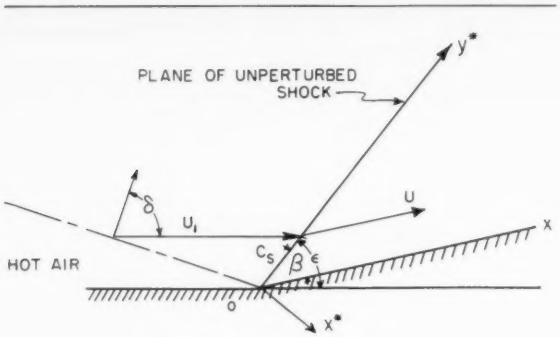

FIG. 1. Model of interaction.

ing on the shock angle concerned, is either entirely supersonic[1] or entirely subsonic.[2] For strong interaction, mixed flow near the foot of the shock was reported.[3] The object of this paper is to show that if the flow is unsteady, then even for weak upstream disturbance, mixed flow, usually, occurs downstream of the shock.

As a model of interaction, the shock is taken to be originated at the concave corner of a wall, and the upstream disturbance is taken to be a jump discontinuity of constant strength, its discontinuity front inclined at a definite angle to the upstream main flow velocity. The upstream disturbance thus drifts at a constant speed along the shock. From dimensional reasoning, the perturbed flow in the downstream must be of the conical nature. Based on the general concept of conical flow,[4] the qualitative nature of the downstream flow field can be predicted at ease. It is shown that the flow field downstream of the shock is divided into two regions; a supersonic region outside a sonic circle and a subsonic region inside a sonic circle.

Finally, a method for the quantitative evaluation of the perturbed flow is presented. In the supersonic region, the solution is obtained by using the concept of constant states and the method of characteristics; in the subsonic region, the solution is obtained by following a general procedure similar to the one used by Lighthill in his investigation concerning diffraction of blast waves.[5]

(2) Formulation of the Problem

The Model

As a model of our analysis, the medium is taken to be an ideal gas, inviscid and obeying perfect gas laws with constant specific heats; the shock is assumed to be originated at a concave corner of a wall. In view of most cases occurred in practice, the downstream main flow is assumed to be supersonic. The upstream temperature disturbance is assumed to have a constant jump, ΔT; the normal to its discontinuity front is inclined at an angle δ with respect to the upstream main flow U_1. The front of the discontinuity therefore advances at a constant speed

$$C_s = [\cos \delta / \cos (\delta - \epsilon)]U_1 \tag{2.1}$$

along the shock (see Fig. 1).

Boundary Conditions

For convenience of analysis, the flow parameters will be replaced by their corresponding nondimensionalized ones. Thus, if Δp, ΔT, and $\Delta \vec{u}$ denote the perturbations of pressure, temperature, and velocity, their corresponding dimensionless parameters will be denoted by

$$p = \Delta p / \gamma p_m, \quad T = \Delta T / T_m, \quad \vec{u} = \Delta \vec{u} / A \tag{2.2}$$

In the above, p_m and T_m are the pressure and temperature of the unperturbed main flow, γ is the ratio of specific heats of the gas, and A is the speed of sound of the medium. We shall also adopt the convention that whenever no subscript is attached, the flow parameters are those in the region downstream of the shock; for similar flow parameters upstream of the shock, a subscript 1 will be used—for example, the pressure of the main flow upstream of the shock will be denoted by p_{1m}, while the pressure of the main flow downstream of the shock will be denoted by p_m.

Referring to a set of coordinate axes ox^*y^* with the y^* axis taken in the plane of the unperturbed shock, (Fig. 1), using the conservation laws of mass, momentum and energy, the flow conditions across the shock can be written as[1]

$$\begin{bmatrix} T_+ \\ p_+ \\ u_+^* \\ v_+^* \end{bmatrix} = \begin{bmatrix} \Lambda_{11} \\ \Lambda_{21} \\ \Lambda_{31} \\ 0 \end{bmatrix} T_- + \begin{bmatrix} \pi_{11} M \cos \beta \\ \pi_{21} M \cos \beta \\ \pi_{31} M \cos \beta \\ \pi_{41} \end{bmatrix} \psi_{y^*} + \begin{bmatrix} \pi_{11} \\ \pi_{21} \\ \pi_{31} \\ 0 \end{bmatrix} \psi_\tau \tag{2.3}$$

In the above, u^* and v^* are components of the perturbed velocity taken normal to and tangential to the unperturbed shock plane respectively. Λ_{11}, Λ_{21}, . . . π_{11}, π_{21}, . . . etc. are parameters depending on the shock strength, defined as the ratio of main flow pressures across the shock—i.e., p_m/p_{1m}. Their explicit form was given in reference 6.

Besides these shock conditions, the velocity component, v, normal to the wall and the shock displacement, ψ, at the corner of the wall must vanish at all time.

Governing Equations and General Nature of the Solution

As the effect of the upstream disturbance on the shock depends only on the drift speed C_s, from dimensional reasoning, one would expect that the perturbed flow parameters downstream of the shock must also be functions of some physical parameters having the dimension of a velocity. Specifically, if one follows the idea of Busemann,[4] and introduces a set of coordinates defined by

$$\xi = x/\tau, \quad \eta = y/\tau \tag{2.4}$$

then the physical parameters, e.g., p, T, u, v, etc. of the

perturbed flow field must be functions of (ξ, η). The flow field in the (ξ, η) plane can be viewed as a representation of the perturbed flow at the instant of $\tau = 1$. The flow field at any other instant can be obtained by a proper magnification or reduction in proportion to the instant to be considered—i.e., by taking a proper cut along the τ axis (see Fig. 2). With respect to the present frame of reference, the conservation laws of mass and momentum can be written as

$$\left.\begin{aligned} &\text{mass:} && (M - \xi)p_\xi - p_\eta = -(u_\xi + v_\eta) \\ &\text{momentum:} && (M - \xi)u_\xi - \eta u_\eta = -p_\xi \\ &&& (M - \xi)v_\xi - \eta v_\eta = -p_\eta \end{aligned}\right\} \quad (2.5)$$

For analytical works, it is more convenient to refer them to a set of polar coordinates defined by

$$r = [(\xi - M)^2 + \eta^2], \quad \theta = \tan^{-1}[\eta/(\xi - M)] \quad (2.6)$$

In terms of the polar coordinates, Eq. (2.4) becomes

$$\left.\begin{aligned} rp_r &= \cos\theta\, u_r + \sin\theta\, v_r - (\sin\theta/r)\, u_\theta + (\cos\theta/r)v_\theta \\ ru_r &= \cos\theta\, p_r - \sin\theta\, p_\theta/r \\ rv_r &= \sin\theta\, p_r + \cos\theta\, p_\theta/r \end{aligned}\right\} \quad (2.7)$$

It is easy to see that the particular solution of the velocity field associated with the pressure field is irrotational, or it is the drift velocity associated with a sound wave; while the homogeneous part of the solution represents the rotational part of the velocity field—i.e., the shear waves. From Eq. (2.7), three characteristic directions can be obtained; they are

$$\left.\begin{aligned} C_a&: \ \theta = \text{constant} \\ C_+&: \ \theta + \sec.^{-1} r = \text{constant} \\ C_-&: \ \theta - \sec.^{-1} r = \text{constant} \end{aligned}\right\} \quad (2.8)$$

While the characteristic θ = constant is valid for the whole region downstream of the shock, the last two characteristics exist only outside the sonic circle—i.e., for $r > 1$ only. The characteristics $C+$ and $C-$ can be shown to be simply lines tangent to the sonic circle; the circle itself is an envelope of the characteristics, hence, it is sometimes known also as the Mach circle. Physically, these characteristics represent discontinuity fronts of sound waves generated downstream. Similarly, the characteristic C_a corresponds to accompanying discontinuity fronts of entropy (or temperature disturbance) and vorticity waves formed at the shock.

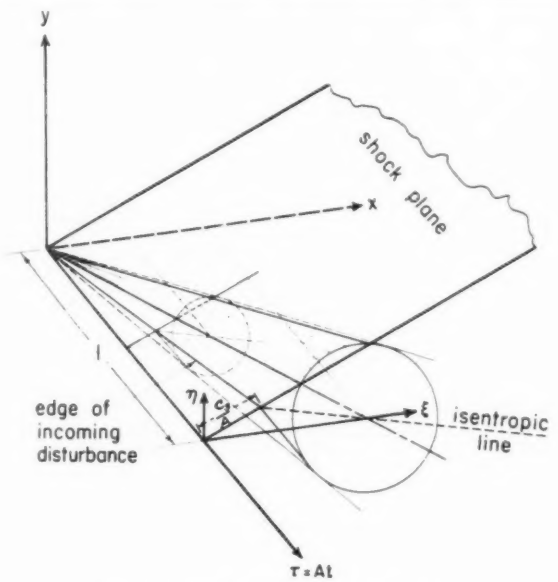

FIG. 2. Conical coordinates of flow field.

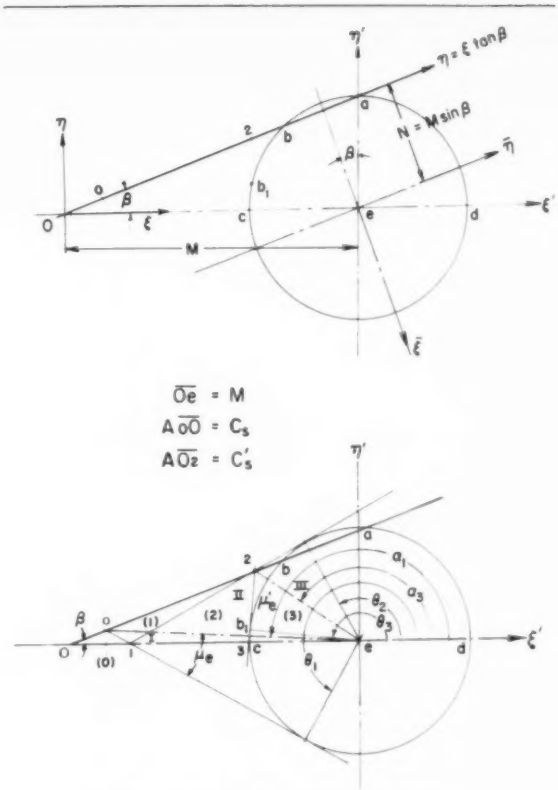

FIG. 3. Flow field in hyperbolic region.

With the aid of these characteristic directions, a qualitative examination of the downstream flow field can be made at once. A specific example is given in Fig. 3. Thus, if 0o represents the drift speed C_s of the upstream temperature discontinuity, then 01 and 0e will represent the sound wave and the vorticity wave (also the entropy wave) generated, respectively, at the shock. 12 will represent the sound wave reflected at the wall; 23, its reflection at the shock; 2e, the accompanying vorticity and entropy wave formed at the shock.

The sound field in regions (0), (1), and (2) are hyperbolic in nature—i.e., the pressure disturbances are waves with constant amplitudes. The sound field in region (3) is of a mixed type, hyperbolic outside and elliptic inside the sonic circle. If one wants to explore further about the downstream flow field quantitatively, one finds that it is most convenient to analyze the

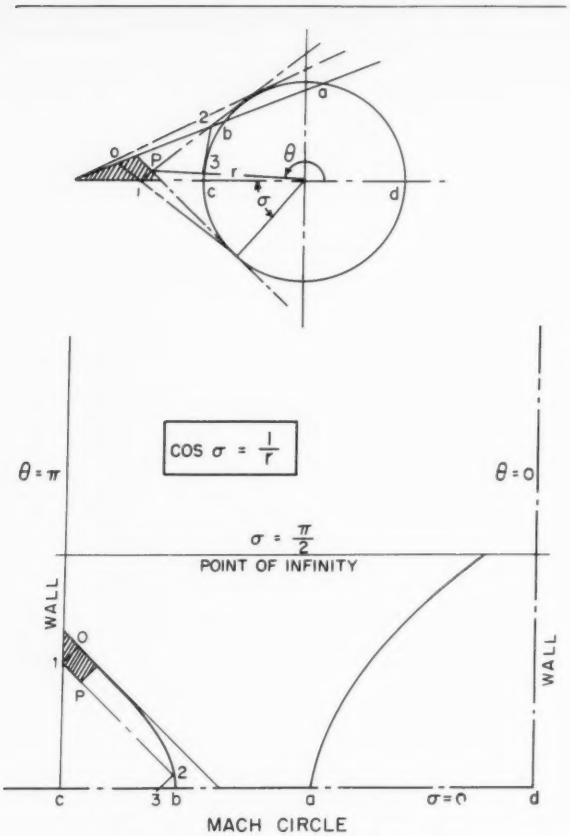

FIG. 4. Mapping of hyperbolic region.

pressure field first. From Eq. (2.7), after the elimination of u and v, a single governing equation for the perturbed pressure p results, thus,

$$r^2(r^2 - 1)p_{rr} + r(2r^2 - 1)p_r = p_{\theta\theta} \qquad (2.9)$$

Since Eq. (2.9) is hyperbolic or elliptic according to whether r is greater or less than unity, this confirms our previous statement that the downstream flow field is of the mixed type.

(3) METHOD OF SOLUTION

Flow Field in the Hyperbolic Region

When $r > 1$, Eq. (2.9) can be reduced to a simple wave equation with respect to the characteristic coordinates θ and σ thus:

$$p_{\theta\theta} - p_{\sigma\sigma} = 0 \quad \text{for } r > 1 \qquad (3.1)$$

where
$$\sigma = \sec.^{-1}(r) \qquad (3.2)$$

Eq. (3.2) can be viewed as a transformation which maps a point (r, θ) in the physical plane to a point (σ, θ) in an image plane. In particular, the Mach circle is mapped into the coordinate axis $\sigma = 0$; the characteristics which are not fixed in the (r, θ) plane are mapped into two sets of lines inclined at 45° to the coordinate axis in the (σ, θ) plane (see Fig. 4). From Fig. 4, it is evident that, unless the shock degenerates into a Mach wave, the family of characteristics coming from the wall will intersect with the shock; thus reflection phenomena will continue (although the strength of the reflected wave might be zero in some special case),[1] until the last characteristic hits the coordinate axis $\sigma = 0$—i.e., the Mach circle. Clearly, the zone of influence for a fixed field point P in the hyperbolic region is the region on the left of the two characteristics passing through the point. Although the dominating effect at the point is coming from waves generated at the shock caused by the upstream disturbance and the first reflection at the wall, if the point under consideration is not too far away from the corner of the wall, then clearly the effect of the corner will have a great significance. Consequently, in order to investigate the flow field in the hyperbolic region, first of all one needs the knowledge of the flow field near the corner. Once the wave front of the upstream disturbance has passed the corner of the wall, the transient effect of the disturbance is gone. As a result, one might expect that the flow field near the corner would be the same as that produced by a steady disturbance; its region of validity is limited to that defined by the characteristics —i.e., up to the line 01 for the sound field and up to the line 0e for the vorticity field as indicated in Fig. 3. Using the fact that we are looking for a solution near the corner of the wall where the vertical component of the perturbed velocity, $v = 0$, the boundary conditions at the shock, Eq. (2.3), in the present case, reduces to

$$\left.\begin{aligned} p_+ &= \Lambda_{21} T_1 + \pi_{21}(M \cos\beta)\psi_{y^*} \\ u_+ \sin\beta &= \Lambda_{31} T_1 + \pi_{31}(M \cos\beta)\psi_{y^*} \\ u_+ \cos\beta &= \pi_{41}\psi_{y^*} \end{aligned}\right\} \qquad (3.3)$$

where u_+ is the component of the velocity perturbation along the wall immediately behind the shock. Since the region upstream of the shock consists of constant states[7] separated by the discontinuity front of the given temperature jump, the hyperbolic region outside the Mach circle in the flow field downstream of the shock must also consist of regions of constant states separated by characteristics, and it follows that the above three equations will be just sufficient for the determination of the three unknown quantities p, u, and ψ_{y^*}. In particular, the sound field is given by

$$p_0 = \frac{(\Lambda_{21}C - \Lambda_{31})M \cos^2\beta + \Lambda_{21} B \sin\beta}{M \cos^2\beta + B \sin\beta} T_1 \qquad (3.4)$$

where
$$C = \pi_{31}/\pi_{21}, \quad B = -\pi_{41}/\pi_{21}$$

and
$$(u_t)_0 = -p_0/M$$

Since the shock displacement in terms of the conical coordinates is

$$\psi(y^*, \tau) = \chi(\eta^*)\tau \qquad (3.5)$$

it follows then at the instant $\tau = 1$, or $\eta^* = C_s/A$,

$$\chi_0 = [\Lambda_{31} T_1 \cos\beta/(\pi_{41} \sin\beta - \pi_{31} M \cos^2\beta)] \times (C_s/A) \qquad (3.6)$$

In a similar manner, the vorticity and temperature

field near the corner can be determined. To explore further the flow field in the adjacent zones, it might be worthwhile to take another close look at the governing equation for the perturbed pressure in its original form, Eq. (2.9). If one compares our present problem, a two-dimensional unsteady flow with no restriction on rotationality, with the known case of three-dimensional irrotational steady conical flow about supersonic wings,[8,9] one notices that our governing equation for the perturbed pressure (more general, for any parameters p, u_i or v_i of the sound field) has the identical structure as the governing equation for the velocity perturbation in the latter case, provided we identify our present pressure perturbation p with the axial component $-w \cot(\sin^{-1} 1/M)$ in the latter case. Using this analogy and the results of reference 8, it is easy to verify that the general solution of the flow field for $r > 1$ is given by

$$\left.\begin{aligned} p &= \int^{\theta-\sigma} g(\omega)\, d\omega + \int^{\theta+\sigma} f(\omega)\, d\omega \\ u_i &= \int^{\theta-\sigma} \cos\omega\, [g(\omega)]\, d\omega + \int^{\theta+\sigma} \cos\omega\, [f(\omega)]\, d\omega \\ v_i &= \int^{\theta-\sigma} \sin\omega\, [g(\omega)]\, d\omega + \int^{\theta+\sigma} \sin\omega\, [f(\omega)]\, d\omega \\ u_s &= \int^{\alpha} \cos\omega\, [I(\omega)]\, d\omega \\ v_s &= \int^{\alpha} \sin\omega\, [I(\omega)]\, d\omega \end{aligned}\right\} \tag{3.7}$$

where $f(\omega)$, $g(\omega)$, and $I(\omega)$ are periodic functions of period 2π such that

$$\int_0^{2\pi} g(\omega)\, d\omega = \int_0^{2\pi} \cos\omega\, [g(\omega)]\, d\omega = \int_0^{2\pi} \sin\omega [g(\omega)]\, d\omega = 0 \tag{3.8}$$

Similar relations hold for $f(\omega)$ and $I(\omega)$. In the above, (u_i, v_i) is the irrotational part and (u_s, v_s) is the rotational part of the perturbed velocity field, respectively.

Denoting the pressure jump across the characteristic 01 by Δp and the velocity jump for the shear wave across the characteristic 0e by Δe according to Eq. (3.7), the jump of the flow parameters across these characteristics are given by

$$\left.\begin{aligned} \Delta p &= p_i - p_0 \\ \Delta u_i &= (u_i)_1 - (u_i)_0 = \Delta p \cos\theta_1 \\ \Delta v_i &= (v_i)_1 - (v_i)_0 = \Delta p \sin\theta_1 \\ \Delta u_s &= (u_s)_{II} - (u_s)_I = \Delta e \cos\alpha_1 \\ \Delta v_s &= (v_s)_{II} - (v_s)_I = \Delta e \sin\alpha_1 \end{aligned}\right\} \tag{3.9}$$

The flow parameters immediately behind the shock now are seen to be expressible in terms of the two unknown jumps, Δp and Δe. The local shock displacement $x(\eta^*)$ furnishes an additional unknown. Using the last three equations of the shock conditions of Eq. (2.3), with the upstream disturbance T_-, deleted, these unknown quantities can be determined algebraically.

In view of the fact that discontinuities of flow parameters can occur only across characteristics and the concept regarding constant states,[7] the entire flow field in the hyperbolic region can be evaluated in a similar manner.

In summary, the physical phenomena occurring in the hyperbolic region, generally, will consist of the following: generation of waves of all three modes—sound, vorticity, and temperature spottiness—at the shock; reflection of sound waves at the wall; and reflection of sound waves at the shock with simultaneous production of waves of the other two modes. The process will continue or stop at any one of these stages whenever the last characteristic of the sound wave hits the Mach circle. An example illustrating all the above-mentioned phenomena has been given already in Fig. 3.

Flow Field in the Elliptic Region

Inside the Mach circle, $r < 1$, the flow field is elliptic. The governing equation for the perturbed pressure, Eq. (2.9), can be reduced to a Laplace equation in terms of a new set of polar coordinates (ρ, θ) thus,

$$(1/\rho)\,(\partial/\partial\rho)\,[\rho(\partial p/\partial\rho)] + (1/\rho^2)\,(\partial^2 p/\partial\theta^2) = 0 \quad \text{for } \rho < 1 \tag{3.10}$$

where the radius vector ρ is given by the Tschaplygin's transformation[9]

$$\rho = [1 - \sqrt{1 - r^2}]/r \tag{3.11}$$

The appropriate boundary condition now is to be specified along the boundaries of the region—namely, the shock condition on the segment ab, the "upstream" disturbance on the arc bb_1c obtained from known information in the hyperbolic region, the wall condition on the segment ced, and the "downstream" disturbance on the arc da (see Fig. 5). Among these conditions, the one at the shock is the most complicated, for instead of dealing with one single flow parameter, one has to deal with a system of simultaneous equations stating the relationship between the flow parameters and the local shock displacement. After the elimination of the shock displacement χ, one obtains from the shock condition the following system of simultaneous equations:

$$Cp_{\bar\eta} - \bar u_{\bar\eta} = 0, \quad Bp_{\bar\eta} - \bar\eta \bar v_{\bar\eta} = 0 \tag{3.12}$$

where $\bar u$ and $\bar v$ are components of the perturbed velocity along the coordinate axes $\bar\xi$ and $\bar\eta$, respectively. With the aid of the governing equations themselves a single equation for the perturbed pressure now can be derived. With reference to Fig. 3, confining our attention to values of the drift speed, C_s/A below that of Ob, the boundary conditions for the pressure perturbation can be stated as the following.

(1) On the segment ab,

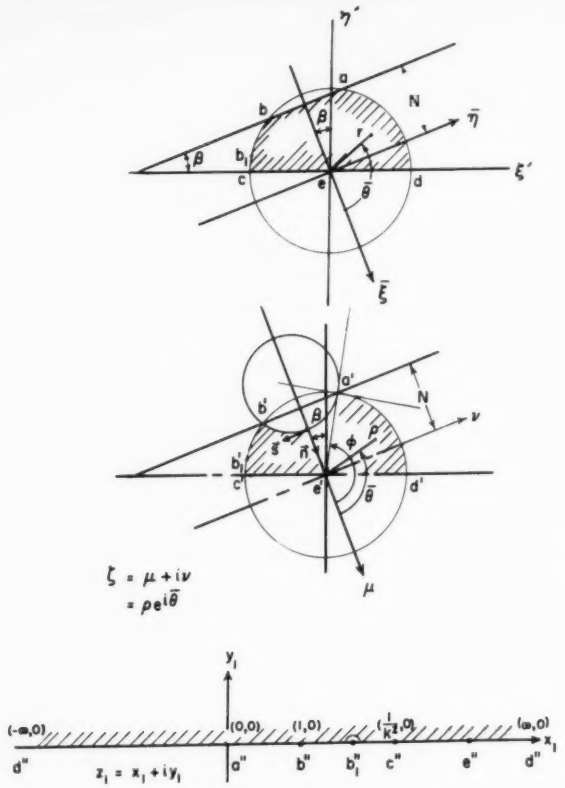

FIG. 5. Mapping of elliptic region.

$$\frac{p_{\bar{\xi}}}{p_{\bar{\eta}}} = \frac{(C - N)\bar{\eta} + (BN)/\bar{\eta}}{1 - N^2} \quad \text{for} \quad \begin{aligned} \bar{\xi} &= -N \\ \bar{\eta} &= -\,[M\cos\beta - (C_s/A)] \end{aligned} \tag{3.13}$$

(2) On the arc bb_1, $\quad p = p_3$ (3.14)

(3) On the arc b_1c, $\quad p = p_2$ (3.15)

(4) On the segment ced, $p_{\eta'} = 0$ (3.16)

(5) On the arc da, $\quad p = 0$ (3.17)

In addition, one has the compatibility conditions that the perturbed velocity $\bar{v}$ along the shock at $\bar{\eta}_b$ and at $\bar{\eta}_a$ must conform to those values obtained previously in the hyperbolic region, or from Eq. (3.12) one has

$$\int_{-\sqrt{1-N^2}}^{\sqrt{1-N^2}} (B/\bar{\eta})p_{\bar{\eta}}\, d\bar{\eta} = \int_{\bar{\eta}_b}^{\bar{\eta}_a} \bar{v}_{\bar{\eta}}\, d\bar{\eta} = -\bar{v}_3 \tag{3.18}$$

where $\bar{v}_3$ is the component along the shock of the velocity perurbation in zone (3).

According to Eq. (3.11), the domain of interest dabb$_1$ced in the $(r, \bar{\theta})$ plane is mapped into a curvilinear quadrangle d′a′b′b′$_1$c′e′d′ in the $(\rho, \bar{\theta})$ plane. The segment ab corresponding to the shock is mapped into a circular arc of a circle having radius equal to $\sqrt{(1/N^2) - 1}$ and center at $(-\sin\beta/N, \cos\beta/N)$. The Mach circle $r = 1$ is mapped into the unit circle $\rho = 1$ with points on the circumference mapped into themselves. The unit circle $\rho = 1$ intersects the circle, corresponding to the shock, orthogonally at the image points a′ and b′ of the points a and b (see Fig. 5). To proceed further analytically, it would be much more convenient to deform such a complicated domain into a somewhat simpler one. By introducing a complex variable $\zeta = \mu + i\nu = \rho e^{i\bar{\theta}}$, it can be shown that the region inside the curvilinear quadrangle in the complex ζ plane can be mapped into the upper half plane, $y_1 > 0$, in the complex $z_1 = x_1 + iy_1$ plane through the following transformation[1]

$$z_1 = \mathrm{Sn}^2\left\{ i\frac{K}{\pi} \ln\left[\frac{(1 - \alpha e^{i\phi}) - (1 - \alpha e^{i\phi})\,\zeta e^{i\phi}}{(1 + \alpha e^{i\phi}) - (1 + \alpha e^{i\phi})\,\zeta e^{i\phi}}\right]\right\} \tag{3.19}$$

where

$$\left.\begin{aligned} \phi &= \pi - \cos^{-1}(N) \\ \alpha &= \sqrt{\cos^2\beta - \sin^2\phi}/\cos(\phi + \beta) \\ K &= \int_0^1 dt/[(1 - t^2)(1 - k^2t^2)]^{1/2} \\ k &= \lambda(i \ln G/\pi) = \text{modulus of elliptic integral} \\ G &= \frac{\sqrt{\cos\beta + \sin\phi} + \sqrt{\cos\beta - \sin\phi}}{\sqrt{\cos\beta + \sin\phi} - \sqrt{\cos\beta - \sin\phi}} \end{aligned}\right\} \tag{3.20}$$

Eq. (3.19) maps the boundary of interest in the ζ plane into the real axis in the z_1 plane. The arc d′a′ is mapped into the negative half of the real axis; the arc a′b′ corresponding to the shock is mapped into the segment $0 \le x_1 \le 1$; the arc b′b′$_1$c′ is mapped into the segment $1 < x_1 \le k^{-2}$ and the segment c′e′d′ corresponding to the wall is mapped into the half line $x_1 > k^{-2}$ (Fig. 5). For a fixed shock angle β, the modulus k can be shown as a function of the shock strength, p_m/p_{1m}. Result of calculation shows that for $\beta = 30°$, and for values of shock strength p_m/p_{1m} above 2.0, up to the accuracy of four figures behind the decimal, the value of k is very close to unity.[1]

Following a method used by Lighthill,[5] the present problem can be formulated conveniently in terms of a function $F(z_1)$ defined by

$$F(z_1) = p_{y_1} + ip_{x_1} \tag{3.21}$$

The function $F(z_1)$ is regular in the upper half plane $y_1 > 0$. In accordance with the boundary conditions stated previously in the $(r, \bar{\theta})$ plane, it is also subjected to the following conditions along the real axis $y_1 = 0$.

(1) When $x_1 < 0$, $\quad F(z_1)$ is real (3.22)

(2) When $0 \le x_1 \le 1$,

$$\arg[F(z_1)] = \tan^{-1}\left\{\frac{\sqrt{\tan^2\phi\cot^2\bar{\theta} - 1}}{C_1}\right\} + \tan^{-1}\left\{\frac{\sqrt{\tan^2\phi\cot^2\bar{\theta} - 1}}{C_2}\right\} \tag{3.23}$$

where

$$\sqrt{\tan^2\phi\cot^2\bar{\theta}-1}=2\frac{(1/\alpha)\tan\{(\pi/2K)\mathrm{Sn}^{-1}(\sqrt{x_1},k)\}}{1-(1/\alpha^2)\tan^2\{(\pi/2K)\mathrm{Sn}^{-1}(\sqrt{x_1},k)\}} \tag{3.24}$$

the constants C_1 and C_2 are to be determined from

$$C_1+C_2=1/D,\quad C_1C_2=(C/D)-1 \tag{3.25}$$

C and D, in turn, are given by

$$C=\pi_{31}/\pi_{21},\quad D=-(\pi_{41}/\pi_{21})\,[N/(1-N^2)] \tag{3.26}$$

(3) When $1\le x_1<k^{-2}$,

$$F(z_1)\text{ is real} \tag{3.27}$$

(4) When $x_1>k^{-2}$,

$$F(z_1)\text{ is pure imaginary} \tag{3.28}$$

In addition, the function $F(z_1)$ is to be supplemented by the following conditions.

(5) Near the point $z_1=x_0$, the image point of b_1', at which a pressure jump occurs in the $(r,\bar{\theta})$ plane, must behave as

$$F(z_1)\sim(p_3-p_2)/\pi(z_1-x_0) \tag{3.29}$$

(6) The compatibility condition, Eq. (3.18), further requires that

$$v=\frac{B}{\sin\phi}\int_0^1\frac{1+(1/\alpha^2)\tan^2\{(\pi/2K)\mathrm{Sn}^{-1}(\sqrt{x_1},k)\}}{1-(1/\alpha^2)\tan^2\{(\pi/2K)\mathrm{Sn}^{-1}(\sqrt{x_1},k)\}}\times[\mathrm{Im}\,F(z_1)]_{y_1=0}\,dx_1 \tag{3.30}$$

With some amount of manipulation, it can be shown that the first four conditions are satisfied by a function[1]

$$H(z_1)=f_1(z_1)f_2(z_1)\,(k^{-2}-z_1)^{-(1/2)}$$

where

$$f_1(z_1)=\left[C_1+2i\frac{(1/\alpha)\tan\{(\pi/2K)\mathrm{Sn}^{-1}(\sqrt{z_1},k)\}}{1-(1/\alpha^2)\tan^2\{(\pi/2K)\mathrm{Sn}^{-1}(\sqrt{z_1},k)\}}\right]\times\left[C_2+2i\frac{(1/\alpha)\tan\{(\pi/2K)\mathrm{Sn}^{-1}(\sqrt{z_1},k)\}}{1-(1/\alpha^2)\tan^2\{(\pi/2K)\mathrm{Sn}^{-1}(\sqrt{z_1},k)\}}\right] \tag{3.31}$$

and

$$f_2(z_1)=\exp\left\{-\frac{i}{\pi}\int_{1/k^2}^{\infty}\frac{[e^{i\alpha\tan^{-1}(x_1)}]-[(z_1-i)/(z_1+i)]}{[e^{i\alpha\tan^{-1}(x_1)}]+[(z_1-i)/(z_1+i)]}\times\frac{g(x_1)}{1+x_1^2}\,dx_1\right\}$$

where $g(x_1)=\arg[f_1(z_1)]$ on $x_1>1/k^2$

In view of the remaining conditions, our required function, as can be verified, is given by

$$F(z_1)=D_1[D_2(z_1-x_0)-1]\,H(z_1)/(z_1-x_0) \tag{3.32}$$

The two constants, D_1 and D_2, are to be determined from the remaining conditions stipulated by (5) and (6), respectively.

(4) Conclusion

By considering the shock as originated at the concave corner of a wall, and the discontinuity front of an upstream temperature jump as inclined at an angle to the upstream main flow velocity, a problem of unsteady interaction between a thermal layer and a plane oblique shock is studied. It is found that under such a condition, even for weak upstream disturbance, mixed flow generally occurs in the region downstream of the shock—namely, a hyperbolic region outside a sonic circle and an elliptic region inside the sonic circle. Based on the general concept of conical flow, the downstream perturbed flow caused by the interaction is examined qualitatively at first. Subsequently, a method for quantitative investigation of the downstream flow field is formulated. Analytically, this is accomplished by formulating a single governing equation for the pressure perturbation alone. This equation, then, is shown to be reducible to a simple wave equation for the hyperbolic region, and to a Laplace equation for the elliptic region.

For the flow in the hyperbolic region, the solution is started by assuming that the region near the foot of the shock is the same as that corresponding to a steady flow; using the concept of constant states, solutions for adjacent regions were obtained by the method of characteristics. For the flow in the elliptic region, the solution is effected by using the method of conformal mappings after a Tschaplygin's transformation. The domain of interest is finally mapped into a half plane. Due to the topological equivalence of the region to a rectangle, the mapping function involves an elliptic integral. The modulus occurring in the elliptic function is shown to be related to the shock strength and is found to be very close to unity for fairly strong shocks. Finally, following a procedure of Lighthill, the solution for the pressure perturbation is obtained.

References

[1] Chang, C. T., *On the Interaction of Weak Disturbances and a Plane Shock of Arbitrary Strength in a Perfect Gas*, Dissertation, The Johns Hopkins University, 1955.

[2] Griffith, Wayland C., *Interaction of a Shock Wave with a Thermal Boundary Layer*, Journal of the Aeronautical Sciences, Vol. 23, No. 1, pp. 16–22, January, 1956.

[3] Hess, Robert V., *Interaction of Moving Shocks and Hot Layers*, NACA TN 4002, May, 1957.

[4] Busemann, A., *Infinitesimale Keglige Überschallströmung*, Jahrbuch der Luftfahrtforschung, 7B No. 3, pp. 105–121, 1943 (English Trans. NACA TM 1100, 1947).

[5] Lighthill, M. J., *The Diffraction of Blast*, I, Proc. Roy. Soc. (London) Series A, Vol. 198, pp. 454–470, 1949.

[6] Chang, C. T., *Interaction of a Plane Shock and Oblique Plane Disturbances with Special Reference to Entropy Waves*, Journal of the Aeronautical Sciences, Vol. 24, No. 9, pp. 675–682, September, 1957.

[7] Courant, R., and Friedrichs, K. O., *Supersonic Flow and Shock Waves;* Interscience Publishers, New York and London, 1948.

[8] Goldstein, S., and Ward, G. N., *Linearized Theory of Conical Field in Supersonic Flow with Application to Plane Aerofoils*, The Aeronautical Quarterly, Vol. II, Part I, pp. 39–84, 1950.

[9] Lagerstrom, P. A., *Linearized Supersonic Theory of Conical Wings*, NACA TN 1685, 1950.

Experimental Investigation of the Aerodynamics of a Wing in a Slipstream†

MARC E. BRENCKMANN*

Institute of Aerophysics, University of Toronto

SUMMARY

An experimental study of a wing in a propeller slipstream was made in order to determine the spanwise distribution of the lift increase due to slipstream at different angles of attack of the wing and at different free stream to slipstream velocity ratios. The results were intended in part as an evaluation basis for different theoretical treatments of this problem.

The comparative span loading curves, together with supporting evidence, showed that a substantial part of the lift increment produced by the slipstream was due to a "destalling" or boundary-layer-control effect. The integrated remaining lift increment, after subtracting this destalling lift, was found to agree well with a potential flow theory.

An empirical evaluation of the destalling effects was made for the specific configuration of the experiment.

SYMBOLS

S	= area of wing immersed in slipstream
R	= propeller radius
c	= wing chord
y	= spanwise coordinate, origin at midspan
L	= total wing lift
ΔL	= total lift increase due to slipstream
ΔL_p	= direct lift increase due to slipstream
C_L	= wing lift coefficient in uniform flow (nondimensionalized with free-stream q_0)
$(\Delta C_L)_{\text{ind.}}$	= additional wing lift coefficient due to indirect slipstream influence (nondimensionalized with free-stream q_0)
c_l	= local lift coefficient (nondimensionalized with free-stream q_0)
$\hat{c}_l$	= local lift coefficient (nondimensionalized with "average" $\hat{q}$)
l	= local lift per unit span
q_0	= dynamic pressure in free stream
q_j	= local dynamic pressure in slipstream
$\bar{q}_j$	= equivalent dynamic pressure of slipstream
Δq	= equivalent dynamic pressure increment of slipstream
$\hat{q}$	= $[(\bar{q}_j + q_0)/2]$, "average" dynamic pressure
T	= slipstream thrust
σ	= $(\bar{q}_j - q_0)/(\bar{q}_j + q_0)$ slipstream strength parameter
λ	= empirical factor
α	= angle of attack of the wing
β	= angle of rotation in slipstream
X	= $\sqrt{\bar{q}_j/q_0}$

INTRODUCTION

INTEREST in STOL aircraft configurations has put new emphasis on propeller slipstream deflection as a means of creating lift at low forward velocities. Past experiments on this subject are not systematic from this new point of view, mainly because they were conducted for other purposes. In fact, only two papers[1, 6] are usually cited when experimental values are compared with theoretical results. On the other hand, the earlier theories[1, 5] are known to be inadequate for practical configurations and the validity of recent theories[2, 3, 4] is not definitely established.

The investigation reported here was intended to supply experimental data in the form of the spanwise lift distribution of a straight wing in a propeller slipstream for various angles of attack and for various free stream to slipstream velocity ratios. The present paper is an abridged version of UTIA Technical Note No. 11.[7]

EXPERIMENT

The measurements were conducted in the UTIA 32 by 48 in. low-speed wind tunnel, using a free-stream speed variation from zero to approximately 100 ft./sec.

A wing of constant chord of 8 in. and of constant profile (NACA64A418) was designed to span the tunnel over 32 in. from wall to wall. It was composed of 19 narrow sections independently springmounted on a common spar. Each spring was straingaged so as to allow measurement of the lift at each section. Aerodynamic continuity was obtained by means of a thin elastic skin wrapped around the wing, sealing the gaps between the sections but transmitting very little force from one section to another. The wallmountings of the spar formed pivots for the variation of angle of attack at the 1/4 chord line.

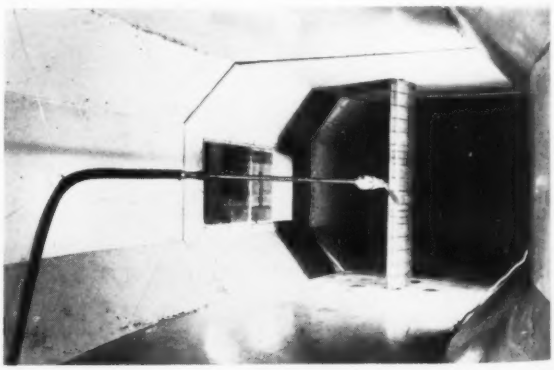

FIG. 1. Downstream view of the apparatus in the wind tunnel.

Received September 30, 1957.

† This research was carried out under the supervision of Dr. G. K. Korbacher and Dr. H. S. Ribner, with the support of The DeHavilland Aircraft of Canada Limited, while the author was on a leave of absence.

* Now at The DeHavilland Aircraft of Canada Limited.

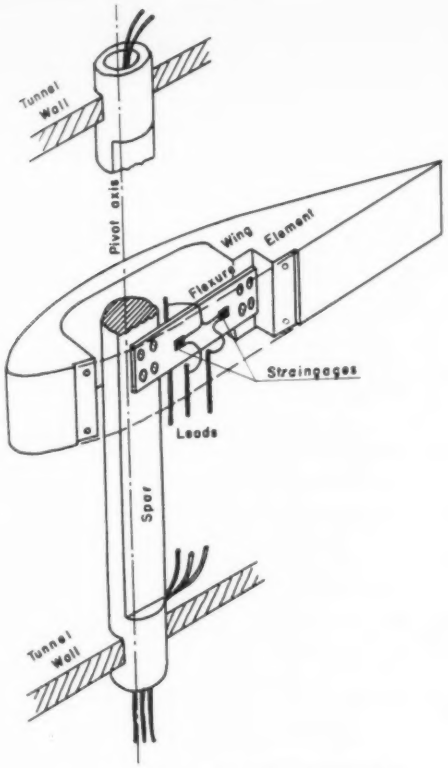

FIG. 2. Sketch of the wing construction.

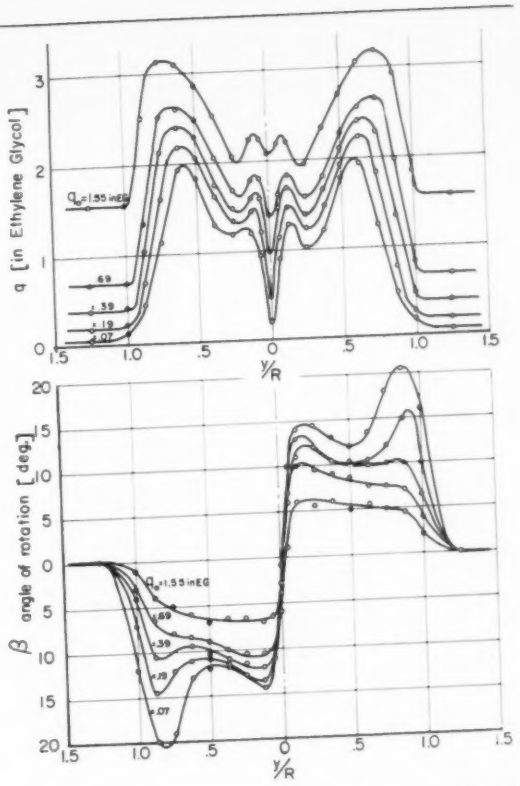

FIG. 3. Slipstream cross sections, dynamic pressure and rotation angle.

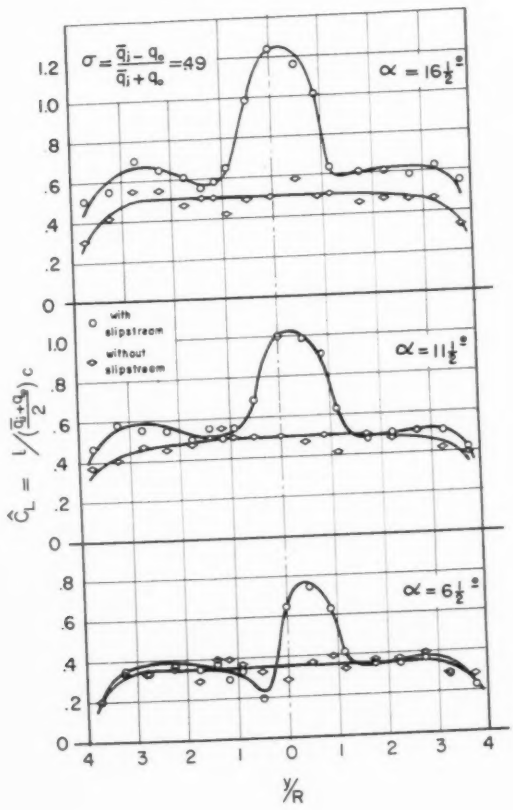

FIG. 4(a). Spanwise lift distribution, $\sigma = 0.49$.

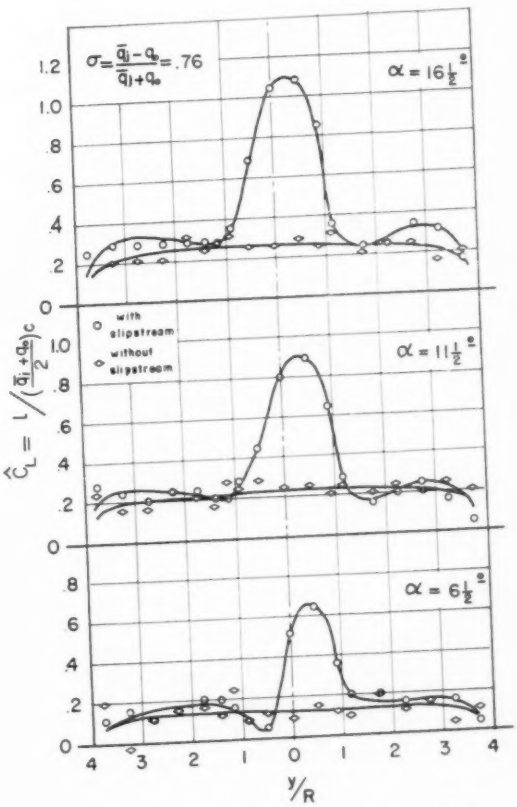

FIG. 4(b). Spanwise lift distribution, $\sigma = 0.76$.

The slipstream was produced by an 8-in. diameter propeller driven at 13,000 r.p.m. by a 1/2-hp. pneumatic motor which was suspended independently upstream of the wing in a pusher configuration.

The variation of the free stream to slipstream velocity ratio was achieved by varying the tunnel speed and keeping the air pressure for the pneumatic motor constant. The experimental layout is shown in Fig. 1 and the construction of the wing in Fig. 2.

Test runs were made for five tunnel speeds at three angles of attack with and without slipstream. Fig. 3 shows the slipstream cross sections in dynamic pressure and helix angle for the different runs.

Reduction of Results

The curves of Fig. 3 showed that the slipstream velocity cross section was far from the ideal case of a step increment above freestream velocity. An equivalent step increment was therefore defined as:

$$\overline{\Delta q} = (1/R^2) \int_0^R 2\, y\, (q_j - q_0)\, dy$$

In order to reduce the lift distribution to nondimensional form, a reference quantity was chosen which does not disappear for either of the extreme cases of uniform flow or of static jet; this was termed the "average" dynamic pressure $\hat{q}$ defined as

$$\hat{q} = (q_0 + \bar{q}_j)/2 \quad \text{with} \quad \bar{q}_j = q_0 + \overline{\Delta q}$$

Thus, when $\bar{q}_j \to q_0$ (uniform flow), $\hat{q} \to q_0$, and when $q_0 \to 0$ (static jet), $\hat{q} \to \bar{q}_j/2$.

The nondimensional quantities used in the presentation of the spanwise lift distribution are then

local lift coefficient $\quad \hat{c}_L = l/\hat{q}c$

slipstream strength parameter

$$\sigma = (\bar{q}_j - q_0)/(\bar{q}_j + q_0) = \overline{\Delta q}/2\hat{q}$$

This particular parameter σ arises naturally in the theoretical formulation of reference 4. The results of slender body theory applied to this problem are also expressed most simply as a function of σ. The more common coefficient $c_L = l/q_0 c$ is easily calculated from those defined above as

$$c_L = \hat{c}_L/(1 - \sigma)$$

The total lift increase due to the slipstream was obtained as

$$\Delta L = \int_{\text{span}} (l_{\text{with slipstream}} - l_{\text{without slipstream}})\, dy$$

The slipstream thrust was obtained as

$$T = 4\pi \int_0^R \left(q_j - \sqrt{q_j q_0}\right) y\, dy$$

Total lift increase values were rendered nondimensional in the forms

$$\Delta L/\alpha T, \quad \Delta L/2\pi\alpha S\overline{\Delta q}, \quad \Delta L_p/\alpha T, \quad \Delta L_p/2\pi\alpha S\overline{\Delta q}$$

as explained in the discussion of the results.

Results and Discussion

(a) *Lift Distribution*

Figs. 4(a) and 4(b) illustrate the spanwise distribution of lift as $\hat{c}_L$ versus y/R curves for different σ. It can be seen that:

(1) the rotation of the slipstream causes the lift increase to be shifted towards the side of the wing which is in the propeller upwash. This influence diminishes with higher wing incidence and seems compensative in overall effect.

(2) the limits of the direct slipstream influence are sharply defined and do not vary with α or σ. The present configuration did not cause any appreciable spread of the slipstream.

(3) the lift distribution outside of the slipstream shows a marked increase relative to the corresponding case without slipstream, especially for high wing incidence. This increase extends up to close to the tunnel walls, where the tunnel boundary layer renders the readings uncertain. This phenomenon suggests some flow modification over the whole wing which delays the stall; the evidence is developed in the following section.

(b) *Slipstream Destalling Effect*

Fig. 5(a) illustrates the lift characteristic of the wing at its midspan section in uniform flow at the various Reynolds Numbers encountered in the free stream during the test runs. Fig. 5(b) shows the lift characteristic of the wing at a section outside of the slipstream in flow with and without slipstream. Fig. 6 shows the chordwise shifting of the center of pressure with angle of attack at sections inside and outside of the slipstream boundary for uniform flow and for flow with slipstream.

These curves show the improved stalling behavior of the wing in the flow with slipstream. The progressive flow separation at the trailing edge which is normally taking place at angles of attack above 10° is delayed up to angles above 15°, the most probable cause being boundary-layer suction exerted both by the low-pressure region in the slipstream above the wing and by the jet pump action of the mixing region in the slipstream boundary.

(c) *Total Lift Gain Due to Slipstream*

In order to evaluate the overall slipstream effect, the total lift increase ΔL is presented:

(1) as $\Delta L/\alpha T$ versus σ (dotted lines in Fig. 7). This quantity can be termed slipstream turning effectiveness of the wing. The value unity signifies that ΔL has arisen from a turning of the thrust vector through an angle equal to the angle of attack. It can be seen, however, that curves for different α do not coincide, and ΔL is nonlinear with α and σ.

(2) as $\Delta L/2\pi\alpha S\overline{\Delta q}$ versus σ (dotted lines in Fig. 8).

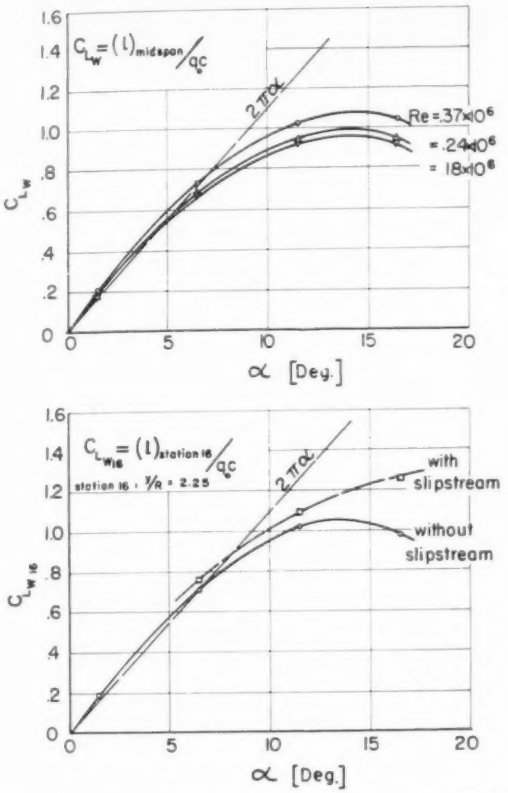

FIG. 5. (a) *Top.* Local lift coefficients in uniform flow at midspan. (b) *Bottom.* Local lift coefficients in flow with and without slipstream, outside of the slipstream.

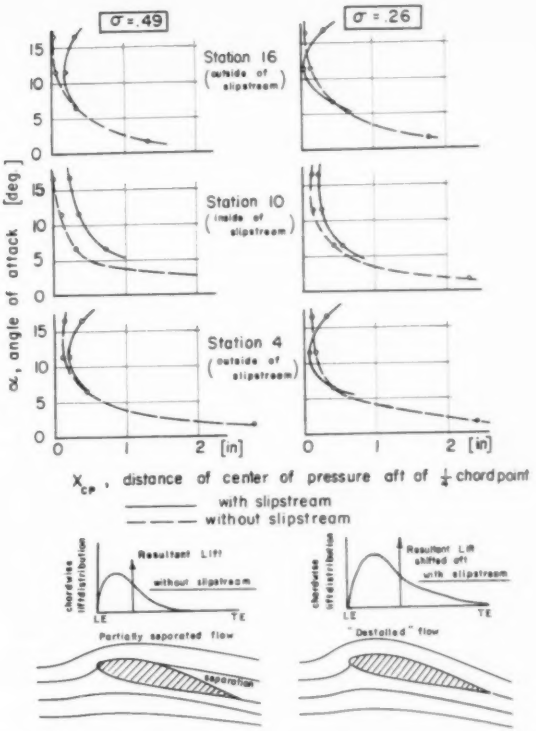

FIG. 6. Variation of the position of the center of pressure with angle of attack for flow with and without slipstream at different spanwise stations.

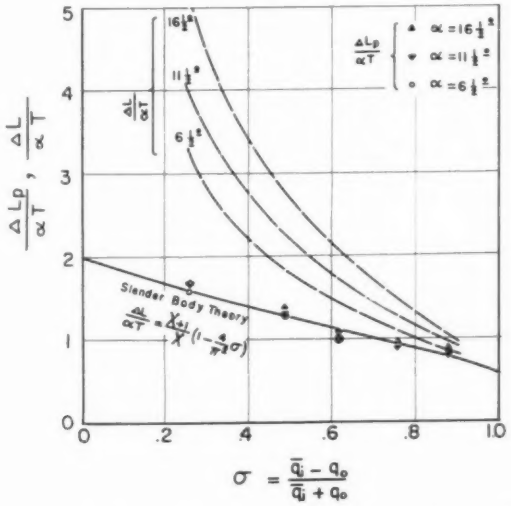
$\frac{\Delta L_p}{\alpha T}$, $\frac{\Delta L}{\alpha T}$
$\frac{\Delta L_p}{\alpha T}$ α = 16½°
α = 11½°
α = 6½°
$\frac{\Delta L}{\alpha T}$
Slender Body Theory
$\frac{\Delta L}{\alpha T} = \frac{\chi_{\sigma 1}}{\chi}(1 - \frac{\sigma}{\pi\lambda}\sigma)$
$\sigma = \frac{\bar{q}_j - q_o}{\bar{q}_j + q_o}$

FIG. 7. Total and "potential flow" lift increase due to slipstream, nondimensionalized with αT.

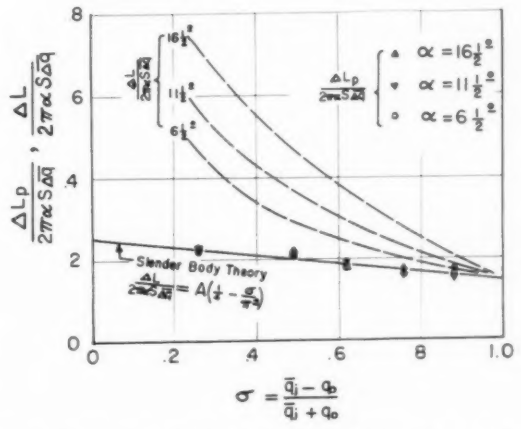
$\frac{\Delta L_p}{2\pi\alpha S\Delta q}$, $\frac{\Delta L}{2\pi\alpha S\Delta q}$
$\frac{\Delta L_p}{2\pi\alpha S\Delta q}$ α = 16½°
α = 11½°
α = 6½°
$\frac{\Delta L}{2\pi\alpha S\Delta q}$
Slender Body Theory
$\frac{\Delta L}{2\pi\alpha S\Delta q} = A(\frac{1}{2} - \frac{\sigma}{\pi\lambda})$
$\sigma = \frac{\bar{q}_j - q_o}{\bar{q}_j + q_o}$

FIG. 8. Total and "potential flow" lift increase due to slipstream, nondimensionalized with $2\pi\alpha\ S\ \Delta q$.

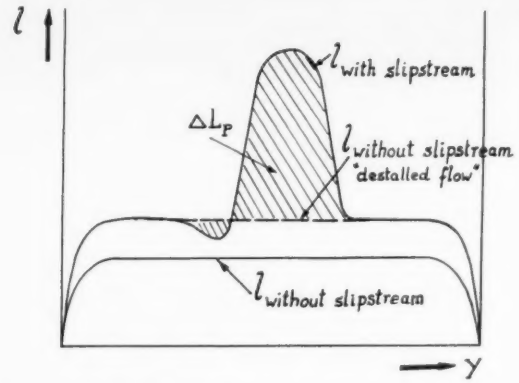

FIG. 9. Graphical estimation of the destalling effect.

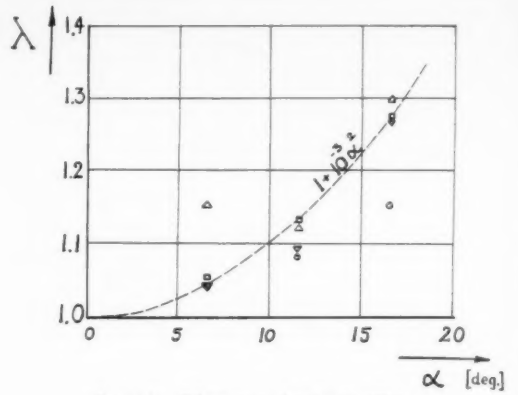

FIG. 10. Slipstream destalling effect.

Here $2\pi\alpha S\overline{\Delta q}$ represents the lift increase according to simple strip theory without induction effects. The general shape of the curves is the same as for those under (1) above, the nonlinearity with α being somewhat less pronounced.

Comparison of both representations with a closed form solution given by slender body theory (adapted from reference 2) shows good agreement only for σ near unity (static jet).

(d) Direct Lift Gain Due to Slipstream

In order to separate the lift due to boundary-layer modification from the total lift increase, the quantity ΔL_p is introduced* as

$$\Delta L_p = \int_{\text{span}} \left(l_{\text{with slipstream}} - l_{\substack{\text{without slipstream} \\ \text{"destalled flow"}}} \right) dy$$

as illustrated in Fig. 9. Thus, ΔL_p is an approximation of the lift increase as it should be predicted by potential flow theory. For comparison ΔL_p is represented in the same forms as ΔL in Figs. 7 and 8. It is seen that (1) $\Delta L_p / \alpha T$ and $\Delta L_p / 2\pi\alpha S\overline{\Delta q}$ are independent of the angle of attack α, and (2) both sets of values agree very well with the solutions given by slender body theory.

(e) Indirect Lift Gain Due to Slipstream

Having correlated the direct influence of the slipstream with potential flow theory, an attempt was made to formulate the indirect influence empirically. The c_L versus α characteristic of the wing was known to be modified by the slipstream to yield higher $c_{L\,max}$ at higher α. Therefore, λ was defined as a distortion factor of the characteristic as

$$\lambda = [C_L + (\Delta C_L)_{\text{destalling}}] / C_L = \int l_{\substack{\text{without slipstream} \\ \text{"destalled flow"}}} dy \Big/ \int l_{\text{without slipstream}}\, dy$$

This factor λ plotted versus α for different σ is shown in Fig. 10. The relation

$$\lambda = 1 + 10^{-3}\alpha^2$$

is shown to be a close approximation of the experimental results for the configuration investigated, indicating that λ is independent of σ for $\sigma \geq 0.25$.

CONCLUSIONS

The slipstream velocity profile, rotation, and deformation are concluded to be of secondary importance.

The total added lift due to the passage of a slipstream over a wing appears to consist of two parts: (a) a direct "potential flow lift" that is a function of slipstream strength, and (b) an indirect "destalling lift" of comparable magnitude that is sensibly independent of slipstream strength above some threshold value.

For the present configuration it was possible to correlate the potential flow lift with an existing slender body theory and to approximate the destalling lift by an empirical function of angle of attack.

The controlled use of the slipstream velocity to energize the boundary layer would appear to be attractive. Since destalling effects will depend on the wing configuration, its stalling behavior, the Reynolds Number, etc., the indirect lift gain obtainable in STOL applications will have to be studied for optimization on the specific configuration considered.

* Dr. H. S. Ribner suggested the idea of subtracting the destalled lift and correlating ΔL_p with slender body theory.

REFERENCES

[1] Durand, W. F., (Ed.), *Aerodynamic Theory*, Vol. IV, Koning C., "Influence of the Propeller on Other Parts of the Airplane Structure," Julius Springer, Berlin, 1935.

[2] Graham, E. W., Lagerstrom, P. A., Licher, R. M., and Beane, B. J., *A Preliminary Theoretical Investigation of the Effects of Propeller Slipstream on Wing Lift*, Report No. SM-14991, Douglas Aircraft Co., Santa Monica Division, November, 1953.

[3] Rethorst, S., *Lift on a Wing in a Propeller Slipstream as Related to Low-Speed Flight*, Aeronautical Engineering Review, Vol. 15, No. 10, pp. 42–48, October, 1956.

[4] Ribner, H. S., *Theory of Wings in Slipstreams*, Unpublished Report, DeHavilland Aircraft of Canada Ltd., March, 1957.

[5] Smelt, R., and Davies, H., *Estimation of Increase in Lift Due to Slipstream*, British ARC, R&M 1788, 1937.

[6] Stuper, J., *Einfluss des Schraubenstrahls auf Flügel und Leitwerk*, Luftfahrtforschung, Vol. 15, No. 4, 1938; translated as NACA TM 874.

[7] Brenckmann, M. E., *Experimental Investigation of the Aerodynamics of a Wing in a Slipstream*, UTIA Tech. Note 11, April, 1957.

Readers' Forum

BRIEF REPORTS of investigations in the aeronautical sciences and discussions of papers published in the JOURNAL are presented in this special department. Entries must be restricted to a maximum of 1,300 words or the equivalent of one JOURNAL page including formulas and illustrations. Publication is completed as soon as possible after receipt of the material. The Editorial Committee does not hold itself responsible for the opinions expressed by the correspondents.

Contents

A Vectorial Representation of Aerodynamic Forces Acting on a Thin Rectangular Wing Oscillating Harmonically in Supersonic Potential Flow ..... JAGANNATH P. CHAWLA 329

Note on Ballistic Trajectories and Orbits ..... RICHARD F. HUGHES 330

Flow Against a Vertical Plate With Small Suction ..... J. R. FOOTE 331

Hydromagnetic Effects on Stagnation-Point Heat Transfer ..... JOSEPH L. NEURINGER AND WILLIAM MCILROY 332

Magnetohydrodynamic Analysis of Heat Transfer Near a Stagnation Point ..... VERNON J. ROSSOW 334

Space-Time Correlations of the Fluctuating Wall Pressure in a Turbulent Boundary Layer ..... W. W. WILLMARTH 335

Blunt Body Separation at Supersonic Speeds ..... PAUL F. BRINICH 336

Some Solutions of the Navier-Stokes Equations With Time Dependent Density ..... ROGER D. SULLIVAN AND COLEMAN DUP. DONALDSON 337

On the Character of the Instability of the Laminar Boundary Layer Near the Nose of a Blunt Body ..... A. M. KUETHE 338

Relative Importance of Free-Stream Vorticity and Self-Induced Pressure Gradient on a Flat-Plate Boundary Layer ..... HAROLD MIRELS 339

One-Dimensional Transient Heat Flow in a Multilayer Slab ..... W. F. CAMPBELL 340

Asymmetric Starting for Hypersonic Wind Tunnels ..... ROBERT H. JOHNSON 341

Note on "Stability Equations for Conical Shells" ..... PAUL SEIDE 342

Application of the Witte Rearranging Method to a Typical Structural Matrix ..... BERTRAM KLEIN 342

The Conservation Equations for Multicomponent Gas Mixtures in Arbitrary Coordinate Systems ..... F. A. WILLIAMS 343

A Vectorial Representation of Aerodynamic Forces Acting on a Thin Rectangular Wing Oscillating Harmonically in Supersonic Potential Flow*

Jagannath P. Chawla

Aerodynamics Department, Systems Development Laboratories, Hughes Aircraft Company, Culver City, Calif.

January 2, 1958

A METHOD of representing aerodynamic lift and moment acting on a thin rectangular wing oscillating harmonically in supersonic potential flow is indicated. This may help the practicing flutter engineer gain a better understanding of the nature of aerodynamic forces exciting the structure. This representation should also prove useful for (a) solution of flutter determinant by vector methods, (b) flutter studies by analog methods, (c) correlation with lift and moment of oscillating airfoils measured in a wind tunnel, (d) dynamic testing of structures, and (e) flight testing for flutter.

The section lift and moment acting on the airfoil may be expressed as follows:

$$L = 2\rho c V^2 k^2 \{(L_1 + iL_2)[h/(c/2)] + (L_3 + iL_4)\alpha\} \quad (1)$$

$$M = -\rho c^2 V^2 k^2 \{(M_1 + iM_2)[h/(c/2)] + (M_3 + iM_4)\alpha\} \quad (2)$$

Defining $\alpha_h = \dot{h}/V = ikh/(c/2)$, the sectional coefficients become

$$c_l = L/(1/2)\rho V^2 c = 4k(L_2 - iL_1)\alpha_h + 4k^2(L_3 + iL_4)\alpha \quad (3)$$

$$c_m = M/(1/2)\rho V^2 c^2 = -2k(M_2 - iM_1)\alpha_h - 2k^2(M_3 + iM_4)\alpha \quad (4)$$

* The author is grateful to the Hughes Aircraft Company for permission to publish this note, and should like to express his appreciation to his colleague, Dr. William M. Bleakney, for helpful discussions.

Contributors Please Note

Readers' Forum items must be confined to the equivalent of one page in the *Journal*. Contributions that exceed this limit will be returned to the authors for condensation and rewrite. To avoid inconvenience and delay, please adhere to the following specifications:

(1) Five, double-spaced, typewritten, manuscript pages (8½ by 11 in.), including wide margins, formulas, and headings equal one printed page.

(2) For every illustration, deduct at least one-half or as much as one manuscript page, depending on the size of the illustration.

With $(\partial c_l/\partial\alpha)_{k=0} = 4/\beta$, we can write

$$c_{l_{\alpha_h}}/(c_{l_\alpha})_{k=0} = k\beta(L_2 - iL_1) \tag{5}$$

$$c_{l_\alpha}/(c_{l_\alpha})_{k=0} = k^2\beta(L_3 + iL_4) \tag{6}$$

$$c_{m_{\alpha_h}}/(c_{l_\alpha})_{k=0} = -(1/2)\,k\beta(M_2 - iM_1) \tag{7}$$

$$c_{m_\alpha}/(c_{l_\alpha})_{k=0} = -(1/2)\,k^2\beta\,(M_3 + iM_4) \tag{8}$$

The right-hand sides of these equations may be written as $Ae^{i\phi}$. Hence, the amplitude and phase of the lift vector at any frequency are known in terms of their values at zero frequency; also, the magnitude and phase of the moment vector are known in relation to the lift vector at a prescribed frequency of oscillation and Mach Number.

Plots of Eqs. (5) to (8), based on the results of linear theory (see reference 1) and for the axis of pitch at mid-chord, are shown in Figs. 1 to 4.

Figs. 1 and 2 show that the lift vector lies in the right half plane for all values of k and M. Its amplitude decreases monotonically with k, for values of k of practical interest in flutter work. The deviations in phase and amplitude from the steady-state value decrease as Mach Number is increased.

Fig. 3 shows that for mid-chord location of the axis of pitch, the moment vector due to vertical translation leads the vertical velocity $\dot{h}$ by 90° for small values of k and lies in the upper half plane for values of k or $\{\bar{\omega} = [2kM^2/(M^2 - 1)]\}$ of practical interest.

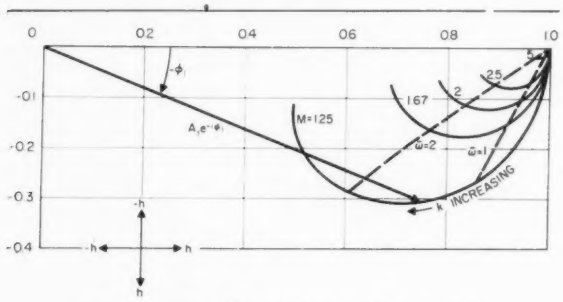

FIG. 1. $(\partial c_l/\partial\alpha_h)/(\partial c_l/\partial\alpha)_{k=0} = k\beta(L_2 - iL_1)$.

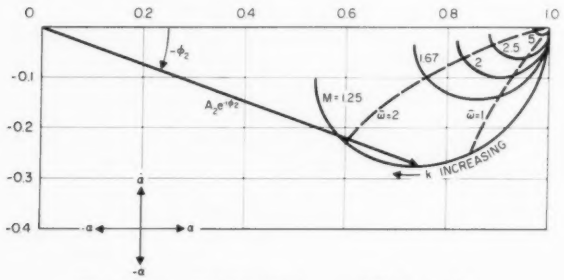

FIG. 2. $(\partial c_l/\partial\alpha)/(\partial c_l/\partial\alpha)_{k=0} = k^2\beta(L_3 + iL_4)$.

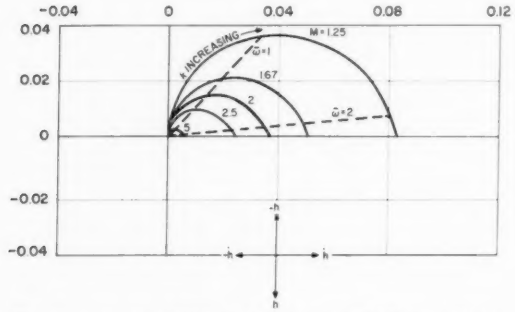

FIG. 3. $(\partial c_m/\partial\alpha_h)/(\partial c_l/\partial\alpha)_{k=0} = -(1/2)k\beta(M_2 - iM_1)$.

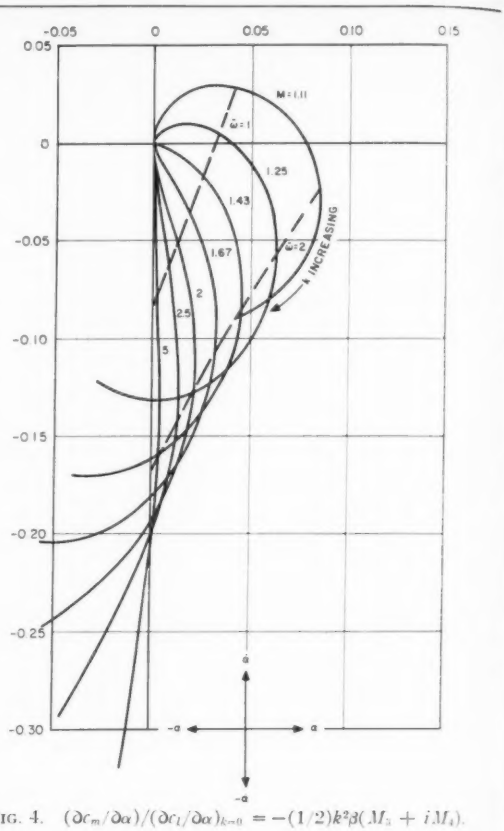

FIG. 4. $(\partial c_m/\partial\alpha)/(\partial c_l/\partial\alpha)_{k=0} = -(1/2)k^2\beta(M_3 + iM_4)$.

Fig. 4 shows that for low supersonic Mach Numbers the moment vector leads the angular displacement vector α by 90° for small values of k. As Mach Number is increased, lead angle decreases changing to a lag angle. The limiting value of the lag angle for $M^2 \gg 1$ is 90°. Another noteworthy observation is that for $M^2 \gg 1$ amplitude of the moment vector increases linearly with frequency of oscillation. Position of the moment vector in the upper half plane, that is, with a lead angle of 0° to 180°, is indicative of instability in pitch.

Curves of a similar nature can be drawn for other locations of the axis of pitch. For rectangular wings of finite aspect ratio, similar plots may be prepared with values of lift and moment integrated over the span, including the effect of pertinent mode shapes considered in the flutter analysis.

REFERENCE

[1] Garrick, I. E., and Rubinow, S. I., *Flutter and Oscillating Air-Force Calculations for an Airfoil in a Two-Dimensional Supersonic Flow*, NACA TR 846, May, 1946.

Note on Ballistic Trajectories and Orbits

Richard F. Hughes
Vice President, K & H Engineering Company, Toledo, Ohio
January 14, 1958

THE PATH of a particle moving in the earth's gravitational field (see Fig. 1) is an ellipse which may be described as follows:

$$\frac{r}{r_0} = \frac{\gamma \sin^2\alpha}{1 - \sqrt{1 - (2 - \gamma)\gamma \sin^2\alpha \sin\theta}} \tag{1}$$

(see reference 1) where

γ = $(V_0^2/gR_0)(r_0/R_0)$
α = attitude of particle motion with respect to radial direction at location r_0, θ_0
r, θ = coordinates of path
V_0 = particle velocity at location r_0, θ_0
R_0 = the earth's radius
g = gravitational acceleration at the earth's surface

Characteristics of the particle motion are readily discernible from an inspection of the form of relation (1). The maximum and minimum distances of the path from earth's center are given by the $+1$ and -1 values of $\sin\theta$, respectively.

$$\frac{r_{max\ or\ min}}{r_0} = \frac{\gamma \sin^2\alpha}{1 \mp \sqrt{1 - (2-\gamma)\gamma \sin^2\alpha}} \tag{2}$$

Relation (2) indicates that the conditions necessary for the particle to move in an orbital path about the earth are (a) $\gamma < 2$, i.e., $V_0^2/gR_0 < 2R_0/r_0$, the escape velocity condition, and (b) $R_0/r_0 < r_{min}/r_0$.

Condition (b) may be restated as a lower limit for the value of γ by inserting R_0 for r minimum in relation (2) and solving for γ. Thus the inequality which must be satisfied for an earth satellite is

$$2 > \gamma > \frac{2(r_0/R_0 - 1)}{r_0^2 \sin^2\alpha/R_0^2 - 1} \tag{3}$$

where $$\sin^2\alpha > R_0/r_0$$

The restriction on α is required to satisfy condition (b) for values of γ less than 2. The minimum particle velocity which will produce an orbital path is given by α equal $\pi/2$.

$$(V_0^2/gR_0)_{min} = 2/(r_0/R_0 + 1)(r_0/R_0) \tag{4}$$

This orbit would measure a minimum distance of R_0 and a maximum distance of r_0 from the earth's center. If the path is everywhere relatively near the earth's surface ($r_0/R_0 \backsimeq 1$), the minimum required orbital velocity becomes the familiar $\sqrt{gR_0}$.

Relation (1) may also be used to examine the ballistic trajectory of a particle moving between two points on the earth's surface. The trajectory range, distance traveled measured along the earth's surface, may be determined from

$$\text{range} = 2R_0(\theta\ @\ r_{max} - \theta_0)$$

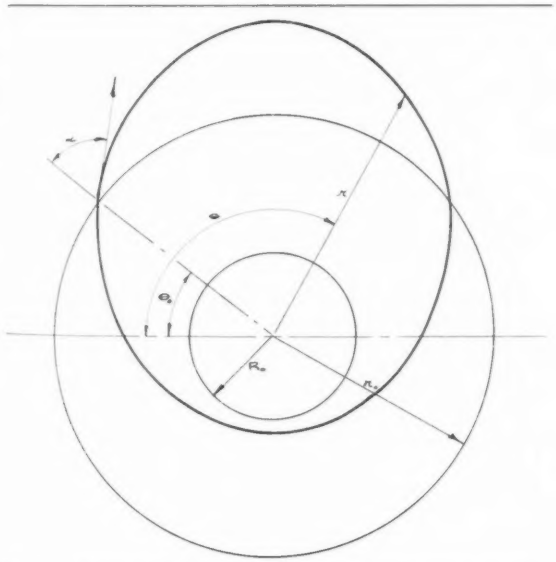

FIG. 1. Orbital path of a particle moving in the earth's gravitational field.

where R_0 has been set equal to r_0. θ @ r_{max} from relation (1) is $\pi/2$. θ_0 is the coordinate angle for $r/r_0 = 1$.

$$\therefore \text{range} = 2R_0(\pi/2 - \theta_0) = 2R_0 \cos^{-1}\sin\theta_0$$

and

$$\text{range} = 2R_0 \cos^{-1}\frac{1 - \gamma\sin^2\alpha}{+\sqrt{1 - (2-\gamma)\gamma\sin^2\alpha}} \tag{5}$$

For a fixed value of γ, the value of α which maximizes range is

$$\alpha_{opt} = \sin^{-1}(1/\sqrt{2-\gamma}) \tag{6}$$

$$\text{max. range} = 2R_0 \cos^{-1}[2\sqrt{1-\gamma}/(2-\gamma)] \tag{7}$$

and

$$r_{max}/R_0\ @\ \text{max. range} = \gamma/(2-\gamma)(1 - \sqrt{1-\gamma}) \tag{8}$$

For $0 < \gamma < 1$, optimum α varies between $\pi/4$ and $\pi/2$ and maximum range varies between 0 and πR_0.

The maximum altitude attained by a particle directed straight outward from the earth may be obtained from relation (2) by allowing $\alpha \to 0$.

$$r_{max}/R_0\ (\text{for } \alpha = 0) = 1/(1 - \gamma/2) \tag{9}$$

REFERENCE

[1] Kooy, J. M. J., and Uytenbogaart, J. W. H., *Ballistics of the Future*, pp. 147, 157, McGraw-Hill Book Company, Inc., New York, 1946.

Flow Against a Vertical Plate with Small Suction*

J. R. Foote
Professor, Division of Engineering Sciences, Purdue University, Lafayette, Ind.

January 14, 1958

IT IS WELL KNOWN that the complete Navier-Stokes equations for boundary-type flow can be solved for the case of a stagnation point in plane steady flow. Here that problem is contained as a special case of flow having wall suction, typified by flow through porous cloth. The simplest effect of porosity is to alter a boundary condition without affecting the differential equation.

In the notation of reference 1 the equation and boundary conditions are

$$\left.\begin{aligned} &\varphi''' + \varphi\varphi'' - \varphi'^2 + 1 = 0, \\ &\varphi(0) = \varphi_0 \geq 0, \quad \varphi'(0) = 0, \quad \varphi'(\infty) = 1 \end{aligned}\right\} \tag{1}$$

The independent variable is ξ, the wall is $\xi = 0$, and the suction parameter is φ_0. This mathematical problem is related to the physical problem through

$$u = -A\varphi(\xi), \quad v = A\alpha y\,\varphi'(\xi),$$

$$\xi = \alpha x, \quad \alpha = \sqrt{a/\nu}, \quad A = \sqrt{\nu a}$$

At large distances, $u = -ax$, $v = ay$, which give the meaning of the parameter a. At the wall,

$$u = -u_0, \quad v = 0, \quad \varphi_0 = u_0/A$$

and φ_0 can be quite large since $A \sim \nu^{1/2}$. This fact greatly affects the possibility of quickly truncating the series form of the solution.

A series method, set forth in detail by Fettis,[2] is applied, which leads to a system of linear differential equations with forcing terms dependent on previously calculated functions. Put

* This note was written under the sponsorship of the National Science Foundation, Contract NSF-G3050, New York University. Reproduction in whole or in part is permitted for any purpose of the United States Government.

The author wishes to acknowledge the valuable assistance of Israel Krongold in programmer training and the UNIVAC staff at New York University in regard to machine time and computing aids.

$$\varphi(\xi) = \xi + p\varphi_1(\xi) + p^2\varphi_2(\xi) + \ldots \tag{2}$$

where p is a parameter to be suitably selected. The first term trivially satisfies the boundary condition $\varphi'(\infty) = 1$. The remaining procedure is to satisfy the wall conditions with $\varphi_1(\xi)$, while the higher-order terms satisfy zero conditions. These terms act to bring the series into agreement with the solution of the differential equation. In the present case it happens that $p = 1$ may be chosen and no other parameter, in particular $1/\varphi_0$, arises in a natural way to form either a power series or an asymptotic series.

It then is sufficient to use as boundary conditions

$$\left.\begin{array}{l} \varphi_i'(\infty) = 0, \quad \varphi_{i+1}(0) = 0, \\ \varphi_1(0) = -\varphi_1'(0) = 1/p, \quad \varphi_{i+1}'(0) = 0 \end{array}\right\} \quad i = 1, 2, \ldots \tag{3}$$

Substituting the series into Eq. (1) and collecting terms by powers of p, for each i

$$\varphi_i''' + \xi\varphi_i'' - 2\varphi_i' = f_i(\varphi_1, \varphi_2, \ldots, \varphi_{i-1}) = f_i(\xi) \tag{4}$$

where

$$f_1(\xi) = 0, \quad f_2(\xi) = \varphi_1'^2 - \varphi_1\varphi_1''$$

and for each i, $f_i(\xi)$ can be written explicitly as a homogeneous function. All the equations have the same form of complementary function:

$$A_i + B_i[(\xi^3/3) + \xi] + C_i e^{-\xi^2/4} D_{-4}(\xi) \tag{5}$$

where A_i, B_i, C_i are determined by boundary conditions, and $D_{-4}(\xi)$ is a parabolic cylinder function.[3] The method of variation of parameters gives as a particular solution, for $i \geq 2$,

$$_iC_1(\xi) + {}_iC_2(\xi)\,[(\xi^3/3) + \xi] + {}_iC_3(\xi)e^{-\xi^2/4}\,D_{-4}(\xi) \tag{6}$$

where

$$\left.\begin{array}{l} {}_iC_1(\xi) = -1/3\displaystyle\int_0^\xi e^{-\eta^2/4}\, g_i(\eta)d\eta, \\ {}_iC_2(\xi) = \displaystyle\int_0^\xi g_i(\eta)D_{-3}(\eta)d\eta, \\ {}_iC_3(\xi) = \displaystyle\int_0^\xi e^{\eta^2/4}\,(\eta^2 + 1)g_i(\eta)d\eta, \\ g_i(\eta) = e^{\eta^2/4}\, f_i(\eta) \end{array}\right\} \tag{7}$$

When the boundary conditions (3) are applied to Eq. (2), it is found that each constant A_i, B_i, C_i contains the factor $1/p^i$ because the $f_i(\xi)$ are homogeneous in the functions $\varphi_j(\xi)$. Thus, it is sufficient to take $p = 1$, since neither the equations nor the boundary conditions place a necessary requirement on p.

For $i = 1$ the particular solution is zero and boundary conditions give a final form

$$\varphi_1(\xi) = [\varphi_0 - (2/3)\sqrt{2/\pi}] + 2\sqrt{2/\pi}\, e^{-\xi^2/4}D_{-4}(\xi) \tag{8}$$

For $i \geq 2$,

$$A_i = -(2/3)\sqrt{2/\pi}B_i,$$
$$B_i = -\int_0^\infty g_i(\eta)D_{-4}(\eta)d\eta, \quad C_i = -3A_i \tag{9}$$

Numerical calculations of the function

$$\varphi(\xi) \cong \xi + \varphi_1(\xi) + \varphi_2(\xi)$$

and its first derivative were made for $\varphi_0 = 0$, 1, 2, 3, 10, and 100, using Simpson's rule on the integrals, with an interval of $\eta/\sqrt{2} = 0.005$. The first three cases are shown in Figs. 1 and 2. For $\varphi_0 = 10$, results seemed to be good to two digits, and for $\varphi_0 = 100$ to only one digit. But for usual dynamic conditions of flow through cloth $\varphi_0 \cong 250$ seems appropriate. Hence, additional terms in the series, or a direct numerical solution of the differential equation, will be required for such a problem.

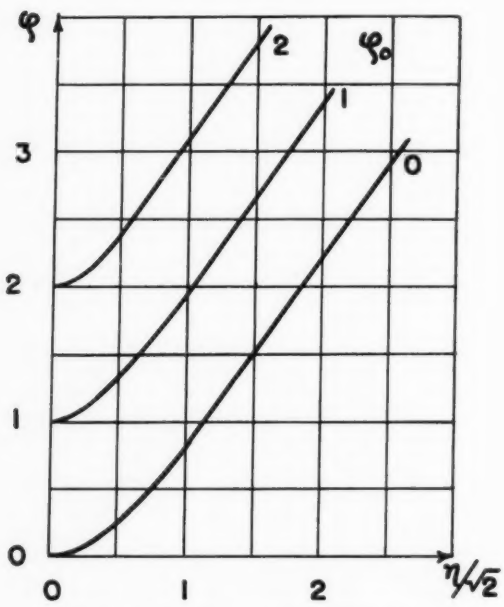

FIG. 1. Solutions for φ at three values for φ_0.

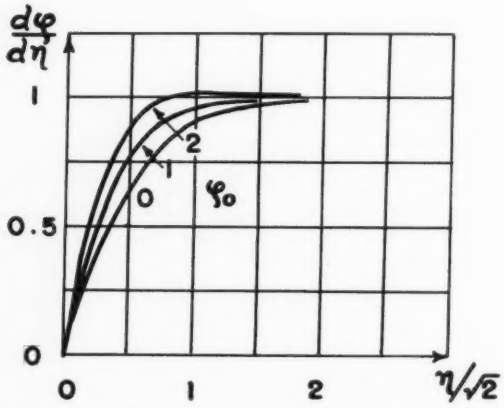

FIG. 2. Solutions for φ' at three values for φ_0.

REFERENCES

[1] Durand, W. F., (Ed.), *Aerodynamic Theory*, Vol. III, Julius Springer, Berlin, 1935.

[2] Fettis, H. E., *On the Integration of a Class of Differential Equations Occurring in Boundary Layer and Other Hydrodynamic Problems*, Proceedings of the 4th Midwestern Conference on Fluid Mechanics, Purdue University, 1956.

[3] Magnus, W., and Oberhettinger, F., *Formulas and Theorems for the Functions of Mathematical Physics*, Chelsea, 1954.

Hydromagnetic Effects on Stagnation-Point Heat Transfer

Joseph L. Neuringer and William McIlroy
Scientific Research Staff, Republic Aviation Corporation, Farmingdale, N.Y.

December 9, 1957

INTRODUCTION

IN A PREVIOUS PAPER[1] by the authors, an investigation was initiated to study the hydromagnetic interaction of an electrically conducting viscous fluid with an applied magnetic field in stagnation-point flow. In the present note (see also reference 2) this investigation is carried a step further, and the corresponding influence on aerodynamic heating is presented.

The notation employed will be that already clearly outlined in reference 1. However, a few more definitions will be necessary:

T_e^* = temperature of the gas behind the detached nose shock
T_w^* = temperature of the surface at the stagnation point, assumed very much smaller than T_e^*
U_0^* = gas velocity leaving the shock front
U_∞^* = speed of the body—i.e., the gas speed entering the shock
Γ = ratio of the specific heats behind the shock = c_p/c_v
Pr = Prandtl Number of the gas behind the shock, assumed equal to 0.70
c_f = skin friction coefficient = $2\tau/\rho_0 b^2 x^{*2}$
Re_{x^*} = Reynolds Number, based on the local value of x^* and the local external tangential flow velocity = bx^*
Nu = Nusselt Number = $qx^*/k(T_e^* - T_w^*)$

Discussion

The theoretical model studied here is the same as that in reference 1. By virtue of the incompressibility assumption and temperature-independent fluid properties, the momentum and continuity equations can be solved independently of the energy equation, and the solution for the velocity distribution, $u(y)$, can then be used to solve for the temperature in the energy equation.

It is further possible to show that the solution reduces to the familiar solution obtained by Squire (see reference 3, page 631) for incompressible stagnation flow, subject to certain conditions which will now be enumerated.

Making the usual boundary-layer assumptions in the energy equation (see reference 3, page 612), but including the Joulean dissipation term J^{*2}/σ, the convective heat-flow equation can be written in the form

$$\rho_0 C_p[U^*(\partial T^*/\partial x^*) + V^*(\partial T^*/\partial y^*)] = U^*(\partial p^*/\partial x^*) + k(\partial^2 T^*/\partial y^{*2}) + \mu(\partial U^*/\partial y^*)^2 + (J^{*2}/\sigma)$$

This equation may be considerably simplified. In the first place, the small perturbations in the electromagnetic field strengths due to the magneto-hydrodynamic interaction may be neglected. It follows, therefore, that the Joulean heating may be written simply as $\sigma U^{*2} B_0^{*2}$, when the definition of J^* in reference 1 is used. Further, following the standard procedures of order analysis, it can be shown, (see reference 3, page 613), that both viscous heating and Joulean heating are likely to be small compared to conduction heating. In other words, the heat-convection equation can be rewritten in the following simpler form:

$$\{U^*(\partial T^*/\partial x^*) + V^*(\partial T^*/\partial y^*)\} = \kappa(\partial^2 T^*/\partial y^{*2})$$

where $\kappa = \{k/c_p\rho_0\}$, provided that

$$\{U_0^{*2}/c_p(T_e^* - T_w^*)\}$$

and

$$\{[h^2(0)/\gamma]U_0^{*2}/c_p(T_e^* - T_w^*)\}$$

Table 1

h(0)	$h^2(0)/\gamma$	b/b_0	$(b/b_0)^{1/2}$	α/α_0	q/q_0	$(b/b_0)^{3/2}$	$u'(0)/u_0'(0)$	τ/τ_0	$c_f Re_{x^*}/Nu$
$\gamma = 10^5$									
0	0.000	1.000	1.000	1.000	1.000	1.000	1.000	1.000	4.96
-100	0.100	0.964	0.977	1.005	0.982	0.920	1.033	0.952	5.09
-300	0.900	0.726	0.852	1.037	0.883	0.620	1.260	0.782	6.02
-400	1.600	0.622	0.789	1.055	0.834	0.492	1.430	0.703	6.72
-500	2.500	0.535	0.732	1.077	0.788	0.392	1.624	0.637	7.50
-700	4.900	0.412	0.642	1.114	0.715	0.267	2.052	0.548	9.14
$\gamma = 2 \times 10^5$									
-300	0.450	0.830	0.910	1.021	0.929	0.760	1.138	0.865	5.53
-500	1.250	0.667	0.815	1.048	0.854	0.540	1.349	0.728	6.38
$\gamma = 10^6$									
-800	0.640	0.782	0.884	1.028	0.909	0.690	1.191	0.822	5.74

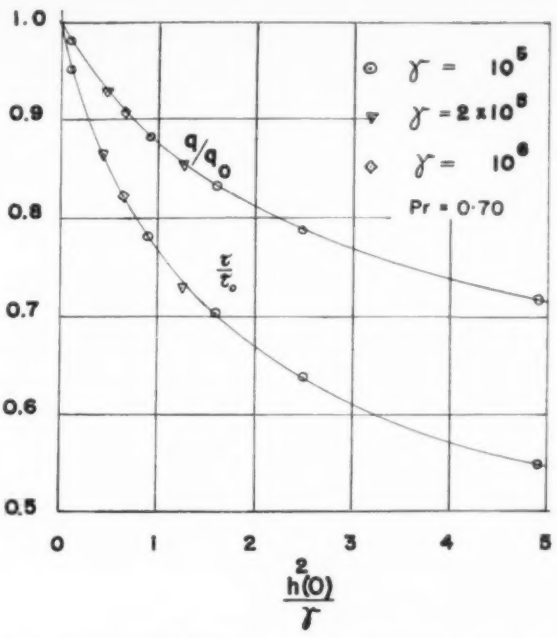

Fig. 1. Shear-stress and heat-transfer ratios versus interaction parameter $h^2(0)/\gamma$.

are both small compared to unity. For strong shocks the first condition is always satisfied, and for the values of the interaction parameter considered in this note, $h^2(0)/\gamma$, the second requirement is also satisfied.

To solve the above equation for temperature, use is made of the solutions for U^* and V^* obtained in reference 1. The effect of the Joulean heating on the inviscid flow is assumed negligible, so that a constant temperature independent of x^* may be used as boundary condition at infinity. The final form of the result is identical to Squire's solution—namely,

$$Nu_{\text{local}} = \alpha(Pr)Re_{x^*}^{1/2}$$

where

$$1/\alpha(Pr) = \int_0^\infty \left\{\exp - Pr\int_0^y u(y)dy\right\}dy$$

This integral, $1/\alpha(Pr)$, was calculated on IBM for various values of $h^2(0)/\gamma$.

The ratio of the heat transfers, with and without the magnetic field, is

$$q/q_0 = (\alpha/\alpha_0)(b/b_0)^{1/2}$$

Here b and b_0 are the external, inviscid, velocity-gradient parameters with and without a magnetic field, respectively. In reference 1 the ratio b/b_0 has been shown to equal $\{1 + [h^2(0)/\gamma]\}^{-1/2}$.

Results of the Analysis

From the above expression for the heat-transfer ratio q/q_0, it can be seen that it consists of two parts; one part, α/α_0, which is a function of the dimensionless velocity profile $u(y)$ alone, and a second part which depends on the character of the external inviscid flow field. As a result of the analysis (see Table 1), it is readily seen that the first part increases slightly with increasing $(h^2(0)/\gamma)$, while the second part decreases. A similar situation exists with respect to the shear-stress ratio. In reference 1 it was shown that

$$\tau/\tau_0 = \{u''(0)/u_0''(0)\}\{b/b_0\}^{3/2}$$

i.e., a product of a nondimensional velocity-profile-dependent portion, $\{u''(0)/u_0''(0)\}$, and an external inviscid-flow-dependent

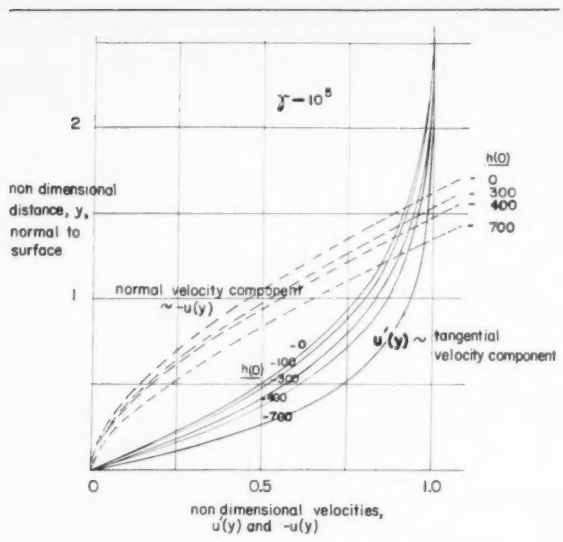

FIG. 2. Typical velocity profiles.

portion, $(b/b_0)^{3/2}$. In Fig. 1, the ratios q/q_0 and τ/τ_0 are plotted, and it is shown that the heat transfer decreases less rapidly than the skin friction.

The effect of the magnetic field on the dimensionless velocity profiles, tangential and normal to the plate, is apparent from Fig. 2. The profile approaches more and more the shape commonly associated with a turbulent boundary layer, and this would lead one to believe that the magnetic field has the added effect of increasing the stability of the flow.

The value of the Reynolds analogy parameter,

$$c_f Re_{x^*}/Nu = 2u''(0)/\alpha(Pr)$$

is tabulated in Table 1. It is seen that this is not a constant with varying $h^2(0)/\gamma$.

Finally, it must be emphasized that the present solution exists only for small values of distance x^*, and for values of $h^2(0)/\gamma$ consistent with the restrictions noted in the discussion. For sufficiently high values of this interaction parameter, the Joulean heating term assumes sufficient magnitude to be included in the energy equation.

CONCLUSIONS

As a result of the above analysis, it is concluded that it is possible to reduce the heat transfer at a stagnation point (when the gas there is ionized) by application of magnetic fields normal to the surface. The reduction can be of considerable magnitude, even in the presence of magnetic fields of reasonable strength and gases of relatively small electrical conductivity. As a typical example, from Fig. 2 it appears that for $\gamma = 10^5$ and $h^2(0)/\gamma = 4.9$, the heat transfer is reduced 28 per cent with a corresponding decrease of 45 per cent in the skin friction.

With the typical electrical conductivity, density, external-velocity parameter b_0, etc., used in reference 1, this would require a magnetic field strength of 3,200 gauss.

REFERENCES

[1] Neuringer, J. L., and McIlroy, W., *Incompressible Two-Dimensional, Stagnation-Point Flow of an Electrically Conducting Viscous Fluid in the Presence of a Magnetic Field*, Journal of the Aeronautical Sciences, Vol. 25, No. 3, pp. 194–198, March, 1958. Also Republic Aviation Report, June 12, 1957.

[2] Neuringer, J. L., and McIlroy, W., *Hydromagnetic Effects on Stagnation Point Heat Transfer*, Republic Aviation Report, November 29, 1957.

[3] Goldstein, S., (Ed.), *Modern Developments in Fluid Dynamics*, Vol. II, Oxford University Press, 1952.

Magnetohydrodynamic Analysis of Heat Transfer Near a Stagnation Point

Vernon J. Rossow
Aeronautical Research Scientist, Ames Aeronautical Laboratory, NACA, Moffett Field, Calif.
December 20, 1957

SUMMARY

The change in the skin friction brought about by a magnetic field perpendicular to a flat plate was studied theoretically in reference 1 for the case of flow near a two-dimensional stagnation point. In the analysis, the electrically conducting fluid was assumed to be incompressible and to have constant fluid properties. The change in the imposed magnetic field induced by the electric currents in the fluid was also considered.

The purposes of this note are to present the results of a heat-transfer analysis for the problem of reference 1, and to compare the skin friction found in reference 1 with that obtained by the more approximate method of reference 2. The intent of the second objective is to find the degree of approximation made by ignoring the secondary magnetic field which is induced by the motion of the fluid through the basic imposed magnetic field.

ANALYSIS

THE DIFFERENTIAL EQUATIONS which describe the motion of the fluid and the transport of thermal energy in the presence of the magnetic field are, from reference 2,

$$u(\partial u/\partial x) + v(\partial u/\partial y) + (\sigma B_0^2/\rho)u = -(1/\rho)(\partial p/\partial x) + \nu[(\partial^2 u/\partial x^2) + (\partial^2 u/\partial y^2)] \quad (1a)$$

$$u(\partial u/\partial x) + v(\partial v/\partial y) = -(1/\rho)(\partial p/\partial y) + \nu[(\partial^2 v/\partial x^2) + (\partial^2 v/\partial y^2)] \quad (1b)$$

$$(\partial u/\partial x) + (\partial v/\partial y) = 0 \quad (2)$$

$$C_p u(\partial T/\partial x) + C_p v(\partial T/\partial y) - (\sigma B_0^2/\rho)u^2 = (C_p \nu/Pr)(\partial^2 T/\partial y^2) + \nu(\partial u/\partial y)^2 + (u/\rho)(\partial p/\partial x) \quad (3)$$

where the symbols σ and B_0 denote the electrical conductivity of the fluid and the imposed magnetic field strength. Eqs. (1a) and (1b) are the Navier-Stokes relations with the additional term in Eq. (1a) accounting for the magnetic field-fluid interaction.

A set of ordinary differential equations for the velocity and temperature distribution in the boundary layer near a stagnation point may be obtained by introducing the new variables,

$$\eta = \sqrt{a_0/\nu}\, y \quad (4a)$$

$$u = a_0 x \varphi'(\eta) \quad (4b)$$

$$v = -\sqrt{\nu a_0}\varphi(\eta) \quad (4c)$$

$$p_0 - p = (\rho/2)a_0^2[x^2 + (2\sqrt{a_0\nu}/a_0^2)\phi(\eta)] \quad (4d)$$

$$T(\eta) = T_{st} - [(U^2 + V^2)/2C_p]\theta_1(\eta) - (T_{st} - T_w)\theta_2(\eta) \quad (4e)$$

where u and v are the velocity components in the boundary layer and $U = ax$ and $V = ay$ are the velocity components outside the boundary layer. Here x is measured along the wall from the stagnation point and y is normal to the surface into the fluid. The stagnation and wall temperatures are, respectively, T_{st} and T_w. When the magnetic parameter $\bar{m}$ is zero, $U = a_0 x$ and $V = a_0 y$. Since the boundary layer is assumed thin, the velocity at its edge is

$$U^2 + V^2 = a^2(x^2 + y^2) \approx a^2 x^2$$

Therefore Eq. (4e) becomes

$$T(\eta) = T_{st} - (a^2 x^2/2C_p)\theta_1(\eta) - (T_{st} - T_w)\theta_2(\eta) \quad (4f)$$

When the above variables are introduced into Eqs. (1), (2), and (3) and the Prandtl Number is taken equal to one, the following set of ordinary differential equations is found:

$$\varphi''' + \varphi\varphi'' - (\varphi')^2 - \bar{m}\varphi' + 1 = 0 \quad (5)$$

$$(\theta_1'' + \varphi\theta_1' - 2\varphi'\theta_1)(a^2/a_0^2) - 2\bar{m}(\varphi')^2 - 2(\varphi'')^2 + 2\varphi' = 0 \quad (6)$$

$$\theta_2'' + \varphi\theta_2' = 0 \quad (7)$$

where $\bar{m} = \sigma B_0^2/\rho a_0$. The boundary conditions are

TABLE 1

$\bar{m}$	$\varphi''(0)$	$a/a_0 = \varphi'(\infty)$	$\frac{a^2\theta_1(\infty)}{a_0^2}$	$\theta_2'(0)$	τ/τ_0	q/q_0	Reference 1 $h^2(0)/\gamma$	Reference 1 $\varphi''(0)$
0	1.2326	1.0000	1.0000	−0.5705	1.0000	1.0000	0	1.2326
0.0953	1.1844	0.9535	0.9091	−0.5601	0.9609	0.9827	0.1	1.1863
0.3381	1.0756	0.8452	0.7160	−0.5350	0.8726	0.9377	0.4	1.0735
0.6529	0.9600	0.7255	0.5264	−0.5053	0.7789	0.8857	0.9	0.9611
0.9923	0.8615	0.6202	0.3847	−0.4774	0.6989	0.8369	1.6	0.8635

$$\left.\begin{aligned} \varphi &= \varphi' = 0 \\ \theta_1 &= \theta_1' = 0 \\ \theta_2 &= 1 \end{aligned}\right\} \quad \text{at} \quad \eta = 0$$

$$\left.\begin{aligned} \varphi' &= a/a_0 \\ \theta_2 &= 0 \end{aligned}\right\} \quad \text{at edge of boundary layer}$$

Eq. (7) is the differential equation found by Squire and presented in reference 3, but the boundary conditions are different. The solution described by Eq. (6) with m set equal to zero or a constant has not been considered previously. Eq. (5) is the usual differential equation found for the velocity in the boundary layer near a two-dimensional stagnation point with an additional term arising from the magnetic field fluid interaction.

Eqs. (5), (6), and (7) were integrated numerically for several values of the magnetic parameter $\bar{m}$ on the IBM 650 Magnetic-Drum Data-Processing Machine using the Runge-Kutta method. The essential results are presented in Table 1. The velocity and temperature profiles in the boundary layer are shown in Fig. 1 for $x = \sqrt{\nu/a_0}$ and $a_0\nu/2C_p = T_{st} - T_w$. The temperature profiles would more nearly resemble those of the flat-plate boundary layer if a larger value of x had been chosen. The reduction in the skin friction and heat transfer brought about by the magnetic field is shown in Fig. 2, where the viscous shear and heat transfer are defined as

$$\tau = \mu \left.\frac{\partial u}{\partial y}\right)_{y=0} = \mu a_0 x \sqrt{\frac{a_0}{\nu}}\, \varphi''(0)$$

$$q = k \left.\frac{\partial T}{\partial y}\right)_{y=0} = k(T_{st} - T_w) \sqrt{\frac{a_0}{\nu}}\, \theta_2'(0)$$

The ratios of these parameters in the magnetic case to the nonmagnetic case (subscript zero) are then,

$$\tau/\tau_0 = [\varphi''(0)]_{\bar{m}}/[\varphi''(0)]_{\bar{m}=0}$$

$$q/q_0 = [\theta_2'(0)]_{\bar{m}}/[\theta_2'(0)]_{\bar{m}=0}$$

The values of the magnetic parameter were chosen so that a direct comparison could be made with the skin-friction results of reference 1. It is to be noted in Table 1 that, up to a magnetic parameter of one, an error of less than 1 part in 400 is caused by ignoring the induced secondary magnetic field in the boundary-layer solution. Hence, the simplification introduced in reference 2 causes no appreciable error and is a good approximation for many problems.

The heat transfer is noted to decrease with increase in magnetic field strength independent of the distance from the stagnation point. Experimental results may depart from the present theory when density variations (which were neglected) arise either because of large temperature variations or because the results are applied too far from the stagnation point.

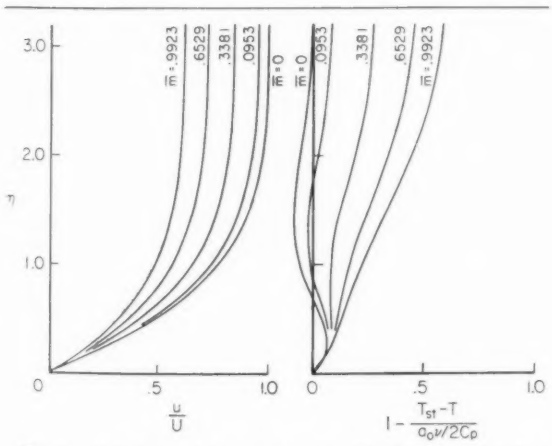

FIG. 1. Velocity and temperature profiles for several values of $\bar{m}$ at $x = \sqrt{\nu/a_0}$ with $T_{st} - T_w = a_0\nu/2C_p$. (a) Velocity. (b) Temperature.

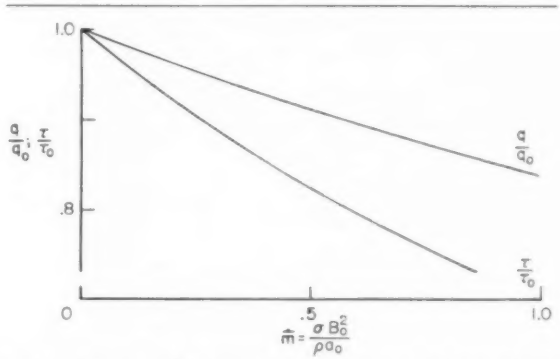

FIG. 2. Reduction in viscous shear and heat transfer as a function of the magnetic parameter $\bar{m}$.

The heat transfer is noted to decrease with increase in magnetic field strength independent of the distance from the stagnation point. Experimental results may depart from the present theory when density variations (which were neglected) arise either because of large temperature variations or because the results are applied too far from the stagnation point.

REFERENCES

[1] Neuringer, Joseph L., and McIlroy, William, *Two-Dimensional Flow in the Vicinity of the Stagnation Point of an Incompressible, Viscous, Electrically Conducting Fluid in the Presence of a Magnetic Field*, Republic Aviation Corp., June 12, 1957.

[2] Rossow, Vernon J., *On Flow of Electrically Conducting Fluids Over a Flat Plate in the Presence of a Transverse Magnetic Field*, NACA TN 3971, 1957.

[3] Goldstein, S. (Ed.), *Modern Developments in Fluid Dynamics*, Vol. II, The Clarendon Press, Oxford, 1938.

Space-Time Correlations of the Fluctuating Wall Pressure in a Turbulent Boundary Layer*

W. W. Willmarth

Senior Research Fellow, Guggenheim Aeronautical Laboratory, California Institute of Technology, Pasadena, Calif.

January 3, 1958

THE PROBLEM of turbulent boundary-layer induced noise inside an airplane fuselage has been discussed and formulated by a number of authors.[1, 2, 3] The random character of the

* The research in this note was supported by National Advisory Committee for Aeronautics, Contract No. Naw-6517.

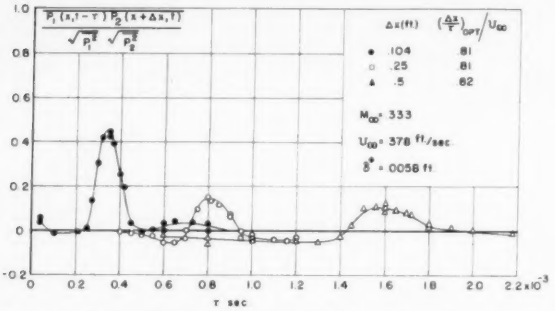

FIG. 1a. Streamwise space-time correlation of the wall pressure in a turbulent boundary layer.

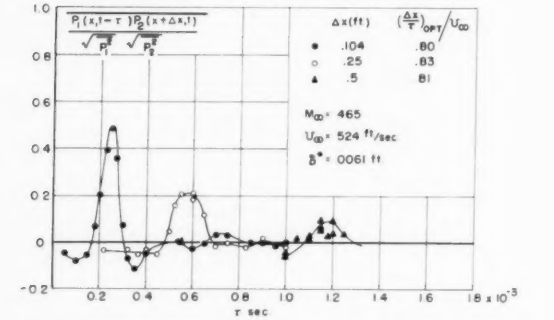

FIG. 1b. Streamwise space-time correlation of the wall pressure in a turbulent boundary layer.

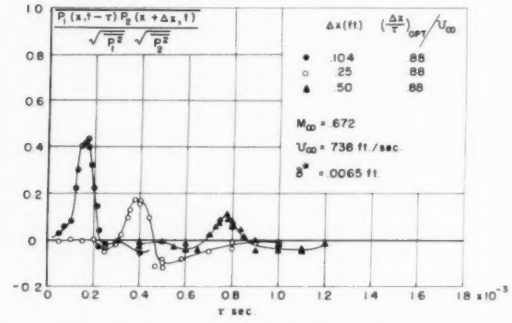

FIG. 1c. Streamwise space-time correlation of the wall pressure in a turbulent boundary layer.

pressure fluctuations which excite the airplane skin make a statistical description of the problem necessary. Thus, one asks for the statistical properties of the wall-pressure fluctuations in the turbulent boundary layer in order that the statistical properties of the motion of the airplane skin and the internal sound field generated by this motion may be computed.

It has been conjectured[1, 2] that the governing phenomenon for the generation of internal noise is a type of resonance in which traveling waves in the skin are excited by the pressure fluctuations in the turbulent boundary layer. The magnitude and other characteristics of this resonance are determined by the properties of both the skin and the pressure fluctuations. Phillips[4] has recently discussed an analogous problem for the generation of ocean waves by turbulent wind. He also finds that a resonance phenomena dominates the situation and shows how convected normal pressure fluctuations can cause appreciable wave amplitudes.

In this note measurements of the streamwise space-time correlation

$$\overline{p(x, t - \tau)\, p(x + \Delta x, t)}$$

are described. p is the pressure, t is the time, x and Δx are distances measured in the stream direction, and τ is the delay time.

The measurements were performed in a low-noise-level tunnel[5] using barium-titanate pressure transducers[6] and Skinner's electronic time correlator.[7] The time correlator samples one signal and stores it in a digital memory device for a time τ, whereupon a sample from the other signal is multiplied with the stored sample. The output of the device is averaged, giving the time correlation of the two signals.

In Figs. 1a, 1b, and 1c the streamwise space-time correlation of the wall pressure in a turbulent boundary layer is presented for three different free-stream velocities. At each stream velocity the pressure transducers were separated by 0.104 ft., 0.25 ft., and 0.50 ft. For each separation distance there is a time delay τ, called the optimum time delay, at which the correlation between the pressures is a maximum. If one forms the ratio $\Delta x/\tau_{opt.}$ it is found that $\Delta x/\tau_{opt.} \doteq 0.85 U_\infty$ for the nine cases investigated. The boundary-layer displacement thickness was $\delta^* \doteq 0.0062$ ft. for all the measurements and the Reynolds Number was approximately 9×10^6 at the lowest speed and 15×10^6 at the highest speed.

One can interpret the peaks in the correlation of the pressures as the result of a convected pattern of turbulent flow in the boundary layer. It should be noted that a given pattern of turbulence has effectively been destroyed,

$$\overline{p_1(x, t - \tau) p_2(x + \Delta x, \tau)} / \sqrt{\overline{p_1}^2} \sqrt{\overline{p_2}^2} \approx 0.1$$

in a time $\tau \doteq 100\, \delta^*/U_\infty$.

A complete report of these measurements and of measurements of the spectrum of the wall pressure is being prepared.

REFERENCES

[1] Corcos, G. M., and Liepmann, H. W., *On the Transmission Through a Fuselage Wall of Boundary Layer Noise*, Douglas Aircraft Co. Report No. SM-19570, December, 1955.

[2] Ribner, H. S., *Boundary-Layer-Induced Noise in the Interior of Aircraft*, Univ. of Toronto, UTIA Report No. 37, April, 1956.

[3] Kraichnan, R. H., *Noise Transmission from Boundary Layer Pressure Fluctuations*, J. Acous. Soc. Am., Vol. 29, No. 1(65), January, 1957.

[4] Phillips, O. M., *On the Generation of Waves by Turbulent Wind*, J. Fluid Mech., Vol. 2, Part 5, July, 1957.

[5] Willmarth, W. W., *Wall Pressure Fluctuations in a Turbulent Boundary Layer*, to be published as an NACA Technical Note.

[6] Willmarth, W. W., *A Small Barium Titanate Transducer for Aerodynamic or Acoustic Pressure Measurements*, Submitted to Review of Scientific Instruments.

[7] Skinner, G. T., *Time Correlator for Problems in Aerodynamics*, NACA TN 3682, June, 1956.

Blunt Body Separation at Supersonic Speeds

Paul F. Brinich
Lewis Flight Propulsion Laboratory, NACA, Cleveland, Ohio

January 17, 1958

SHOCK TUBE EXPERIMENTS conducted at the Cornell Aeronautical Laboratory showed the existence of a separated flow region ahead of a blunt body. This phenomenon was observed at a Mach Number of 5.0 and was found to be caused by the impingement and subsequent upstream reflection of dust particles present in the shock tube gas.

Blunt body experiments conducted at the NACA Lewis laboratory in the 1 by 1 ft. variable Reynolds Number wind tunnel revealed the same phenomenon at a Mach Number of 3.1. This phenomenon was observed both with instantaneous spark schlieren photography and with high-speed schlieren motion pictures. Schlieren photographs of a blunt cone with and without the separated conical flow region are shown in Figs. 1 and 2.

Out of approximately 20,000 frames taken with the high-speed motion picture camera, flow separation was observed only once.

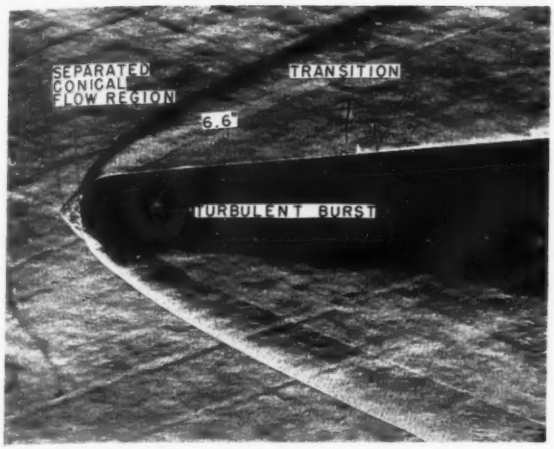

FIG. 1. Separated flow conical shock configuration. Free-stream Reynolds Number, 6.25×10^6/in.

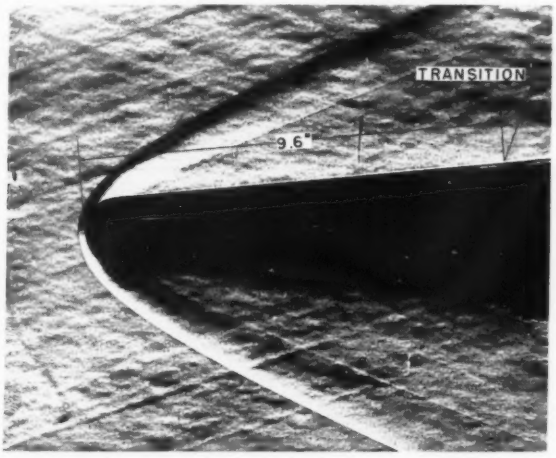

FIG. 2. Conventional blunt tip shock configuration. Free-stream Reynolds Number, 6.25×10^6/in.

On this occasion it appeared on three consecutive frames at a film speed of 1400 frames per second. The description of the separation phenomenon given in reference 1 agrees with that observed in the NACA motion pictures, inasmuch as the separated region suddenly erupted as a dust particle was reflected upstream at the blunt nose and gradually collapsed as the particle was again blown downstream. This relatively infrequent occurrence of separation (three out of 20,000 frames) in the 1 by 1 ft. variable Reynolds Number wind tunnel indicates that the phenomenon probably has an insignificantly small effect on the heat transfer and boundary-layer measurements made in this facility.

It was suggested in reference 1 that the separation region at the blunt nose might be used as a means of reducing the heat transfer in the stagnation region if a sufficient number of dust particles existed in the airstream. Whereas this method might work at the nose, Figs. 1 and 2 suggest that the heat transfer would be increased over the downstream portions of the body. A comparison of the transition locations indicate that the extent of laminar flow is greatly diminished when the nose separation occurs, and that turbulent heat-transfer rates would be encountered over much of the afterbody.

A burst of turbulence which accompanied the unsteady flow separation is also indicated in Fig. 1 and seems to encircle the model. The presence of this burst suggests that early transition may be the result of increased spot production frequency and perhaps that the spot production in this case is somehow related to the presence of dust particles in the airstream.

REFERENCE

[1] Hertzberg, A., *The Shock Tunnel and Its Applications to Hypersonic Flight*. Cornell Aeronautical Laboratory Report No. AD-1052-A-5, June, 1957.

Some Solutions of the Navier-Stokes Equations With Time Dependent Density

Roger D. Sullivan and Coleman duP. Donaldson
Aeronautical Research Associates of Princeton, Princeton, N.J.
January 20, 1958

IN THE COURSE of an investigation of time-dependent boundary-layer problems an apparently new family of exact solutions of the two-dimensional Navier-Stokes equations has been found. They apply to cases in which the density of the fluid is a function of the time only, and the other variables are functions of one space coordinate and the time. The viscosity is taken as a constant.

These solutions represent the boundary layer on an infinite flat plate moving with variable velocity at low Mach Numbers in an environment of changing density, or a generalized Couette flow produced by parallel walls which move in and out as well as in their own planes.

Taking the density, ρ, as a function of the time, t, and the velocity components in the x and y directions, u and v, respectively, as well as the pressure, p, as functions of y and t, the Navier-Stokes equations with constant viscosities, μ and λ, are

$$\rho[(\partial u/\partial t) + v(\partial u/\partial y)] = \mu(\partial^2 u/\partial y^2) \tag{1}$$

$$\rho[(\partial v/\partial t) + v(\partial v/\partial y)] = -(\partial p/\partial y) + [(4/3)\mu + \lambda](\partial^2 v/\partial y^2) \tag{2}$$

and the equation of continuity is

$$\rho' + \rho(\partial v/\partial y) = 0 \tag{3}$$

where the prime denotes differentiation with respect to t.

Eq. (3) can be integrated immediately to give

$$v = -(\rho'/\rho)y \tag{4}$$

if we restrict ourselves to cases where $y = 0$ represents a wall so that $v(0, t) = 0$. If there is another flat wall at $y = h(t)$, from conservation of mass we must have

$$\rho h = \text{constant} \tag{5}$$

(If the relative vertical motion of the plates is to be regarded as the cause of the density variation, this motion must be slow enough so that the density is essentially a function of t only.) In this case Eq. (4) can be written $v = (h'/h)y$ and in particular, $v = h'$ when $y = h$, as is to be expected.

Substitution of v from Eq. (4) into Eq. (2) and integrating gives

$$p = (1/2)\rho[(\rho''/\rho) - 2(\rho'/\rho)^2]y^2 + p(0, t) \tag{6}$$

The main interest lies in the determination of u. Eq. (1), with v determined by Eq. (4), becomes

$$\rho(\partial u/\partial t) = \mu(\partial^2 u/\partial y^2) + \rho' y(\partial u/\partial y) \tag{7}$$

We note that a solution of this equation is given by

$$u = c_1 \rho y \tag{8}$$

Considering the flow between two infinite plates, one at $y = 0$ and the other at $y = h(t)$, Eq. (8) becomes, using Eq. (5), $u = c_2 y/h$, and we see that this solution represents the case in which the wall at $y = 0$ is stationary and the wall at $y = h$ is moving in its own plane with the constant velocity c_2 (postulating no slip at the walls).

This solution suggests the substitutions

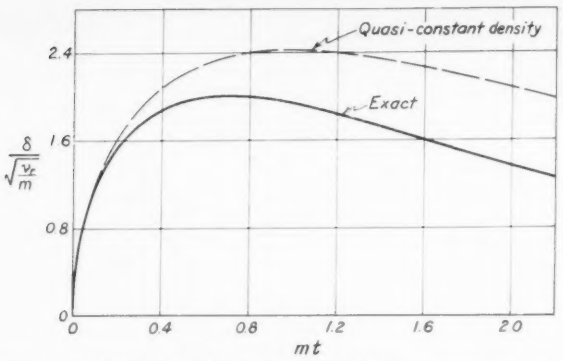

FIG. 1. Variation of boundary-layer thickness with time on a suddenly moved flat plate with exponential density variation.

$$\eta = (\rho/\rho_r)y \tag{9}$$

$$\tau = \int (\rho/\rho_r)dt \tag{10}$$

where ρ_r is a reference density. Eq. (7) becomes

$$\partial u/\partial \tau = \nu_r(\partial^2 u/\partial \eta^2) \tag{11}$$

where $\nu_r = \mu/\rho_r$. This, of course, is the well known one-dimensional heat equation, numerous solutions of which are recorded in the literature. Any of these can be used for arbitrary variations of density with time, provided only that these variations make sense physically. The mathematical requirements on the function $\rho(t)$ are simply that it must be integrable and that it must remain positive (or negative) so that the transformation given by Eq. (10) exists and is one to one. Since in all cases η is proportional to y at any time t, the instantaneous velocity profile—that is, the variation of u with y—always has the characteristics of the profile in the constant density case, where η can be identified with y.

For example, a solution given in reference 1 is written in our notation

$$u = u_0 \operatorname{erfc} \zeta = u_0(1 - \operatorname{erf} \zeta) \tag{12}$$

where

$$\zeta = \eta/2\sqrt{\nu_r \tau} \tag{13}$$

which gives a boundary-layer like flow for small τ. Eq. (13) may represent the solution for a suddenly moved infinite flat plate in a region where the density may be supposed to be varied in an arbitrary manner by the vertical motion of a plane at a distance from the suddenly moved plate which is large compared to the thickness of the boundary layer.

As an interesting case of this solution, assume that the density varies in an exponential manner

$$\rho = \rho_r e^{mt} \tag{14}$$

where m is a constant. The boundary-layer thickness, δ, can be taken as the value of y for which $\zeta = 2$. But, from Eqs. (9), (10), (13), and (14), we find

$$\zeta = e^{mt}y/2\sqrt{(\nu_r/m)\,(e^{mt} - 1)}$$

and, therefore,

$$\delta = 4\sqrt{\nu_r/m}\, e^{-mt} \sqrt{e^{mt} - 1}$$

This relation is plotted in Fig. 1. It is seen that the thickness actually decreases at large values of t. A comparison can be made with what might be called the solution for quasi-constant density—that is, when ζ is given by

$$\zeta = y/2\sqrt{\nu t}$$

with

$$\nu = \nu_r(\rho_r/\rho) = \nu_r e^{-mt}$$

This gives

$$\delta = 4\sqrt{\nu_r/m}\, e^{-mt/2} \sqrt{mt}$$

which is also plotted in Fig. 1. This too shows a decrease for large t, but the effect is considerably delayed and weaker than in the exact solution.

These results may be interpreted as follows. Initially the boundary layer on the suddenly moved plate grows rapidly due to the high shear and low kinematic viscosity. After a time, however, the increasing kinematic viscosity causes a reduction in the boundary-layer thickness. This thinning is larger in the exact case as a result of the convection of the outer layers of the boundary layer toward the plate, as required by continuity.

REFERENCE

[1] Durand, William Frederick (Ed.), *Aerodynamic Theory*, Vol. III, pp. 64–65; California Institute of Technology, Pasadena, California, 1943.

On the Character of the Instability of the Laminar Boundary Layer Near the Nose of a Blunt Body*

A. M. Kuethe
Professor, Department of Aeronautical Engineering, University of Michigan, Ann Arbor, Michigan

January 24, 1958

RECORDS WERE OBTAINED of the hot-wire response to velocity of fluctuations in the boundary layer of a body of revolution

* The experiments in this note were supported by the USAF Office of Scientific Research, ARDC, and carried out under contract number AF18 (603)-34. The analysis referred to was carried out by the author during the summer of 1957 as a consultant of the RAND Corporation. The assistance of K. R. Raman and Ralph Deitrick in obtaining the experimental results is gratefully acknowledged

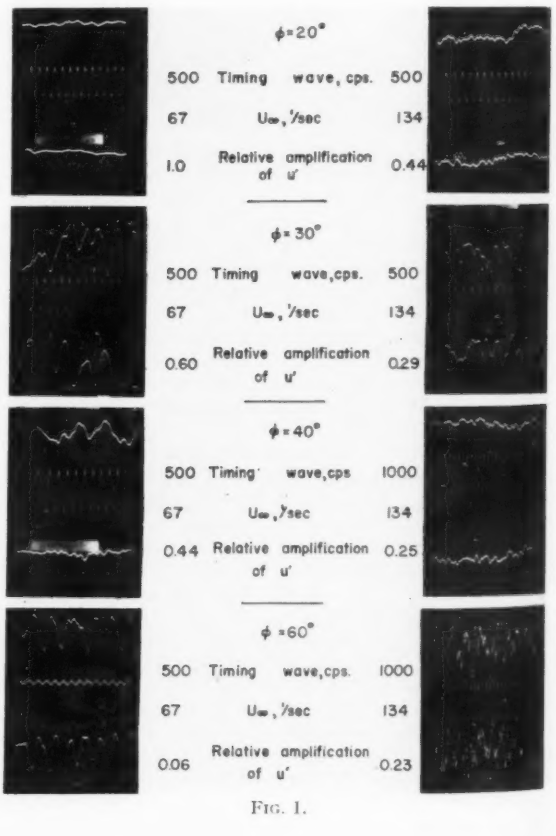
ϕ=20°
500 Timing wave, cps. 500
67 U∞, '/sec 134
1.0 Relative amplification of u' 0.44
ϕ=30°
500 Timing wave, cps. 500
67 U∞, '/sec 134
0.60 Relative amplification of u' 0.29
ϕ=40°
500 Timing wave, cps 1000
67 U∞, '/sec 134
0.44 Relative amplification of u' 0.25
ϕ=60°
500 Timing wave, cps. 1000
67 U∞, '/sec 134
0.06 Relative amplification of u' 0.23

FIG. 1.

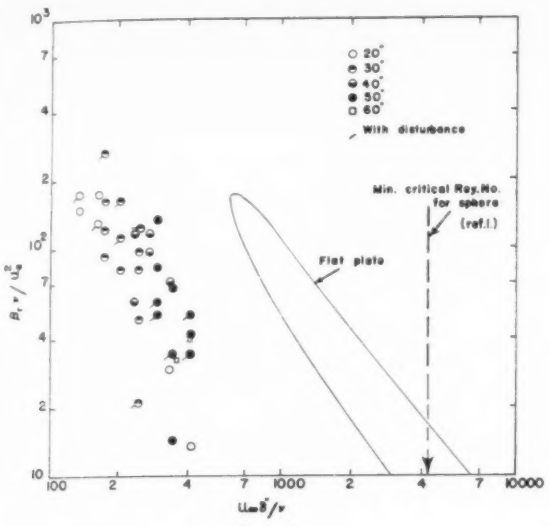

FIG. 2.

with a hemispherical nose 11.5 in. in diameter, at wind speeds up to 134 ft./sec. in the University of Michigan 5 × 7 ft. low-turbulence tunnel. Sample records at various angles from the nose along the same meridian plane are shown in Fig. 1. Two sweeps are shown for each condition. Approximate relative amplification factors for u' are indicated. The disturbances shown were probably produced by surface roughness since they did not appear at all meridian planes. The bursts of approximately sinusoidal fluctuations indicate that the instability is probably of the Tollmien-Schlichting type.

Comparison of the reduced frequency $\beta_r \nu / u_e^2$ where $\beta_r = 2\pi$ (frequency of the disturbances) and u_e is the velocity at the edge of the boundary layer versus $u_e \delta / \nu$ with the flat-plate (Schlichting) and with sphere stability theory[1] is shown in Fig. 2. Some of the points refer to records made with a rough "button" at the nose.

The fact that the disturbances appear and grow at Reynolds Numbers far below the critical value given by theory indicates the existence of a source of instability that is neglected in the theory. I suggest that this hitherto unrecognized source is the stretching of the vortex filaments in the region of diverging flow near the stagnation point.

Approximate analysis[2] of the destabilizing influences of stretching and surface cooling compared with the stabilizing influence of curvature indicates that near the nose the net effect is destabilizing. The analysis uses the Taylor-Görtler vortices (which stretch in the favorable pressure gradient) as a model, but it is pointed out[2] that analogous effects exist for those of the Tollmien-Schlichting type. Qualitative agreement between theory and the present experiment is obtained for the condition of no heat transfer to the body.

It is pointed out further[2] that, while the effect of cooling a flat plate is known to be stabilizing to Tollmien-Schlichting disturbances, when convex curvature is introduced the centrifugal force acting on a displaced particle causes a destabilizing influence as well. It seems reasonable, therefore, that if the curvature is large enough the effect of cooling a surface may be destabilizing to Tollmien-Schlichting disturbances.

A theoretical and experimental program is under way

REFERENCES

[1] Pretsch, J., *The Stability of Laminar Flow Past a Sphere*, NACA TM 1017, 1942.

[2] Kuethe, A. M., *On the Stability of Flow in the Boundary Layer Near the Nose of a Blunt Body*, Rand RM-1972, 1958.

Relative Importance of Free-Stream Vorticity and Self-Induced Pressure Gradient on a Flat-Plate Boundary Layer

Harold Mirels
Lewis Flight Propulsion Laboratory, NACA, Cleveland, Ohio
February 3, 1958

THE PROBLEM of the incompressible laminar boundary layer on a flat plate in a free stream containing a relatively small amount of vorticity, ω_0, has recently been discussed by Glauert[1] and Li.[2] In reference 1, Glauert refutes an earlier claim by Li[3] that the free-stream vorticity introduces a pressure gradient which should be considered in the solution for the effect of free-stream vorticity on the boundary-layer development. However, Glauert did not make an order-of-magnitude estimate of the self-induced pressure gradient and, consequently, Li remained unconvinced.[2] The purpose of this note, in support of Glauert, is to point out that if a self-induced pressure gradient must be considered, it is the pressure gradient associated with the displacement thickness of the zero-order ($\omega_0 = 0$) solution. (The effect of the free-stream vorticity on the self-induced pressure gradient is of higher order and is negligible.) Criteria for evaluating the relative importance of free-stream vorticity as compared with the self-induced pressure-gradient effect are also developed herein for both incompressible and supersonic flows. Unless otherwise specified, the notation of references 1 and 2 is followed.

Consider first the laminar boundary layer on a flat plate in an incompressible uniform stream. Various attempts have been made to improve the zero-order (Blasius) solution by expanding in inverse powers of the local Reynolds Numbers. Kuo[4] has shown that a first-order correction may be obtained by including, in the usual boundary-layer equation, the pressure gradient induced by the displacement thickness of the zero-order solution. The form of the stream function is then

$$\psi = \sqrt{u_0 \nu x}\,[f_0(\eta) + (1/\sqrt{Re_L})\sqrt{L/x}\,F_1(x, \eta) + \ldots] \quad (1)$$

where $Re_L = u_0 L/\nu$, L = plate length, and $F_1(x, \eta)$ is of order 1. The form of $F_1(x, \eta)$ is obtained by computing the pressure distribution due to the zero-order displacement thickness at the plate and in the wake. If a small amount of vorticity is in the free stream it will have a higher-order effect on the self-induced pressure distribution and therefore does not influence $F_1(x, \eta)$.

Now, consider the incompressible free stream to have a small amount of vorticity. The stream function can be expressed as[1]

$$\psi = \sqrt{u_0 \nu x}\,[f_0(\eta) + (\omega_0 L/u_0\sqrt{Re_L})\sqrt{x/L}\,f_1(\eta) + \ldots] \quad (2)$$

In order for this perturbation scheme to be valid it is necessary that

$$\omega_0 L/u_0\sqrt{Re_L} \approx \text{vorticity in free stream/vorticity in boundary layer} \ll 1 \quad (3)$$

The relative importance of the self-induced pressure gradient and small free-stream vorticity can now be evaluated. Considering x/L, $f_1(\eta)$, and $F_1(x, \eta)$ to be of order 1, the ratio of the free-stream vorticity effect to the self-induced pressure effect is

$$R \equiv \frac{\omega_0 L/u_0\sqrt{Re_L}}{1/\sqrt{Re_L}} = \frac{\omega_0 L}{u_0} \quad (4)$$

If R is large, only the free-stream vorticity effect need be considered. If R is small, only the self-induced pressure gradient effect need be considered. If R is of the order 1, both effects are equally important. However, in this case the resulting solution is simply the linear superposition of the pressure-gradient effect (as computed by Kuo) and the free-stream vorticity effect (as computed by Glauert or Li for the case of zero induced pressure).

A similar discussion can be made for the case of supersonic flow. Assuming a linear viscosity-temperature law, $\mu/\mu_0 = C(T/T_0)$, the zero-order displacement thickness can be expressed as

$$\delta_0^* = A\sqrt{\nu_0 x C/u_0}$$

where A is a constant. For Prandtl Number 1, and uniform wall temperature T_w, an approximate expression for A is[5]

$$A = 1.73(T_w/T_0) + 0.332(\gamma - 1)M_0^2$$

Using linearized supersonic theory, the pressure distribution induced by the zero-order displacement thickness is

$$(p - p_0)/p_0 = (\gamma M_0^2/\sqrt{M_0^2 - 1})\,(d\delta_0^*/dx) = [(\gamma M_0^2/2\sqrt{M_0^2 - 1})\,(A\sqrt{C}/\sqrt{Re_L})]\,\sqrt{L/x} \quad (5)$$

The boundary-layer perturbation, due to the self-induced pressure gradient, is of the order of the coefficient of $\sqrt{L/x}$ in Eq. (5). The effect of free-stream vorticity on compressible laminar boundary-layer development can be found by using a Howarth transformation. The perturbation parameter can be expressed as $\omega_0 L\sqrt{C}/(u_0\sqrt{Re_L})$ (see reference 6). The ratio of the free-stream vorticity effect to the self-induced pressure gradient effect is, roughly,

$$R = (2\sqrt{M_0^2 - 1}/\gamma A M_0^2)\,(\omega_0 L/u_0) \quad (6)$$

For hypersonic Mach Numbers, $A \approx M_0^2$ and

$$R \approx \omega_0 L/u_0 M_0^3 \quad (7)$$

Thus, at hypersonic speeds, the parameter $\omega_0 L/u_0$ must be extremely large in order for the free-stream vorticity effect to be comparable with the self-induced pressure effect.

References

[1] Glauert, M. B., *The Boundary Layer in Simple Shear Flow Past a Flat Plate*, Readers' Forum, Journal of the Aeronautical Sciences, Vol. 24, No. 11, pp. 848, 849, November, 1957.

[2] Li, Ting Yi, *Authors Reply* in reference 1.

[3] Li, Ting Yi, *Effect of Free-Stream Vorticity on the Behavior of a Viscous Boundary Layer*, Readers' Forum, Journal of the Aeronautical Sciences, Vol. 23, No. 12, pp. 1128, 1129, December, 1956.

[4] Kuo, Y. H., *On the Flow of an Incompressible Viscous Fluid Past a Flat Plate at Moderate Reynolds Numbers*, J. Math. and Phys. Vol. XXXII, No. 2–3, July–October, 1953.

[5] Lees, Lester, and Probstein, Ronald F., *Hypersonic Viscous Flow Over a Flat Plate*, Princeton University, Aeronautical Engineering Laboratory, Report No. 195, April, 1952.

[6] Li, T. Y., *Simple Shear Flow Past a Flat Plate in a Compressible Viscous Fluid*, Readers' Forum, Journal of the Aeronautical Sciences, Vol. 22, No. 10, pp. 724, 725, October, 1955.

One-Dimensional Transient Heat Flow in a Multilayer Slab

W. F. Campbell

Gas Dynamics Section, Division of Mechanical Engineering, National Research Council, Ottawa, Canada

January 17, 1958

Summary

In a recent contribution to the Readers' Forum[1] Wassermann gave analytic solutions for the temperature in a double layer slab, with a triangular heat rate input at one face, insulated at the other, and with no thermal resistance at the interface. His solutions were for the three particular cases:

$$k_1/\sqrt{a_1} \approx k_2/\sqrt{a_2}, \quad k_1/\sqrt{a_1} \ll k_2/\sqrt{a_2}, \quad k_1/\sqrt{a_1} \gg k_2/\sqrt{a_2}$$

I propose here to give the general solution to this problem, to indicate briefly how it is obtained using the method of reference 2, and to point out that the solutions given by Wassermann are incomplete for times longer than the duration of the heat input.

Symbols*

$R_{12} = (\mu_{12} - 1)/(\mu_{12} + 1) = -R_{21}$

$S_{12} = 2\mu_{12}/(\mu_{12} + 1) = \mu_{12}S_{21}$

$\mu_{12} = (k_1/k_2)\sqrt{a_2/a_1}$

$M(i, j, k)$ = the number of different and distinct paths from the plane of the heat source, $x = 0$, to the plane x, arriving at x in the direction of x *increasing*, which involve, in any possible order, i reflections back into layer No. 1 at the interface, $x = b$, j passages through the interface in the direction of x decreasing, and k reflections back into layer No. 2 at the interface. Thus, for example, $M_1(i, o, k) = 1$ if $k = 0$ and 0 if $k \neq 0$, $M_2(i, o, k) = 1$ for all k; $M_1(1, 1, 1) = 2$ $M_2(1, 1, 1) = 4$; and $M(3, 2, 0) = 10$, etc.

$N(i, j, k)$ = the number of different and distinct paths from the plane of the heat source, $x = 0$, to the plane x, arriving at x in the direction of x *decreasing*, which involve, in any possible order, i reflections back into layer No. 1 at the interface, $x = b$, j passages through the interface in the direction of x decreasing, and k reflections back into layer No. 2 at the interface. Thus, for example, $N_1(0, 0, 0) = 0$ and $N_2(0, 0, 0) = 1$

Discussion

THE GENERAL SOLUTION, assuming, of course, that the thermal properties are independent of temperature, is:

$$T_1' = \frac{8Q_{max}\sqrt{a_1}\,\theta^{3/2}}{\alpha\bar{\theta}k_1}\sum_{i=0}^{\infty}\sum_{j=0}^{\infty}\sum_{k=0}^{\infty}(R_{12})^i(S_{12}S_{21})^j(R_{21})^k\times\left\{M_1(i,j,k)i^3\text{erfc}\,\frac{[x + 2(i+j)b]\sqrt{a_2} + 2(j+k)(L-b)\sqrt{a_1}}{2\sqrt{a_1a_2\theta}} + N_1(i,j,k)i^3\text{erfc}\,\frac{[-x + 2(i+j)b]\sqrt{a_2} + 2(j+k)(L-b)\sqrt{a_1}}{2\sqrt{a_1a_2\theta}}\right\}$$

$$= F(\theta) \quad \text{for} \quad 0 \leq \theta \leq \alpha\bar{\theta}$$

$$T_1'' = F(\theta) - [1/(1-\alpha)]F(\theta - \alpha\bar{\theta}) \quad \text{for} \quad \alpha\bar{\theta} \leq \theta \leq \bar{\theta}$$

$$T_1''' = F(\theta) - [1/(1-\alpha)]F(\theta - \alpha\bar{\theta}) + [\alpha/(1-\alpha)]F(\theta - \bar{\theta}) \quad \text{for} \quad \theta > \bar{\theta}$$

$$T_2' = \frac{8Q_{max}\sqrt{a_1}\,\theta^{3/2}}{\alpha\bar{\theta}k_1}\sum_{i=0}^{\infty}\sum_{j=0}^{\infty}\sum_{k=0}^{\infty}(R_{12})^i(S_{12})^{i+1}(S_{21})^j(R_{21})^k\times\left\{M_2(i,j,k)i^3\text{erfc}\,\frac{[1 + 2(i+j)]b\sqrt{a_2} + [x - b + 2(j+k)(L-b)]\sqrt{a_1}}{2\sqrt{a_1a_2\theta}} + N_2(i,j,k)i^3\text{erfc}\,\frac{[1 + 2(i+j)]b\sqrt{a_2} + [b - x + 2(j+k+1)(L-b)]\sqrt{a_1}}{2\sqrt{a_1a_2\theta}}\right\}$$

$$= G(\theta) \quad \text{for} \quad 0 \leq \theta \leq \alpha\bar{\theta}$$

$$T_2'' = G(\theta) - [1/(1-\alpha)]G(\theta - \alpha\bar{\theta}) \quad \text{for} \quad \alpha\bar{\theta} \leq \theta \leq \bar{\theta}$$

$$T_2''' = G(\theta) - [1/(1-\alpha)]G(\theta - \alpha\bar{\theta}) + [\alpha/(1-\alpha)]G(\theta - \bar{\theta}) \quad \text{for} \quad \theta > \bar{\theta}$$

* These are in addition to those of reference 1.

The method used to write down the preceding solution is based on the well-known analogy of one-dimensional heat flow with the flow of an electric current in a simple transmission line having only series resistance and parallel capacitance. Thus when a "temperature wave," propagated from the heat source, arrives at a point where the thermal properties change abruptly, part of the wave is reflected at, and part passes through the discontinuity. The respective wave strengths are determined by easily calculated reflection and transmission coefficients. The temperature at a point is then made up of all the contributions from all the possible wave paths. Due to dissipation effects, in general, the longer the path length, the smaller the contribution. For the problems where this method is particularly useful, the transient temperature for "short" times only is required and all but a few terms are negligible. This method is fully described in reference 2 for many different types of heat source and for many different boundary conditions. A simpler description of the method is also given in reference 3 for a somewhat more restricted range of boundary conditions.

The solutions given by Wassermann in reference 1 lack terms of the form $F(\theta - \tilde{\theta})$ and are thus incomplete for $\theta > \tilde{\theta}$.

References

[1] Wassermann, B., *One-Dimensional Transient Heat Conduction into a Double-Layer Slab Subjected to a Linear Heat Input for a Small Time Interval*, Readers' Forum, Journal of the Aeronautical Sciences, Vol. 24, No. 12, p. 924, December, 1957.

[2] Campbell, W. F., *A Rapid Analytical Method for Calculating the Early Transient Temperature in a Composite Slab*, Report No. MT-32 of the Division of Mechanical Engineering, National Research Council, Ottawa, Canada, April, 1956.

[3] Campbell, W. F., *A Rapid Analytical Method for Calculating the Early Transient Temperature in a Composite Slab*, Transactions of the Engineering Institute of Canada, No. 1, p. 15, September, 1957.

Asymmetric Starting for Hypersonic Wind Tunnels

Robert H. Johnson
General Electric Research Laboratory, Schenectady, N.Y.

February 3, 1958

THE PROBLEM of flow initiation limits the maximum size of models one may study in supersonic wind tunnels. This is particularly true of hypersonic tunnels because the viscous effects retarding the flow establishment are exaggerated by the low density and large velocity gradients characteristic of such flows. A blunt, axially symmetric model further aggravates the starting problem. Here a strong detached bow shock wave interacts with the boundary layers and the resulting feedback may cause choking. Consequently, full tunnel flow may never become established.

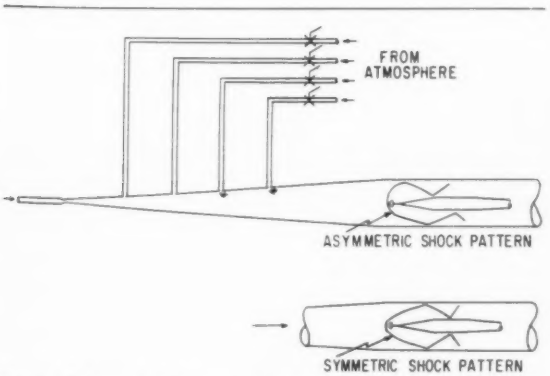

FIG. 1. Schematic diagram of helium-tunnel starting system.

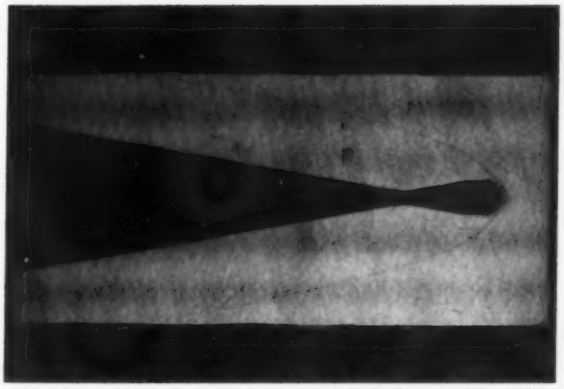

FIG. 2. 3/8-in. diameter cone-sphere in helium at $M = 22$.

The size and bluntness of a model is thus limited in a given tunnel. Since the shock wave from a blunt model in a hypersonic tunnel is the predominant part of the entire diffuser flow, it is possible to increase slightly the maximum possible size of the model by adapting the diffuser design to suit the shock-wave pattern. Thus, when the model shape or size is changed, it is frequently necessary to redesign the diffuser.

A new method for starting supersonic wind tunnels has been developed for use on the hypersonic helium tunnel at the General Electric Research Laboratory. This tunnel is currently operating in the Mach 21 to 28 range. The starting method employs a number of small air jets distributed along the length of the nozzle wall, as illustrated in Fig. 1. Individual quick-acting valves are provided for each air line so that air jets in any combination may be used. A maximum of five 0.010-in. diameter jet orifices have been used. The starting sequence proceeds in the following manner: (1) open air jet valves, (2) start tunnel flow, (3) close air jet valves. Once flow has been established by use of the air jets, it remains stable after closing the jet valves. The hysteresis is sufficient.

The asymmetric flow disturbance in the nozzle due to air jets changes the effective area ratio of the nozzle. This results in a lower Mach Number on one side of the test section. The shock wave, therefore, does not intersect the diffuser walls in a single transverse plane—i.e., the line of intersection between the shock and the boundaries form an irregular curve instead of a circle. This "spreading out" of the shock wave causes a weaker interaction with the boundary layer and reduces the tendency of the model shock wave to converge, and the shock-induced boundary-layer separation, with the resulting feedback, is retarded.

Similar improvement in the starting characteristics of the tunnel have been made by using a series of solid flow obstructions (short pieces of stiff wire) in place of the air jets. Other gases, such as helium, also have been used.

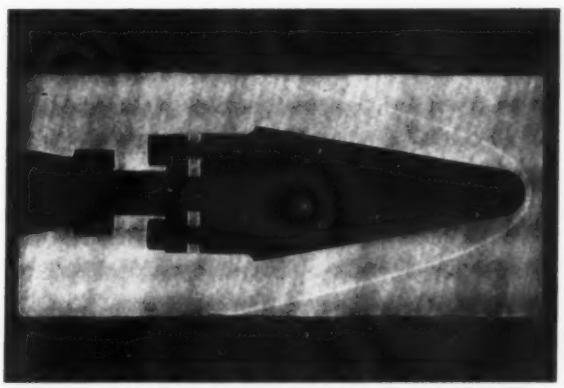

FIG. 3. 1-in. diameter cone-sphere in helium at $M = 22$.

The effectiveness of the asymmetric starting procedure is shown by the increase in the maximum model size which can now be used in our 3.6-in. diameter Mach Number 22 hypersonic helium tunnel. Without this new starting procedure, a 3/8-in. diameter model is the largest for which flow can be established. The new technique, however, permits establishing flow with models larger than 1 in. in diameter. (Mach Number 22 flow about a 3/8-in. and a 1-in. blunt model is shown in Figs. 2 and 3.)

Larger models, resulting in stronger shock waves, require greater asymmetry during the tunnel starting cycle. Thus, the optimum number and location of air jets must be determined for any given model configuration. It is conceivable that models even larger than 1-in. diameter may be used in the present equipment.

Note on "Stability Equations for Conical Shells"

Paul Seide
Guided Missile Research Division, The Ramo-Wooldridge Corporation, Los Angeles, Calif.
February 11, 1958

In a recent note,[1] Professor Kempner shows that the writer's equations for buckling of conical shells[2] are identical with those given by Vlasov[3] (although derived differently) and corrects an error in the writer's derivation of a single eight-order differential equation for the displacement normal to the cone surface, w. He then derives approximate uncoupled equations for the meridional and circumferential displacements, u and v, in terms of w.

The contributions by Professor Kempner concerning the prior derivation of the stability equations and the correction to the eighth-order equation were noted in the published version of the writer's paper[2] where it was also noted that a still earlier derivation of identical stability equations was apparently given by Mushtari.[4] Some further analysis reveals that it is unnecessary to make any approximations in deriving uncoupled equations for the displacements u and v in terms of the normal displacement w and that a further refinement in the eighth-order equation is possible.

It can be shown that the operator L_1 defined by the writer[2] (or H in Kempner's note) can be written as

$$(1/s^3)\nabla^4 s^2 \tag{1}$$

so that the final form of the eighth-order equation for w is

$$\frac{1}{s^3}\nabla^4 s^2\left[D\nabla^4 w - N_{S_0}\frac{\partial^2 w}{\partial s^2} - N_{\theta_0}\times\left(\frac{1}{s}\frac{\partial w}{\partial s}+\frac{1}{s^2}\frac{\partial^2 w}{\partial\bar{\theta}^2}\right) - 2N_{S\theta_0}\frac{\partial}{\partial s}\left(\frac{1}{s}\frac{\partial w}{\partial\bar{\theta}}\right)+S\frac{\partial w}{\partial s}+\Theta\frac{1}{s}\frac{\partial w}{\partial\bar{\theta}}\right]+\frac{Et\cot^2\alpha}{s^5}\frac{\partial^2}{\partial s^2}\left(s^3\frac{\partial^2 w}{\partial s^2}\right)=0 \tag{2}$$

with

$\nabla^2 = (\partial^2/\partial s^2) + (1/s)(\partial/\partial s) + (1/s^2)(\partial^2/\partial\bar{\theta}^2)$
$\nabla^4 = \nabla^2\nabla^2$
s = the distance from the cone vertex
θ = the angular measurement around the circumference
α = the cone semivertex angle
$\bar{\theta} = \theta \sin\alpha$
$N_{S_0}, N_{\theta_0}, N_{S\theta_0}, S, \Theta$ = middle-surface force components and surface force components prior to buckling
E = Young's modulus of cone material
t = wall thickness
ν = Poisson's ratio
$D = Et^3/[12(1-\nu^2)]$

The uncoupled equations for u and v can be derived as follows: Two of the equations of equilibrium of an element of the cone are given in terms of displacements as

$$\{s^2\nabla^2 - 1 - [(1+\nu)/2](\partial^2/\partial\bar{\theta}^2)\}u + (\partial/\partial\bar{\theta})\{[(1+\nu)/2](\partial/\partial s)s - 2\}v = [\nu(\partial/\partial s)s - (1+\nu)]w\cot\alpha \tag{3a}$$

$$(\partial/\partial\bar{\theta})\{[(1+\nu)/2](\partial/\partial s)s + 1 - \nu\}u + \{[(1-\nu)/2](s^2\nabla^2 - 1) + [(1+\nu)/2](\partial^2/\partial\bar{\theta}^2)\}v = (\partial/\partial\bar{\theta})w\cot\alpha \tag{3b}$$

It can be shown that the operators $(s^2\nabla^2 - 1)$ and $(\partial/\partial s)s$ are commutative; that is

$$(s^2\nabla^2 - 1)(\partial/\partial s)s(\ ) = (\partial/\partial s)s(s^2\nabla^2 - 1)(\ ) \tag{4}$$

Then the uncoupled equations can be readily obtained as

$$[(s^2\nabla^2 - 1)^2 + 4(\partial^2/\partial\bar{\theta}^2)]u = s^3\nabla^4 su = \Big([\nu(\partial/\partial s)s - (1+\nu)](s^2\nabla^2 - 1) - \{[(1+\nu)/2](\partial/\partial s)s - (3+\nu)\}(\partial^2/\partial\bar{\theta}^2)\Big)w\cot\alpha \tag{5a}$$

$$[(s^2\nabla^2 - 1)^2 + 4(\partial^2/\partial\bar{\theta}^2)]v = s^3\nabla^4 sv = (\partial/\partial\bar{\theta})\times[(2+\nu)s^2(\partial^2/\partial s^2) + 3s(\partial/\partial s) + 1 + (\partial^2/\partial\bar{\theta}^2)]w\cot\alpha \tag{5b}$$

which replace Eqs. (11) and (12) of Kempner's paper. It is interesting to note that the substitution

$$s/s_0 = e^z \tag{6}$$

introduced by Mushtari and Sachenkov[5] transforms Eqs. (5a) and (5b) into differential equations with constant coefficients which may be of some aid in solving cone stability problems.

References

[1] Kempner, Joseph, *Stability Equations for Conical Shells*, Journal of the Aeronautical Sciences, Vol. 25, No. 2, pp. 137–138, February, 1958.

[2] Seide, Paul, *A Donnell-Type Theory for Asymmetrical Bending and Buckling of Thin Conical Shells*, Journal of Applied Mechanics, Vol. 24, No. 4, pp. 547–552, December, 1957.

[3] Vlasov, V. S., *Basic Differential Equations in General Theory of Elastic Shells*, NACA TM 1241, February, 1951 (Prik. Mat. Mek., Vol. 8, pp. 109–140, 1944).

[4] Mushtari, H. M., *Some Generalization of the Theory of Thin Shells with Application to the Problem of Stability of Elastic Equilibrium*, Izvestiya of the Physico-Mathematical Society and the Scientific Research Institute of Mathematics and Mechanics at the Kazan University, Vol. II, Sec. 3, pp. 71–150, 1938 (also Prikl. Mat. Mek., Vol. 2, pp. 439–456, 1939).

[5] Mushtari, H. M., and Sachenkov, A. V., *On Stability of Cylindrical and Conical Shells of Circular Section Under the Simultaneous Action of Axial Compression and External Normal Pressure*, Prikl. Mat. Mek., Vol. 18, No. 6, pp. 667–674, 1954.

Application of the Witte Rearranging Method to a Typical Structural Matrix

Bertram Klein
Head, Structure Theory and Methods Group, Convair Astronautics, General Dynamics Corporation, San Diego, Calif.
February 10, 1958

The author has shown[1–3] how the analysis of a complicated structure may be reduced to the solution of a large matric equation. The matrix in the equation is large because the author has sacrificed size at the expense of simplicity of setup. There has been doubt expressed as to the practicality of this approach because one has to invert a large, unsymmetric matrix. The purpose of the present note is to illustrate how this predicament may be overcome.

Recently, Bruno Witte has devised a certain scheme[4] particularly suited to the type of matrix obtained in the matric method of structural analysis advocated by the author—a matrix with a large number of zero elements and representing a structure with weak coupling. (Coupling may be described as the interdependence of forces and/or displacements.) The method consists

initially of a systematic rearrangement of the orginal matrix (including the right-hand-side column if desired) so as to approximate as closely as possible an optimized triangular matrix. The purpose of the present note is to illustrate the final form of rearrangement when the Witte method is applied to a typical matrix previously set up by the author.

The matrix shown in Fig. 1 is the one appearing at the bottom of p. 41 of reference 1. The right-hand-side column is included as the seventeenth column. The rearranged form is that shown in Fig. 2. The numbers to the left and above in Fig. 2 represent the actual locations of the rows and columns in the original matrix of Fig. 1. Notice that the matrix is now triangularized except for the last two rows. Therefore the new form is close to a complete triangularization. Also notice the large number of zero elements still appearing above the main diagonal in Fig. 2.

Remember that the Witte rearranging method does not require any arithmetic operations such as connected with elimination. The method can be programed to be carried out completely automatically by a high-speed digital calculating machine. The time necessary to perform the rearrangement is small compared to the additional time necessary to complete the triangularization and, hence, to solve the matric equation. It appears that matric equations encountered in actual structural problems in which the method of references 1–3 are used can be rearranged by the Witte method in forms containing a large percentage of triangularized rows and a large percentage of zero elemeats above the main diagonal. Consequently, the time required to solve such matric equations and the storage necessary for the solution should be considerably less than the corresponding quantities for solid matrices of the same sizes. Therefore, one may conclude that the objection raised against the method of references 1–3 is not justified in light of the fact that the size of a matrix of the type encountered in itself is not a criterion of the time and storage required to solve the problem.

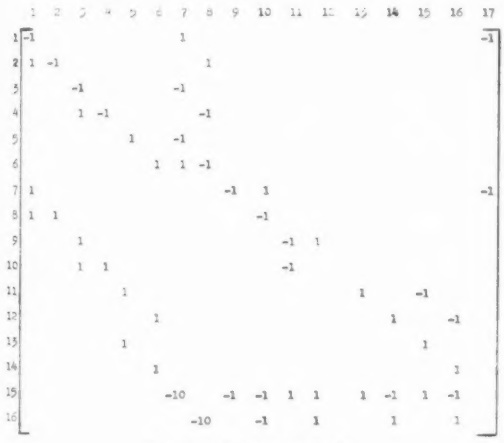

FIG. 1. Original matrix.

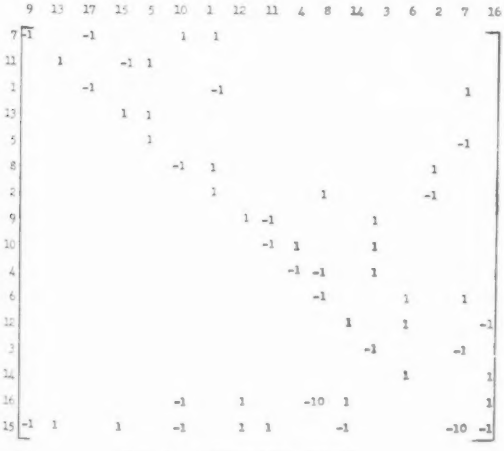

FIG. 2. Rearranged matrix.

REFERENCES

[1] Klein, B., *A Simple Method of Matric Structural Analysis*, Journal of the Aeronautical Sciences, Vol. 24, No. 1, pp. 39–46, January, 1957.

[2] Klein, B., *A Simple Method of Matric Structural Analysis, Part II—Effects of Taper and a Consideration of Curvature*, Journal of the Aeronautical Sciences, Vol. 24, No. 10, pp. 813–820, November, 1957.

[3] Klein, B., *A Simple Method of Matric Structural Analysis, Part III—Flexible Frame and Stiffened Cylindrical Shell Analysis*, Presented at the Missile Structures Session, Twenty-Sixth Annual Meeting, IAS, New York, January 27–30, 1958.

[4] Witte, B. W. F., *An Inside Out Procedure for Solving Linear Systems of Equations With Many Zero Coefficients*, to be published in the Journal of the Association for Computing Machinery.

The Conservation Equations for Multicomponent Gas Mixtures in Arbitrary Coordinate Systems

F. A. Williams*

Daniel and Florence Guggenheim Jet Propulsion Center, California Institute of Technology, Pasadena, Calif.

February 14, 1958

THE CONSERVATION equations for multicomponent reacting gas mixtures are generally given only in Cartesian or orthogonal curvilinear coordinate systems. Actually, the conservation equations are easily expressed in an arbitrary coordinate system. We present the general equations in tensor notation and then indicate the simplifications which arise for orthogonal curvilinear coordinates.

Let us consider a multicomponent gas mixture consisting of s different species which we identify by Greek subscripts. If Y_α is the mass fraction of species α, ρ is the density, v_i is the mass average velocity of the mixture, and $V_{\alpha i}$ is the diffusion velocity of species α, then the general equations for conservation of mass of component α, total mass, momentum, and energy may be written, respectively, as†

$$(\partial/\partial t)(\rho Y_\alpha) + (\rho Y_\alpha v^i)_{;i} + (\rho Y_\alpha V_\alpha{}^i)_{;i} = \omega_\alpha \tag{1}$$

$$(\partial\rho/\partial t) + (\rho v^i)_{;i} = 0 \tag{2}$$

$$\rho(\partial v_i/\partial t) + \rho v^j v_{i;j} = -P_i{}^j{}_{;j} + \rho \sum_{\alpha=1}^{s} Y_\alpha F_{\alpha i} \tag{3}$$

$$(\partial/\partial t)(\rho e) + (\rho e v^i)_{;i} = -Q^i{}_{;i} - P^{ij} v_{i;j} + \rho \sum_{\alpha=1}^{s} Y_\alpha V_\alpha{}^i F_{\alpha i} \tag{4}$$

Here ω_α is the mass rate of production of species α per unit volume by chemical reactions, P_{ij} represents the total stress tensor, and $F_{\alpha i}$ is the body force per unit mass acting on the component α. In Eq. (4) the quantity e represents the total internal energy of the mixture per unit mass, and Q_i denotes the total energy flux vector. English subscripts refer to covariant components, and superscripts identify contravariant components of the tensors.

In Eqs. (1) through (4) use is made of the summation convention for repeated English indices. The semicolon represents covariant differentiation with respect to the coordinates whose indices follow it. The covariant derivative of a tensor $A_{ij}{}^k$, for

* National Science Foundation Predoctoral Fellow.

† For a discussion of the reasoning by which Eqs. (1) through (4) can be derived, see, for example, P. G. Bergmann, *Introduction to the Theory of Relativity*, Prentice-Hall, New York, 1942.

example, is given by

$$A_{ij}{}^{k}{}_{;l} = (\partial A_{ij}{}^{k}/\partial x^{l}) - A_{rj}{}^{k}\left\{{r \atop i\ l}\right\} - A_{ir}{}^{k}\left\{{r \atop j\ l}\right\} + A_{ij}{}^{r}\left\{{k \atop r\ l}\right\} \quad (5)$$

where the Christoffel symbol of the second kind is defined by the relation

$$\left\{{k \atop i\ j}\right\} = (1/2)g^{kl}\left[(\partial g_{jl}/\partial x^{i}) + (\partial g_{il}/\partial x^{j}) - (\partial g_{ij}/\partial x^{l})\right] \quad (6)$$

In Eq. (6) the quantity g_{ij} is the metric tensor which defines the coordinate system by means of the expression for the invariant infinitesimal distance,

$$ds^2 = g_{ij}dx^{i}dx^{j} \quad (7)$$

In an orthogonal curvilinear coordinate system the metric tensor is diagonal and we can define the quantities $h_i = \partial s/\partial x^{i}$ by the equation

$$g_{ij} = \begin{bmatrix} (h_1)^2 & 0 & 0 \\ 0 & (h_2)^2 & 0 \\ 0 & 0 & (h_3)^2 \end{bmatrix} \quad (8)$$

It then becomes convenient to redefine a tensor in such a way that all of its components are of the same physical dimensions. This can be accomplished by dividing each covariant component i of the tensor by h_i and multiplying each contravariant component i by h_i. The new velocities u_i and $U_{\alpha i}$, body forces $f_{\alpha i}$, energy flux vector q_i, and stress tensor p_{ij} are therefore defined by the equations

$$\left.\begin{aligned} v_i &= h_i u_i \qquad [v^{i} = (1/h_i)\,u_i] \\ V_{\alpha i} &= h_i U_{\alpha i} \\ F_{\alpha i} &= h_i f_{\alpha i} \\ Q_i &= h_i q_i \\ P_{ij} &= h_i h_j p_{ij} \end{aligned}\right\} \quad (9)$$

The summation convention does not apply here nor in the following discussion because of the change in notation. The distinction between covariance and contravariance disappears in this formulation and we shall use subscripts for all indices.

By substituting Eq. (8) into Eq. (6) we find that, in orthogonal curvilinear coordinates, the relation

$$\left\{{k \atop i\ j}\right\} = (\delta_{ik}/h_k)(\partial h_k/\partial x_j) + (\delta_{jk}/h_k)(\partial h_k/\partial x_i) - (h_i\delta_{ij}/h_k^2)(\partial h_i/\partial x_k) \quad (10)$$

is valid. Here δ_{ij} denotes the Kronecker delta. If Eqs. (9) and (10) are used in Eqs. (1) through (4), then the following simplified forms for the conservation equations are obtained:

$$(\partial/\partial t)(\rho Y_\alpha) + \sum_i \left\{(1/h_i)(\partial/\partial x_i)\left[\rho Y_\alpha (u_i + U_{\alpha i})\right] + \left[\rho Y_\alpha (u_i + U_{\alpha i})\right] \sum_{j\neq i} (1/h_j h_i)(\partial h_j/\partial x_i)\right\} = \omega_\alpha \quad (11)$$

$$(\partial\rho/\partial t) + \sum_i \left[(1/h_i)(\partial/\partial x_i)(\rho u_i) + \rho u_i \sum_{j\neq i} (1/h_j h_i)(\partial h_j/\partial x_i)\right] = 0 \quad (12)$$

$$\rho(\partial u_i/\partial t) + \sum_j \rho u_j\left\{(1/h_j)(\partial u_i/\partial x_j) + (1/h_i h_j)\left[u_i(\partial h_i/\partial x_j) - u_j(\partial h_j/\partial x_i)\right]\right\} = - \sum_j \left\{(1/h_j)(\partial p_{ij}/\partial x_j) + p_{ij}(1/h_i h_j)\left[(\partial h_i/\partial x_j) - (h_i/h_j)(\partial h_j/\partial x_j) + \sum_k (h_i/h_k)(\partial h_k/\partial x_j)\right] - p_{jj}(1/h_i h_j)(\partial h_j/\partial x_i)\right\} + \rho \sum_{\alpha=1}^{s} Y_\alpha f_{\alpha i} \quad (13)$$

$$(\partial/\partial t)(\rho e) + \sum_i \left[(1/h_i)(\partial/\partial x_i)(\rho e u_i + q_i) + (\rho e u_i + q_i) \sum_{j\neq i} (1/h_j h_i)(\partial h_j/\partial x_i)\right] = - \sum_{i,j} \left\{(p_{ij}/h_j)(\partial u_i/\partial x_j) + \left[(p_{ij}/h_j) - (p_{ij}/h_i)\right](u_i/h_j)(\partial h_i/\partial x_j)\right\} + \rho \sum_{\alpha=1}^{s} \left(Y_\alpha \sum_i U_{\alpha i} f_{\alpha i}\right) \quad (14)$$

In Eqs. (13) and (14), use has been made of the symmetry of the pressure tensor p_{ij}. The derivation of Eqs. (11) through (14) for orthogonal curvilinear coordinates illustrates the method of application of the general conservation equations given in Eqs. (1) through (4).

Third U.S. National Congress of Applied Mechanics

Brown University, June 11–14, 1958

The congress program, being distributed in May, will feature over 100 papers in Applied Mechanics, including mechanics of rigid bodies, mechanics of deformable solids, mechanics of fluids and gases, thermodynamics, and heat transfer. In addition, there will be four general lectures by leading authorities.

To reduce the cost of attending the symposium to the utmost, the following all-inclusive living arrangement is offered. This covers rooms in the new West Quadrangle of Brown University and all meals from Breakfast on Wednesday, June 11, through Luncheon on Saturday, June 14, but *not* the Banquet on Thursday night ($5.00). The rates will be $24.00 for each of two persons sharing a room, or $30.00 for a person occupying a single room. Rooms will be available without additional charge for Tuesday night and Saturday night.

Registration Fees: Advance Registration on or before June 7, $4.00. Registration on June 8 or later, $6.00. Please make checks payable to: *Applied Mechanics Congress*, not to any person.

Requests for copies of the program and letters concerning advance registration should be addressed to Miss E. M. Addison, Box F, Brown University, Providence 12, R.I. In registering, please indicate number of persons in party and family relationship, desire for single rooms or willingness to share rooms, estimated arrival and departure times, and need for parking space.

onent i of
component
$_{ai}$, energy
ed by the

(9)

he follow-
distinction
his formu-

rthogonal

Σx_k) (10)

s. (9) and
ng simpli-

(11)

(12)

$x f_{ai}$ (13)

f_{ai}) (14)

n (14) for
Eqs. (1)

ics
ad-

ed.
11,
ch
nal

ase

di-
ily
for